EFFECT OF BOUTIQUE PROCESSING ON GEOMETRIC ATTRIBUTES: A
PERMIAN BASIN CASE STUDY

———————————————

A Thesis

Presented to

The Faculty of the Department of Geosciences

University of Houston

———————————————

In Partial Fulfillment

Of the Requirements for the Degree

Master of Science in Geophysics

———————————————

By

Joel Anthony Tabuli Famini

December, 2005

EFFECT OF BOUTIQUE PROCESSING ON GEOMETRIC ATTRIBUTES: A PERMIAN BASIN CASE STUDY

_____

Joel Anthony T. Famini

APPROVED:

_____

Dr. Kurt J. Marfurt, Ph. D.
Committee Chairman

_____

Dr. Hua-wei Zhou, Ph. D.
Committee Member

_____

Dr. Robert W. Wiley, Ph. D.
Committee Member

_____

Dr. Dengliang Gao, Ph. D.
Committee Member

_____

Dr. John Bear, Ph. D
Dean, College of Natural Science
and Mathematics

ACKNOWLEDGMENTS

ABSTRACT

Vacuum Field in Lea County, New Mexico is a mature, multi-pay field set in a carbonate platform and provides an ideal study area for studying the effects of the seismic processing flow on the geologic interpretation of 3-D seismic data. The geology of the field contributes to low reflectivity and poor illumination of the subsurface structures. Recent advancements in algorithm development have allowed for the calculation of full 3D volumes of dip and azimuth without the input of picked stratigraphic horizons.

I evaluate the effect of careful seismic processing in improving the lateral resolution of subtle features. I focus my attention on ground-roll suppression, deconvolution, and velocity picking. Results show that removal of ground-roll provides an improved image compared to volumes with no ground-roll filtering. Leaks of the residual of the ground-roll into the migrated data and appear as steeply-dipping artifacts on the migrated images. Following migration of the data sets, I generate geometric attributes including principal component coherence, coherent energy gradients, and curvature volumes. I use these output volumes along with the seismic data to faults, fractures, channels and slumps in front of the carbonate platform.

TABLE OF CONTENTS

CHAPTER 1

INTRODUCTION

1.1   Motivation of the Study

The emergence of 3-D reflection seismology and seismic attributes in the past two decades has greatly enhanced our ability to image the subsurface.   These new technologies have helped interpreters better interpret structural and stratigraphic variation between wells.

A focal point in the research of the Allied Geophysical Laboratories at the University of Houston is the development and calibration of new as well as existing seismic and geometric attributes and the application to various data sets from various regions of the world. As these algorithms continue to improve, better calibration of these attributes to well data can lead to more objective quantification of features and better correlation of the seismic to geology.

The Vacuum Field/Maljamar data set from southeast New Mexico (Figure 1.1) provides an ideal scenario for such an integrated study.   The availability of three overlapping volumes (two differently processed, post-stack volumes, and one pre-stack volume) allows geophysicist to make careful and controlled comparisons about how data quality limits the imaging of small-scale and subtle lateral features. Well control allows for the calibration of these modern seismic attributes, including coherence and geometric curvature, thereby providing greater insight into the complex geologic history of the Permian Basin.
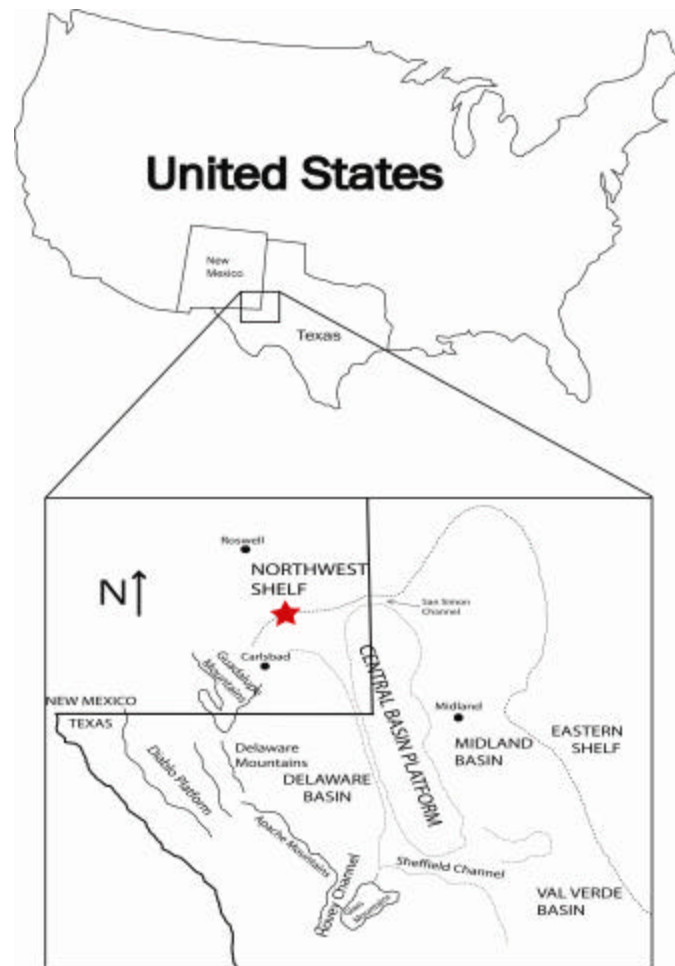
Figure 1.1 – Location of Vacuum Field, New Mexico. Figure is from Ward (1986).

1.2   Statement of the Problem

Data quality is the primary limitation of the Vacuum Field/Maljamar data set and severely hampers geophysical interp0072etation of the data. In addition, the geology of the Vacuum-Maljamar area affects the illumination of subsurface features that may not appear in the final section. Ground roll and acquisition footprint limit vertical and lateral resolution of subtle geologic features. Often, the typical solution to deal with these problems is to reprocess the whole data volume and compare the reprocessed volume with the original one. Unfortunately, most seismic processors are not familiar with the

appearance of subtle stratigraphic features (slumps, karsts, etc) as they appear on seismic vertical and time slices. Seismic attributes provide images that generally are easier to interpret than the conventional seismic data. In this "attribute-assisted" processing workflow, the processor is able to evaluate alternative processing parameters in terms of optimally imaging faults, channels, reefs, and other geologic features of interest.

1.3 Purpose of the Study

The Permian Basin has long been the object of interest for the oil and gas industry as well as academia due to its highly diverse geology and prolific hydrocarbon reservoirs. The primary purpose of this study is not to develop new geophysical techniques in seismic processing but rather to improve on existing workflows and on the geological interpretation of the Vacuum Field/Maljamar area, Lea County, New Mexico.

1.4 Overview of Thesis

Chapter 1 – This chapter contains a statement of the problem and motivation of the study regarding the Vacuum-Maljamar data set.

Chapter 2 – This chapter details the regional tectonics and lithostratigraphy found in the Vacuum-Maljamar area of the Permian Basin.

Chapter 3 – This chapter describes previous geophysical studies that are related to the processes and workflows used in this study.

Chapter 4 – This chapter details the seismic processing workflows utilized in processing the Vacuum-Maljamar data volume.

Chapter 5 – Comparison of the geometric attribute volumes generated from the different processing workflows. This chapter has side-by-side comparisons of the lateral resolution of subsurface features from the attribute volumes.

Chapter 6 – Interpretation and integration of analysis of the newly-processed Maljamar data set with the Vacuum Field Data volumes.

Chapter 7 – Conclusions and recommendations for future work and direction.

CHAPTER 2

GEOLOGY OF THE VACUUM-MALJAMAR AREA

2.1   Tectonic Setting

The Permian Basin of West Texas and Southeast New Mexico (Figure 2.1) is an area of great complexity, having undergone several tectonic events in its history (Figure 2.2).   The structural development and tectonic elements on its boundaries greatly influenced the depositional history during the Paleozoic and the subsequent maturation and occurrence of hydrocarbons in the basins (Hills, 1984).

Vacuum-Maljamar Field is located approximately 20 miles west of the town of Hobbs, Lea County, New Mexico (Figure 2.1).   It was discovered in 1929 with the drilling of the Socony Vacuum State 1 well in Section 13-T17S-R34E, and production in the area started in 1937.   It is situated on the Northwest Shelf of the Delaware Basin within the larger Permian Basin.   There are some 14 producing reservoirs in this field, with the Permian, Guadalupian, and Leonardian carbonates being the most prolific.   The Permian carbonates, which include the San Andres, Grayburg, Paddock, and Yeso formations, are considered the main producing zones in the area (Benson and Davis, 2000).
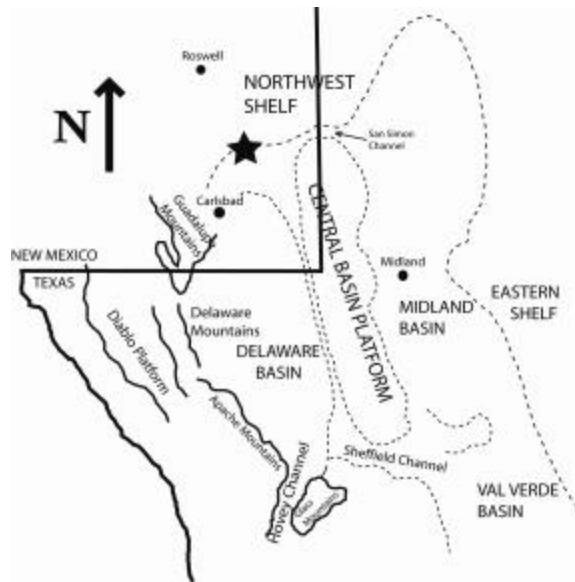
Figure 2.1 – Location map of Vacuum Field, located in the Northwest Shelf of the Delaware Basin of the New Mexico side of the Permian Basin. From Ward, et al. (1984).

The tectonic events in the Permian Basin are summarized in Figure 2.2. From Late Precambrian to Pennsylvanian (850-310 Ma), tectonic activity in the ancestral Permian Basin was in a passive margin phase, characterized by weak crustal extension and low-rate of subsidence (Horak, 1985).

A collisional phase characterized the late Paleozoic (Atokan) (310-265 Ma), with NE-SW trending suturing culminated in West Texas during the Early Permian (Horak, 1985). Continental collision compression transmitted 1000 km into the foreland. Permian age carbonate shelves dominate the North, East and West margins of the Permian Basin. Clastic sediments derived from orogenic activity dominate the basins.

High-mobility rates characterized the Permian Basin Phase (265-230 Ma). Elements of the basin subsided differentially but at decreasing rates. Rapid filling of the basins with fine-to-coarse grained clastics and extensive reef-fringed carbonate platforms and shelves proceeded until only the Delaware Basin remained as a small deepwater

6

depocenter (Horak, 1985). The rapid basin subsidence increased the relief on structures formed during the collision phase. The development of differing depositional environments, ranging from evaporitic shelves to deep-marine clastics formed the assemblage of rocks that include Lower Permian source rocks and Upper Permian reservoirs (Horak, 1985).
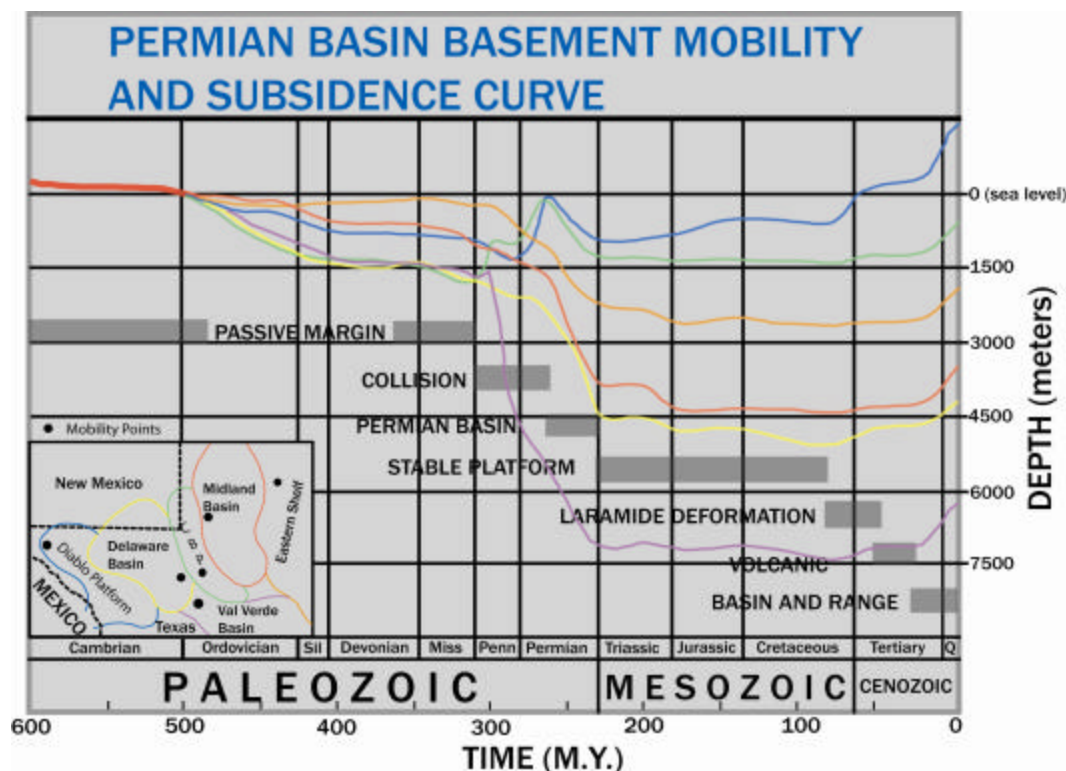
Figure 2.2 – A summary of the basement mobility and tectonic events of the Permian Basin. From Horak (1985).

Horak (1985) termed most of the Mesozoic Era (230-80 Ma) as the "stable platform phase." Mobility rates remained low and the region remained positive relative to the rifted Gulf of Mexico basin towards the south. Weak subsidence during the Early to Middle Cretaceous allowed the joining of the Cordilleran and Gulf of Mexico seaways.

7

Epeirogenic uplift and weak compressive overprinting from a western source occurred throughout the stable Permian Basin east of the Laramide front. The Permian Basin was permanently raised above sea level during this time (80-50 Ma).

Weak extension and crustal thinning followed the late Cretaceous-early Tertiary Laramide orogeny and preceded the Basin and Range event. Volcanism (40-30 Ma) from six centers in West Texas and Mexico (Horak, 1985) were characteristic of this time. This increased the regional heat flow in the SW Permian Basin.

Basin and Range tectonism (25-0 Ma) extends from the western Delaware Basin across the SW United States to California (Horak, 1985). This was characterized by distributive rifting, crustal extension and thinning, high heat flow, and low gravity values and compressional velocity.

The Delaware Basin is the most western division of the Permian Basin. It is an irregular, north-northwest trending, inverted pear-shaped depression about 250 km long by 180 km wide, covering an area of approximately 33, 500 km^2. It is one of the deepest intracratonic basins in North America, containing about 7135 m of Phanerozoic sediments (Hill, 1996).

The Delaware Basin lies between the structurally active Basin and Range Province and non-active Great Plains Province (Hill, 1996). Chapin and Cather (1994) consider the west side of the Delaware Basin to be part of the Rio Grande Rift, which they consider to form the western boundary of the North American Craton. The eastern limit of the Basin and Range normal faulting zone is in New Mexico and West Texas is along the western limit of the Delaware Basin. The Border Fault Zone, composed of the Guadalupe, Delaware, and Apache fault zones, is about 240 km and trends N20°W,

extending from the northern Davis Mountains in Texas to the head of the Lewis Canyon in New Mexico, where the Guadalupe Mountains merge with the Sacramento Mountains. The southern zone of faulting has a trend of N45°W and is considered to be an extension of the regional trend of the Sierra Madre Oriental of Mexico. This is parallel to the trend of both the Texas Lineament and the Chihuahua tectonic belt. Pre-Leonardian rocks in the Glass Mountains are related to the Marathon-Ouachita fold belt in the south (Hill, 1996).

Simple structures characterize the near surface of the Delaware Basin. Faulting is distinct only in the exposed western side of the Delaware Basin and only has gentle folding, except for anticlinal features in the bedded salt. The Guadalupe Mountains, from the Guadalupe Peak to Carlsbad, has a regional dip of about 1° northeastward. Pennsylvanian to Wolfcampian and older rocks exhibit more complex structure toward and east and south of the basin deeper in the subsurface.

The tectonic evolution of the Delaware Basin is closely related to the depositional sequence of packages of the area. The San Andres Formation is a marine carbonate platform that occupied the shelf and basement highs of the late Leonardian to mid-Guadalupian time of the Permian Basin (Kerans and Fitchen, 1995). The San Andres, along with its basinal equivalents the Brushy Canyon, Cherry Canyon, and Bone Spring Formations, present a complex record of equal sedimentation showing periods of basin starvation and carbonate platform aggradation and progradation followed by periods of exposure and sediment bypass. San Andres sedimentation occurred along the landward periphery of the basin and its basement highs.

2.2   Lithologic Description

The Capitan Reef Complex surrounds the perimeter of the Delaware Basin, encompassing the inner area of the basin at all sides. It extends as a narrow carbonate belt around the basin, extending approximately 600-700 km. It outcrops around the basin in the Guadalupe, apache, and Glass Mountains, but most of the Capitan Reef is in the subsurface. The whole Capitan Reef Complex includes also the backreef and basin strata. A comparative stratigraphic column of the Delaware Basin and nearby basin follows in figure 2.3.

The Paddock Formation is subdivided into an Upper and Lower Paddock, with the Upper Paddock subdivided into an Upper Paddock Limestone and Upper Paddock Dolomite. The Upper Paddock has thickness of about 150 ft and is the main producer. The Upper Paddock Dolomite acts as a barrier between the limestone and a highly fractured, producing Lower Paddock Dolomite (Acuna, 2000).

The late Leonardian Glorieta section overlying the Paddock consists of dolomitic sandstone. It is a low-stand deposit, restricted to a shallow shelf environment. The Glorieta Formation is composed of cyclically deposited siliciclastics, carbonate, and carbonate-evaporite deposits. It is from varying environment of deposition from supratidal to shallow sub-tidal to open marine environments. Siliciclastics are mainly eolian-derived sediments deposited onto the shelf.
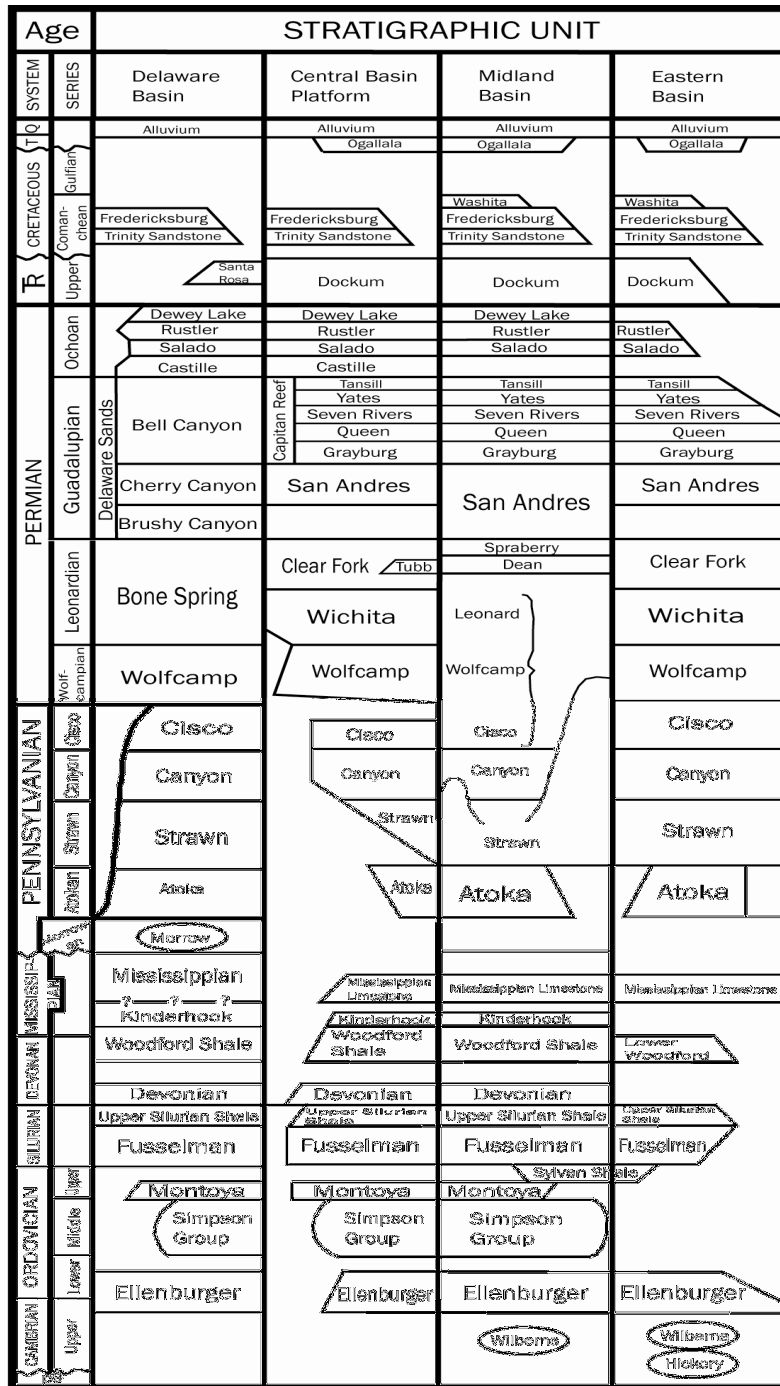
Age		STRATIGRAPHIC UNIT			
SYSTEM	SERIES	Delaware Basin	Central Basin Platform	Midland Basin	Eastern Basin
CRETACEOUS (TQ)	Gulfian	Alluvium	Alluvium / Ogallala	Alluvium / Ogallala	Alluvium / Ogallala
	Coman-chean	Fredericksburg / Trinity Sandstone	Fredericksburg / Trinity Sandstone	Washita / Fredericksburg / Trinity Sandstone	Washita / Fredericksburg / Trinity Sandstone
TR	Upper	Santa Rosa	Dockum	Dockum	Dockum
PERMIAN	Ochoan	Dewey Lake / Rustler / Salado / Castille	Dewey Lake / Rustler / Salado / Castille	Dewey Lake / Rustler / Salado	Rustler / Salado
	Guadalupian	Bell Canyon (Delaware Sands)	Tansill / Yates / Seven Rivers / Queen / Grayburg (Capitan Reef)	Tansill / Yates / Seven Rivers / Queen / Grayburg	Tansill / Yates / Seven Rivers / Queen / Grayburg
		Cherry Canyon	San Andres	San Andres	San Andres
		Brushy Canyon			
	Leonardian	Bone Spring	Clear Fork / Tubb	Spraberry / Dean	Clear Fork
			Wichita	Leonard	Wichita
	Wolf-campian	Wolfcamp	Wolfcamp	Wolfcamp	Wolfcamp
PENNSYLVANIAN	Cisco	Cisco	Cisco	Cisco	Cisco
	Canyon	Canyon	Canyon	Canyon	Canyon
	Strawn	Strawn	Strawn	Strawn	Strawn
	Atokan	Atoka	Atoka	Atoka	Atoka
	Morrow	Morrow			
MISSISS.		Mississippian / ?—?—? / Kinderhook	Mississippian Limestone / Kinderhook	Mississippian Limestone / Kinderhook	Mississippian Limestone
DEVON.		Woodford Shale	Woodford Shale	Woodford Shale	Lower Woodford
		Devonian	Devonian	Devonian	
SILURIAN		Upper Silurian Shale	Upper Silurian Shale	Upper Silurian Shale	Upper Silurian Shale
		Fusselman	Fusselman	Fusselman	Fusselman
ORDOVICIAN	Upper	Montoya	Montoya	Sylvan Shale / Montoya	
	Middle	Simpson Group	Simpson Group	Simpson Group	
	Lower	Ellenburger	Ellenburger	Ellenburger	Ellenburger
CAMBRIAN	Upper			Wilberns	Wilberns / Hickory

Figure 2.3 – Stratigraphic column of the Delaware Basin and surrounding basins. Modified from the United States Geological Service (USGS) website (2004), www.usgs.gov.

CHAPTER 3

Previous Studies

The original Vacuum-Maljamar survey was collected in the mid-1990s for a consortium of exploration and service companies. The Allied Geophysical Laboratories has two volumes of the Vacuum Field data produced from two differing processing workflows.

The first data set was obtained from Company A (hence called Volume A). Processing notes are not present and have been presumed lost to antiquity. What is known is the data has dip moveout applied and was migrated, followed by a FXY spatial prediction filtering. Figures 3.1 and 3.2 shows the quality of data of the two volumes of the Vacuum Field survey. Figure 3.1 is a time slice taken from a time of 1.5s and Figure 3.2 is cross-section A-A' running east west as marked on Figure 3.1.
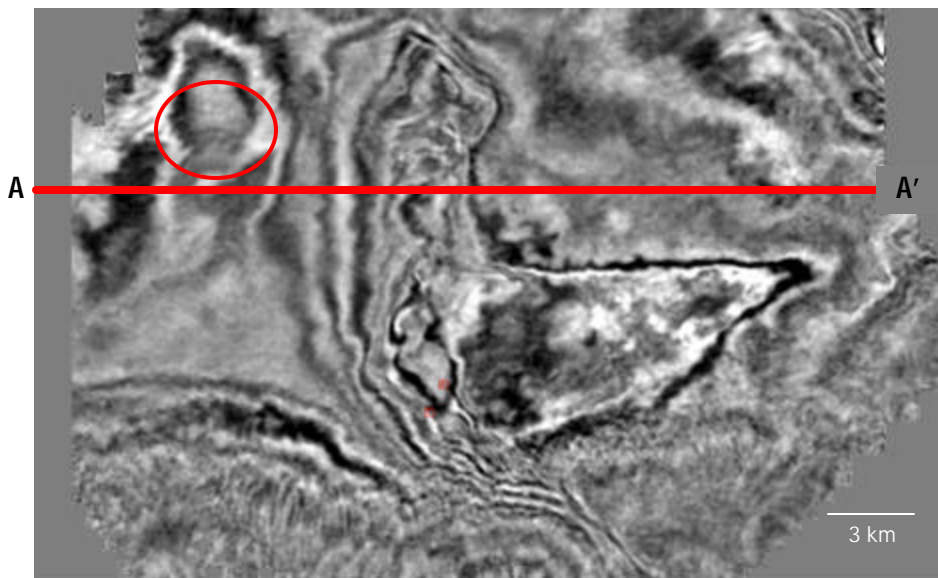

Figure 3.1 – Time slice of Vacuum Field taken from t=1.5s. Cross-section A-A' is displayed in Figure 3.2. The red circle is area where acquisition footprint can be seen.
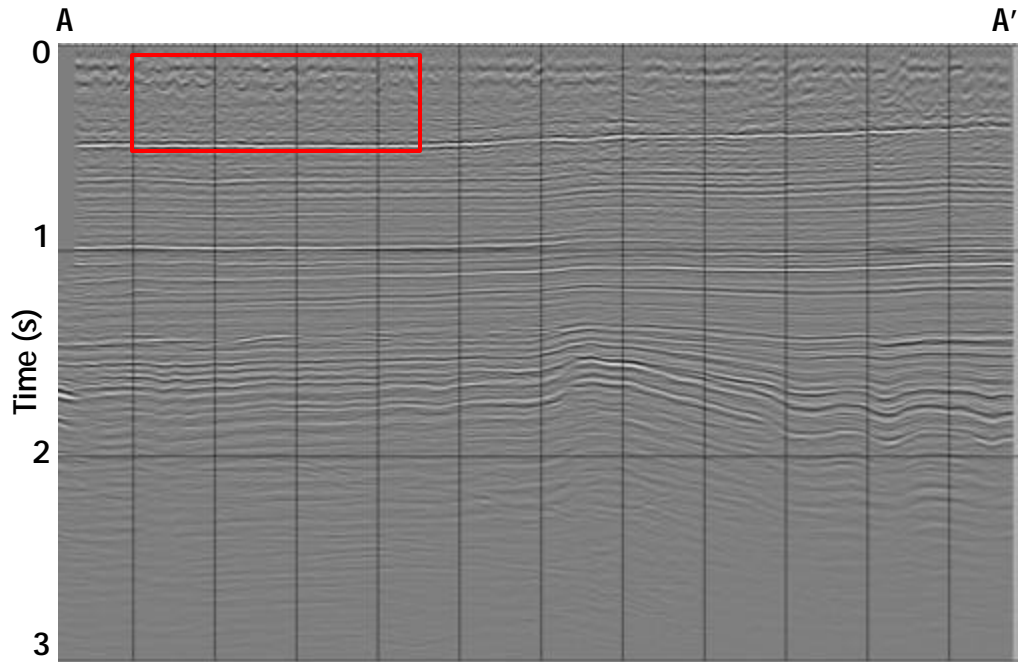
Figure 3.2 – East-west transect through the Vacuum Field survey from the Company A. The red box shows the extent of acquisition footprint on the data.

The second seismic volume was acquired from Company B (hence called Volume B. The data have been corrected to a datum of 4000 ft (1200 m) above sea level, with a datum velocity of 8000 ft/s (2400 m/s). Surface consistent spiking deconvolution as well as spectral balancing was applied before the first iteration of velocity on a 1-mile (1.6 km) grid. Surface-consistent residual statics followed another iteration of velocity analysis on a 0.5-mile (0.8 km) grid. After dip moveout, data were stacked and migrated with a wave-equation migration using 100% of the smoothed stacking velocities.

Despite the difference in processing flows, Volume A and Volume B exhibit similar problems. Acquisition footprint is very much visible in both data volumes. In Figures 3.1 and 3.4, I encircle areas where acquisition footprint can be seen in time slices, while Figures 3.2 and 3.3 shows acquisition footprint in the vertical section. Residual noise can be seen in the shallow sections of section A-A'. I identify these noise

trains in Figures 3.2 and 3.3 (red rectangles). These can be artifacts from ground roll and
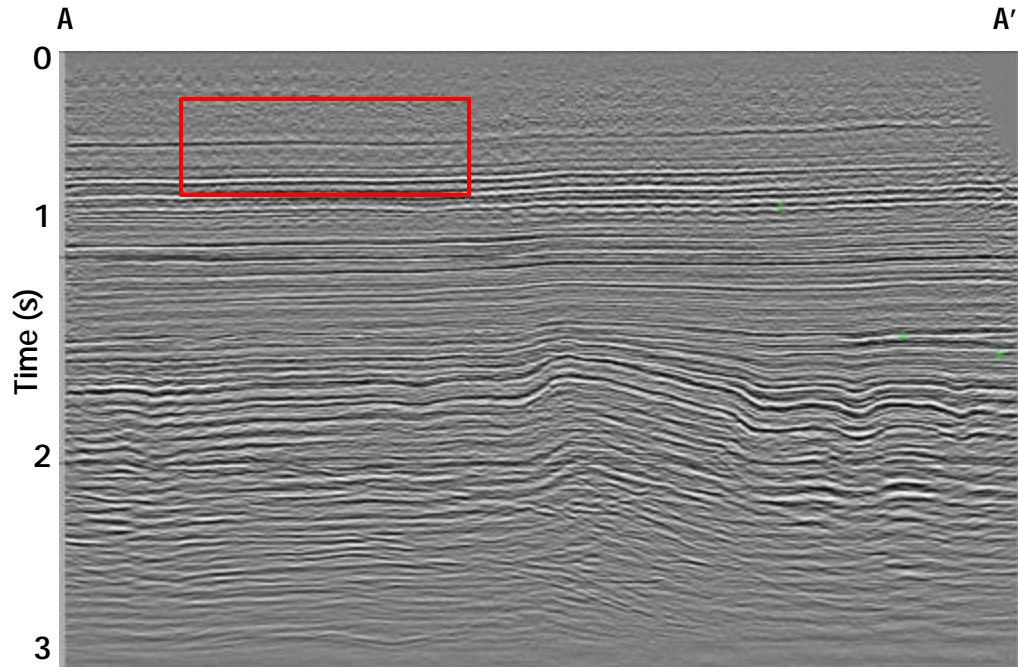
its back-scattered components.

Figure 3.3 – Cross-section A-A' (Figure 3.1) taken from the seismic volume of Company B. The red box shows the extent of acquisition footprint on the data.

Figure 3.4 – Time slice taken at t=1.5s from the Company B volume. The red circle is area where acquisition footprint can be seen.

3.1 Seismic Data Processing

3.1.1 Ground Roll Filtering

Ground roll is usually generated as 3D seismic data are being acquired in land surveys. Anstey's (1986) shows how the stack array can attenuate ground roll in 2D data. The stack array takes into consideration the geology of the area of interest and design an effective array length that is equal to the to the group interval to avoid spatial aliasing.

The effectiveness of the stack array is reduced in 3D seismic since the perpendicular arrangement of source and receiver pairs used in 3D land acquisition causes high apparent velocity of the ground that obscures the seismic signal (Smith and McKinley, 1996). For 3D data, migration does an efficient job in attenuating ground roll.

D'Agosto (2003) modeled and removed ground roll from the horizontal component of converted waves to enhance the imaging of carbonate reservoirs. Ground roll is flattened following a linear moveout to a velocity of a component of ground roll and is extracted using the coherence of the dominant dip direction and is summed with the original trace.

3.1.2 Acquisition Footprint

Acquisition footprint is defined as pattern in the seismic data caused by the surface acquisition geometry, or processing methodology, or irregularities as opposed to having geologic significance (Sheriff, 2002). Aliased steeply noise such as ground roll and multiples causes artifacts in the data (Gulanay, 1999). In 3D seismic surveys, economics often constrain the design of the stack arrays, allowing for the leakage of

aliased noise into the stacked volumes as periodic events. Figure 3.5 shows a shallow time slice taken from the Vacuum Field survey.
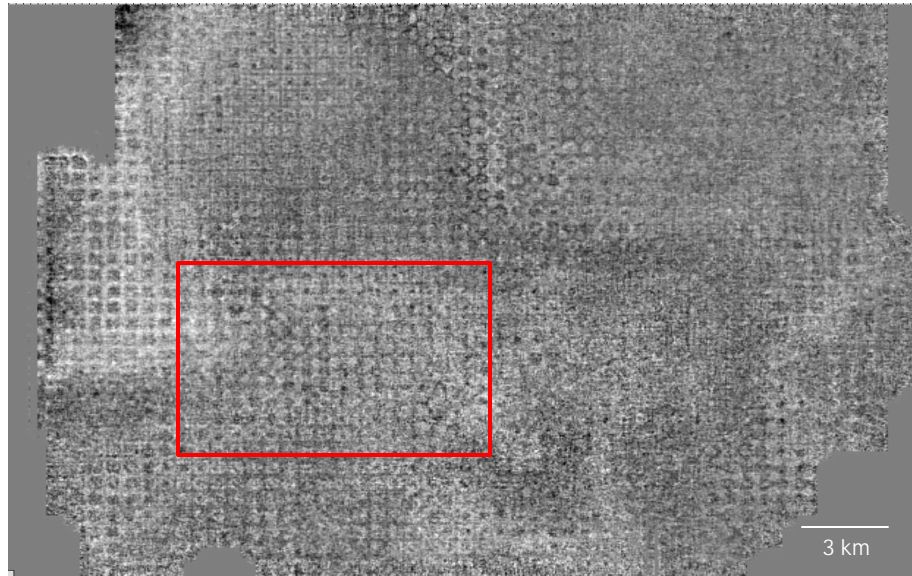

Figure 3.5 – Time slice taken at 0.4s from the Vacuum Field survey. Acquisition footprint (red square) manifests itself in a "checkerboard" pattern.

Several studies have been done in improving acquisition footprint in data. Marfurt et al (1998a) found that seismic coherence is very sensitive to coherent noise that passes through the survey acquisition. They also found that edge preservation methods further exacerbates these linear artifacts.

3.2   Seismic Attributes

A seismic attributes is defined as "a measurement derived from seismic data based on measurements of time, amplitude, frequency, and/or attenuation" (Sheriff, 2002). Figure 3.6 is a classification chart of all known currently known attribute classes. Since most seismic attributes have some sort of empirical relationship to stratigraphy and

reservoir properties, it is widely utilized by seismic interpreters to delineate geologic structure and rock properties of the subsurface.

The advent of 3-D seismic data brought forward more advancement in the field of attribute analysis. Three-dimensional data allowed the interpreter to view the data either in time slices or horizon slices, the former being a horizontal slice through the data without having to reference a pre-picked stratigraphic horizon (i.e. in time), while the latter is referenced to a picked horizon. This advancement brought forth a new generation of seismic attributes for use in interpreting the data. Geometric attributes such as coherence, amplitude gradients, and curvature provide interpreters another way of viewing the data.
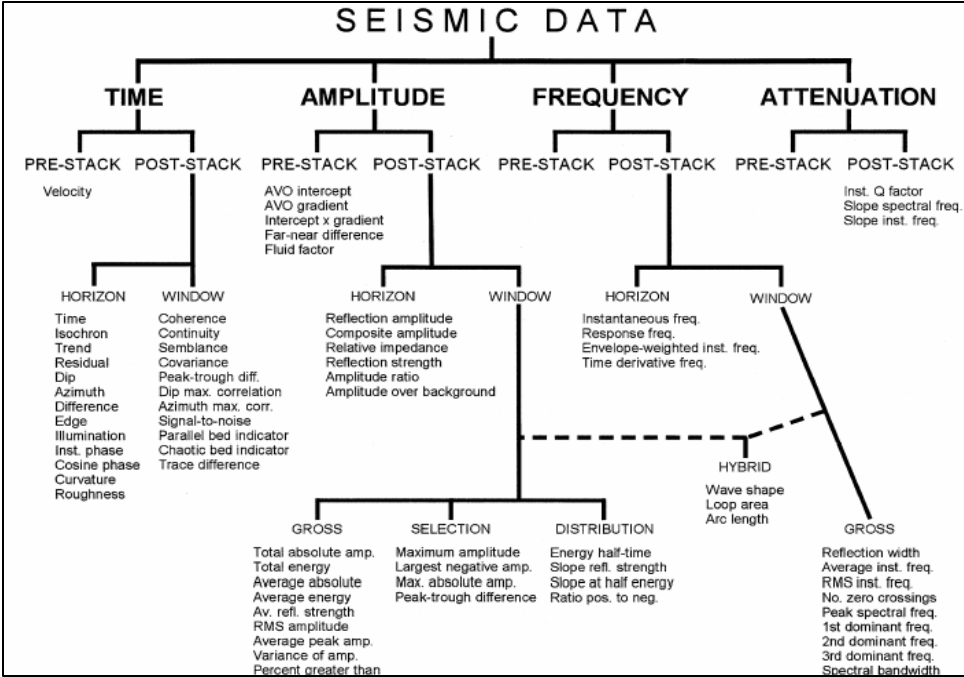

Figure 3.6 – Classification of seismic attributes. Seismic data is broken down to four fundamental components: time, amplitude, frequency, and attenuation (Brown, 2001).

17

3.2.1　Coherence

Seismic coherence is one of the more popular attributes in interpreting seismic data. The coherence cube of Bahorich and Farmer (1995) is effective in imaging seismic faults when there lateral differences in the acoustic impedance. The algorithm also allows for effective imaging subtle differences in stratigraphy, i.e. highlighting distributary channels, point bars, slump valleys, and drainage patterns. Advantages of applying seismic coherence to a cube of seismic data are outlined by Marfurt and others (1998):

1) Interpretation of data is accelerated as it eliminates the need for any preliminary detailed picking of stratigraphic horizons. Previous algorithms relied on the accuracy of pre-picked horizons.

2) Algorithm allows for generation of data across the whole volume, i.e. the area of interest, as well as zones adjacent to the area of interest.

3) Coherency allows for imaging of subtle and small scale features not imaged from picks of peaks, troughs, and zero-crossings.

4) Maps of channels and fans can be generated based on sequence boundary instead of reflector boundaries.

5) Features parallel to pickable formation tops and bottoms can be analyzed.

Three-dimensional seismic data is generally binned into a regular grid. Bahorich and Farmer's (1995) algorithm is based on normalized cross-correlation, calculating localized similarity of the waveform in both the inline and crossline directions. Figure 3.7 shows a simplistic representation of this process. A limitation of this method is that in data contaminated with coherent noise, the two-trace dip estimation can be noisy.
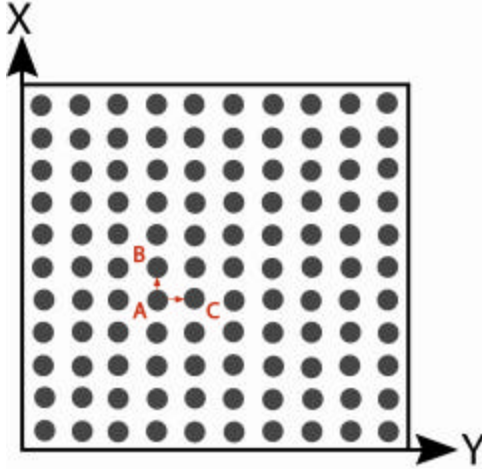
18

Figure 3.7 – A simple illustration of computation of coherence where a minimum three-trace operator is used. Similarity between points A and B and between points A and C is computed, and the combination of the two 2-D measurements is a measure of the 3-D coherence (Bahorich and Farmer, 1995).

Marfurt et al. (1998) improved upon Bahorich and Farmer's method by including more traces in a multi-trace semblance estimation. An elliptical or rectangular analysis window containing J number of traces is defined (Figure 3.8). If the axis (x, y) is centered at the analysis point, semblance can be calculated by:

$$s(t,p,q) = \frac{\left[\sum_{j=i}^{J} u(t - px_j - qy_j, x_j, y_j)\right]^2 + \left[\sum_{j=1}^{J} u^H(t - px_j - qy_j, x_j, y_j)\right]^2}{J \sum_{j=1}^{J} \{[u(t - px_j - qy_j, x_j, y_j)]^2 + [u^H(t - px_j - qy_j, x_j, y_j)]^2\}} \quad (3\text{-}1),$$

where (τ, p, q) are points defining a local planar event at time τ, and p and q are apparent dips in the x and y direction measured in milliseconds per meter (Figure 3.9), and H represents the Hilbert transform of the real seismic trace, u. Semblance allows for estimation of coherency even around the zero-crossing of reflection events.
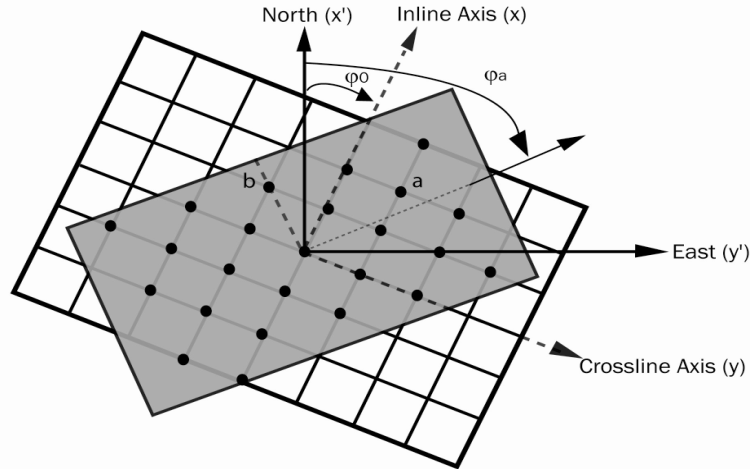
Figure 3.8 – Rectangular analysis windows centered about an analysis point defined by length of major axis *a*, length of minor axis *b*, and azimuth of major axis φ_a. From Marfurt (1998).
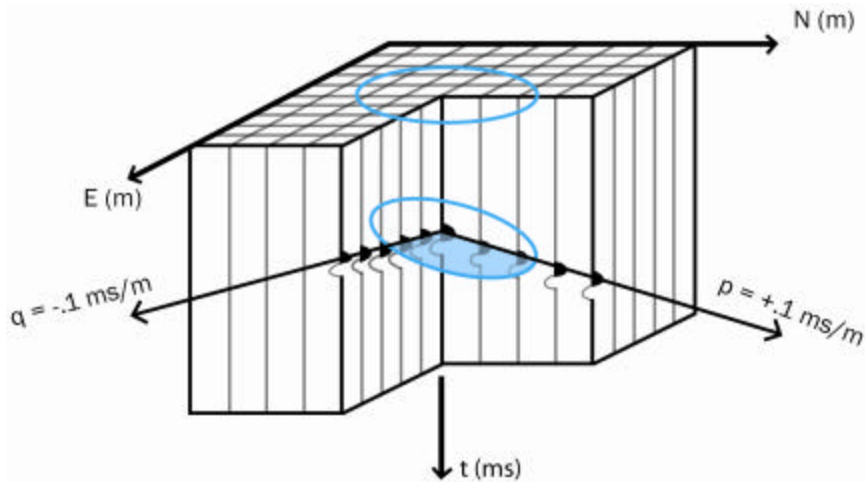
Figure 3.9 – Coherence calculation in 3-D. Coherence is computed over an elliptical window with apparent dips $(p, q) = (0.1$ ms/m, -0.1 ms/m). From Marfurt (1998).

3.2.2 Coherent Energy Gradient

Semblance and variance algorithms measure variations in amplitude over the whole seismic volume regardless of the waveform. Coherent energy gradients measure amplitude changes of only the coherent component of the seismic data. Figure 3.10

illustrates the calculation for the coherent energy gradient. The method of computation comes from the eigenstructure computation of coherence (Marfurt, 2006). The eigenstructure method uses a window of traces (Figure 3.10a) then finds the wavelet that best fits the change in waveform (Figure 3.10b). The wavelet is scaled to fit to each of the traces to find the coherent component of the seismic data inside the analysis window (Figure 3.10c). The eigenstructure coherence is taken from the ratio of the energy of the coherent component of the data (Figure 3.10c) and the energy of the original traces (Figure 3.10a) within the analysis window. In Figure 3.10d, the amplitude of the coherent wavelet that best fits the traces within the analysis window. The dotted line in Figure 3.10d represents the curve that best fits the lateral variation in the values of the seismic.

Marfurt (2005) notes two ways to calculate the coherent energy gradients. The first method takes the derivative of the principal components and found that the method is sensitive to the noise that leaks through the stacked section. The second method weights the derivatives using the energy of the coherent component of the data.
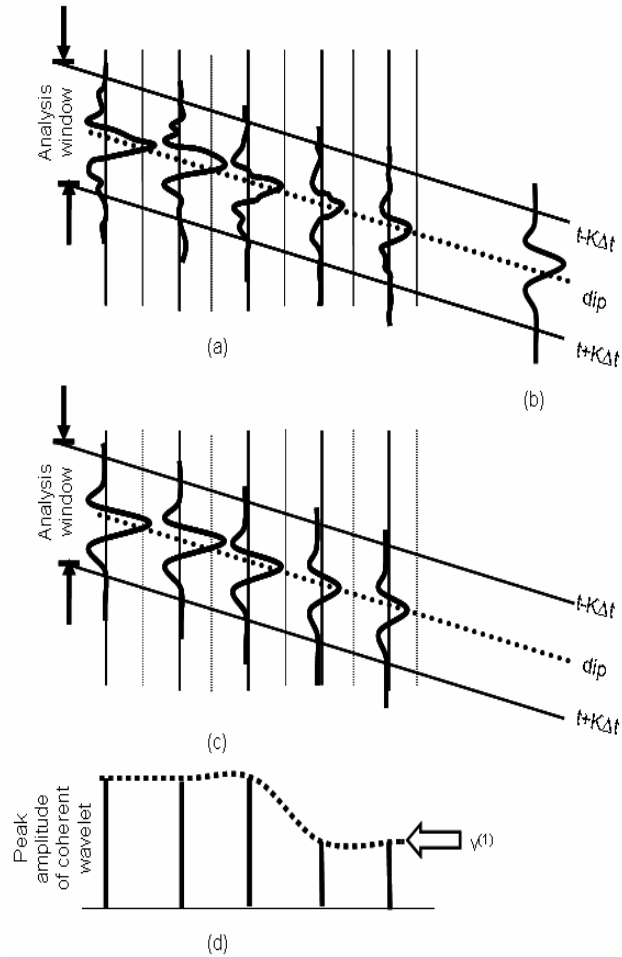
Figure 3.10 – Graphical explanation of computation for the eigenstructure. From Marfurt (2005). See text for discussion.

Application to 3-D data is to represent the amplitude of the coherent data into a discrete sampled map by a local $v(x, y)$. The values represent the lateral changes in coherent energy along the structural dip and azimuth of the reflector of interest (Figure 3.11).
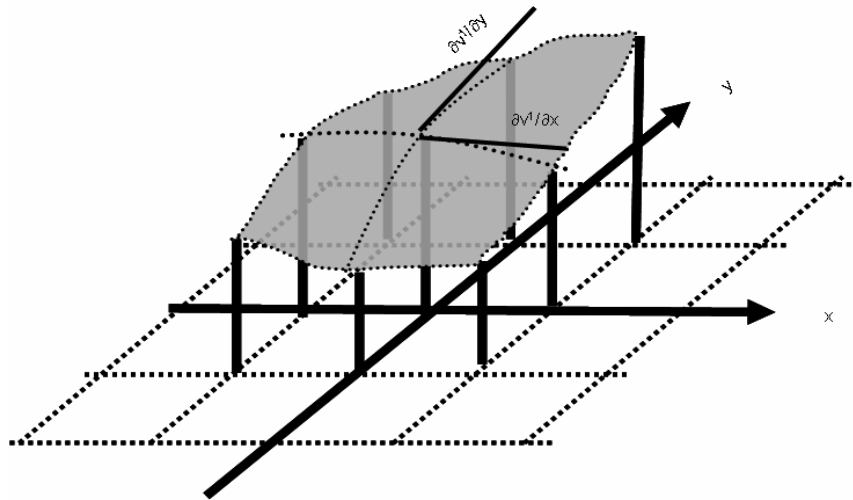
Figure 3.11 – Application to 3-D data of the coherent energy gradients. From Marfurt (2005).

3.2.3   Curvature

Curvature as an attribute has been in limited use in seismic interpretation. It is a surface-derived attribute (Roberts, 2001) where its purpose is to enhance a property of a surface which may not be easily defined. In this aspect, a surface can be a flat surface, an interpreted surface, or an arbitrary window from which an attribute can be extracted.

Curvature is defined by Roberts (2001) as "the two-dimensional property of a curve and describes how bent a curve is at a particular point on the curve, i.e. how much the curve deviates from a straight line at this point." Figure 3.12 shows an illustrated definition of curvature. In the figure, Roberts shows that curvature is simply the reciprocal of the radius of curvature, *R*, where the smaller the *R*, the larger the curvature, and vice-versa.
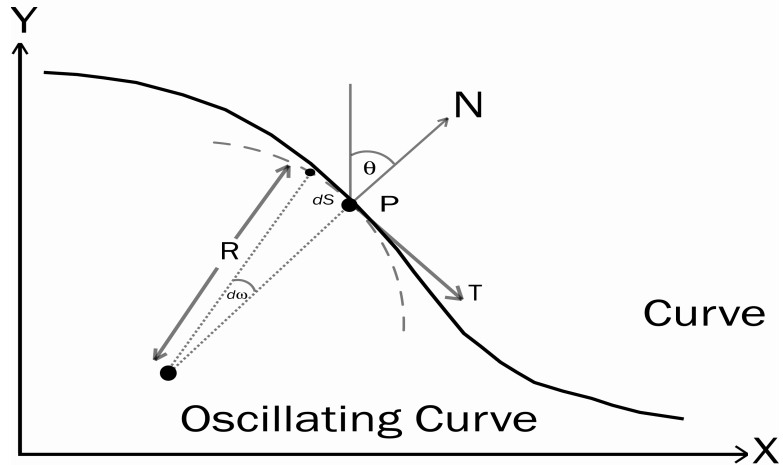
Figure 3.12 – Mathematical definition of curvature, where for a particular point *P*, curvature is defined by the radius of curvature, *R*, of the oscillating circle. Vector *N* is normal to the curve at point *P*. The curvature at point *P* is the reciprocal of the radius of curvature. From Roberts (2001).

Figure 3.13 displays curvature in a two-dimensional, cross-sectional view. Take the surface to be the interpreted picks for a horizon and the arrows to be vectors normal to the surface at any particular point of the surface. When the surface in question is flat or is a planar dipping surface, vectors will be parallel with each other and the surface will have zero curvature. Synclinal features within the horizon makes the vectors converge with each other, creating negative curvature. Anticlinal and ridge features have the vectors diverge from each other, defining positive curvature.

Figure 3.13 – Signing convention for curvature. Converging vector arrows over a syncline define negative curvature while arrows diverging over anticlines define positive curvature. Vector arrows perpendicular to a plane define zero curvature. Figure is taken from Roberts (2001).

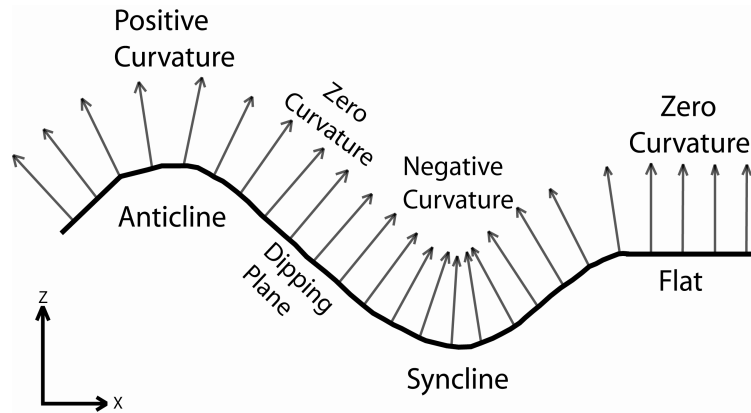Roberts (2001) extended the application of curvature into three-dimensions. Figure 3.14 shows curvature in three-dimensions. When a surface is cut by a plane, the intersection of the plane with the surface is a curve where the curvature can be extracted at any point along the curve. Normal curvature is a subset of curvatures that are defined by planes orthogonal to the surface. Combining normal curvatures defines different curvature characteristics that can relate to all surfaces.

The two principal curvature attributes are the maximum curvature, K_{max}, and minimum curvature, K_{min}, where K_{max} is the largest absolute curvature and K_{min} is the curve perpendicular to the maximum, having the smallest absolute curvature. Averaging the two principal curvatures gives K_{mean}. Gaussian curvature, K_{gauss}, is the product to the two principal curvatures, $K_{gauss}=K_{min} K_{max}$ (3-2). Gaussian curvature describes a property of a surface related to its bending, where no matter how a surface is bent, the Gaussian curvature remains constant, so long as a surface is not broken.

25

Maximum curvature is defined by the equation

$$K_{max} = K_{mean} + \sqrt{K_{mean}^2 - K_{gauss}} \;\; (3\text{-}3),$$

while K_{min} is defined by the equation:

$$K_{max} = K_{mean} - \sqrt{K_{mean}^2 - K_{gauss}} \;\; (3\text{-}4).$$

Mean curvature is not an effective visual attribute as it tends to be fairly similar to maximum curvature. Its importance is that it can be used to derive other curvature attributes.
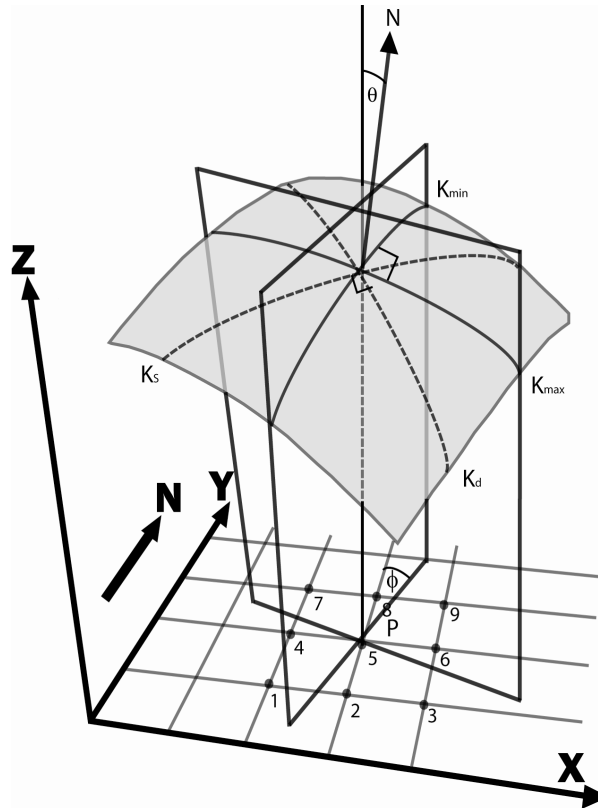
Figure 3.14 – Three-dimensional representation of curvature. **X** and **Y** are the map axes and **Z** is the time axis. Point P is the point where curvature is being computed. The dip angle is where **N**, the vector normal to the surface, is at an angle θ with the vertical plane. See text for a more complete discussion of the different types of curvature. Figure is taken from Roberts (2001).

Maximum curvature is useful in delineating faults and faults geometries, while minimum curvature is effective in imaging surfaces where there is potentially a fault or a fracture. From these curvature types, other curvatures can be derived. Figure 3.15 shows the different curvature types that can be derived from the mean and Gaussian curvature.

Figure 3.15 – Curvature shape classification, where combining mean and Gaussian curvature is used to describe local shape of a surface. (Roberts, 2001).

Most positive curvature, K_+, and most negative curvature, K_-, are curvature attributes derived from normal curvatures by searching the most positive and most negative values through the surface. From Figure 3.15, positive and negative curvature helps in delineating features that exhibit flexure.

CHAPTER 4

PROCESSING THE VACUUM-MALJAMAR FIELD DATA SET

The two major goals of this research are (1) to design a processing flow that will accentuate the image of the Vacuum-Maljamar Field data set and (2) to observe the impact of each processing step on volumetric seismic attributes. The sensitivity of these volumetric attributes to these processing parameters allow them to be used as a quality control measure that aid in choosing processing parameters. In this chapter, I focus on the processing of the shot gathers of the Vacuum Field data set.

Conoco-Phillips provided the unprocessed field shot data used during the course of this study. The data volume is the result of two separate acquisition programs, Maljamar and Vacuum. The prestack data set consists of four SEG-Y files totaling approximately 33 gigabytes in size. For the processing, I used the commercial seismic processing package SEISUP from Geocenter, Inc. and FOCUS from Paradigm Geophysical. I used processing codes from the Allied Geophysical Laboratories to generate the various attribute volumes.

4.1   Acquisition Parameters

The seismic survey for Vacuum-Maljamar acquired by Dawson Geophysical consists of:

- A spread configuration of 25 source lines and 37 receiver lines, with lines varying in length,

- 6 geophones per receiver group,

- Group interval of 220 ft (67 m) with a receiver line spacing of 1320 ft (402 m),

- Vibroseis source with a peak force of 50,000 lb (22,700 kg),

- A sweep length of 12 seconds,

- Minimum sweep of 8 Hz and maximum sweep of 90 Hz,

- Source interval of 220 ft (67 m) with a source line interval of 1540 ft (470 m),

- Total data length of 3.072 s two-way traveltime, and

- Sample rate of 2 ms.

4.2   Pre-Processing

Optimizing signal-to-noise (S/N) ratio is one of the goals of reflection seismic acquisition and processing. The acquisition X-, Y-, and Z- values of both shots and receivers are stored in the seismic trace headers. In spite of the SEGY "standard", many trace header values needed for processing were not stored in the headers. Particularly, the commercial processing packages I used require shot and receiver line numbers to properly sort the data. These values are not part of a standard SEGY trace header and not recorded in the prestack trace header. Field observer notes are ascribed as lost in antiquity.

As a preliminary step, I generate a map of the shots and receivers using the unmodified data set (Figure 4.1). There is clearly something wrong with the extracted data. The display shows no apparent correlation between the blue shot lines and the red receiver lines. A map from Conoco-Phillips verifies this assumption of missing information (Figure 4.2).

I used a C program to compute the receiver bin numbers from the X and Y coordinates. Geometry information can now be extracted from the headers after the correction. The correct locations of the shots and receivers are shown in Figure 4.3. The corresponding fold map generated is shown in Figure 4.4.
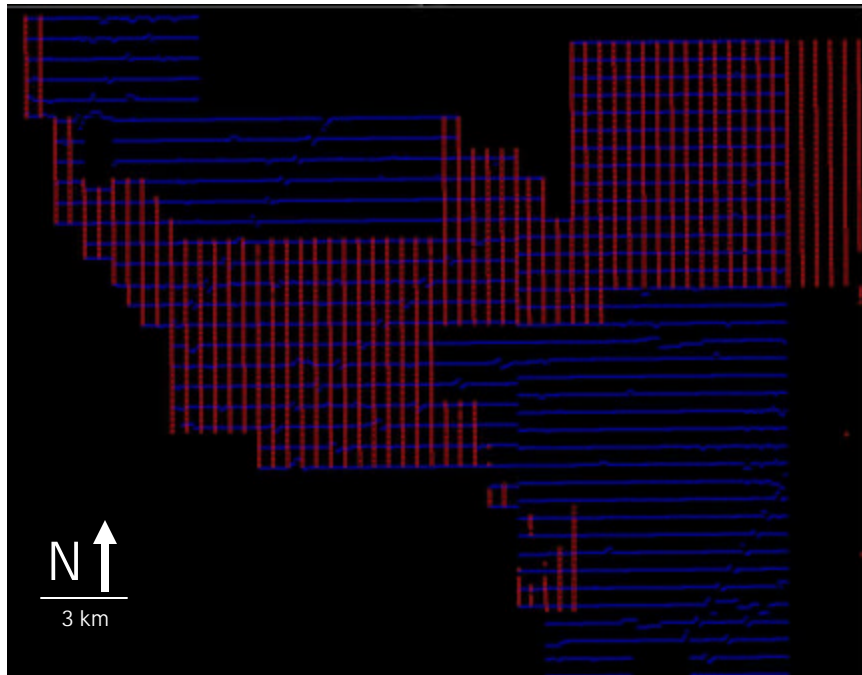
Figure 4.1 – A shot/receiver map of the data. The shot lines are oriented east-west and displayed in blue. The receivers are oriented north-south and displayed in red..

My next quality control step was to check for spherical divergence. Seismic amplitude decreases with time due to geometric spreading, absorption, and energy loss at reflection interfaces (Sheriff, 2002). To check for this, I examine a common shot gather of the data with no automatic gain control (AGC) applied (Figure 4.5). The amplitudes of both the shallow and deep reflectors appear to be well-balanced. No loss in the amplitude of the deeper data is observed, and from this, I concluded that spherical divergence correction has been previously applied to the data.
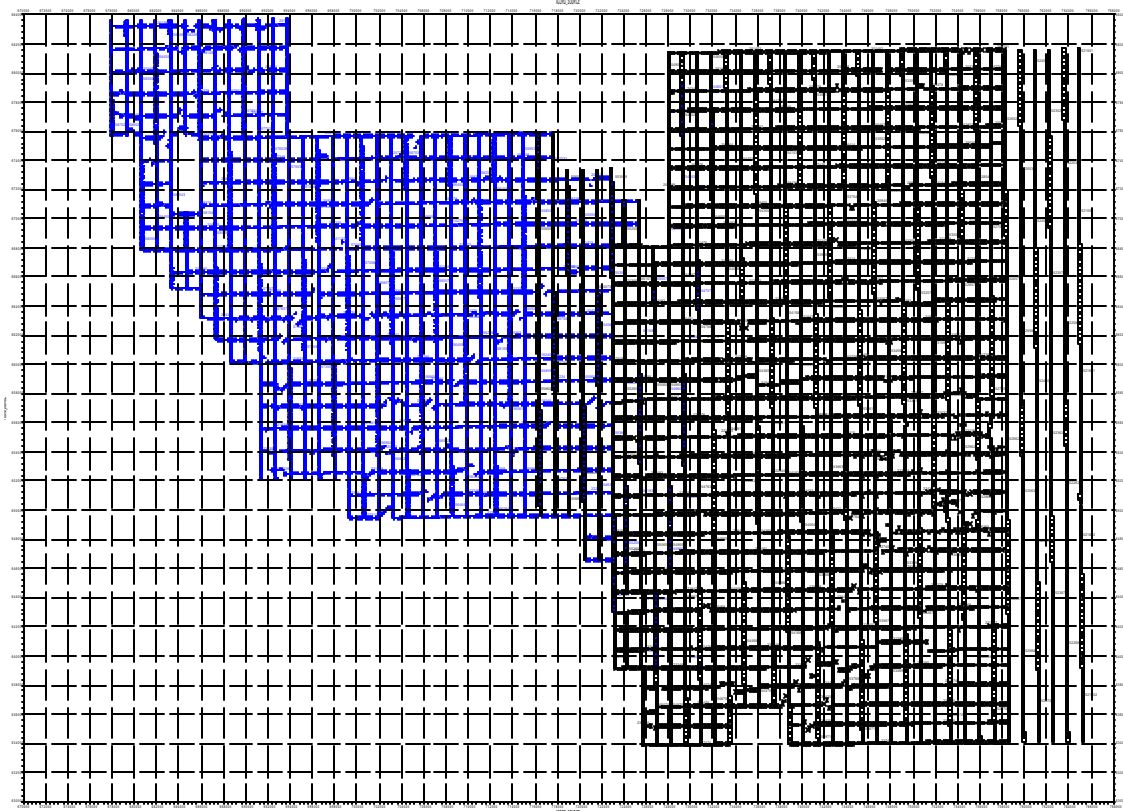
Figure 4.2 – Layout of the shots and receivers of the merged Maljamar (blue) and Vacuum (black) survey. Shot lines are oriented East-West, while receiver lines are oriented North-South. Image is courtesy of Conoco-Phillips
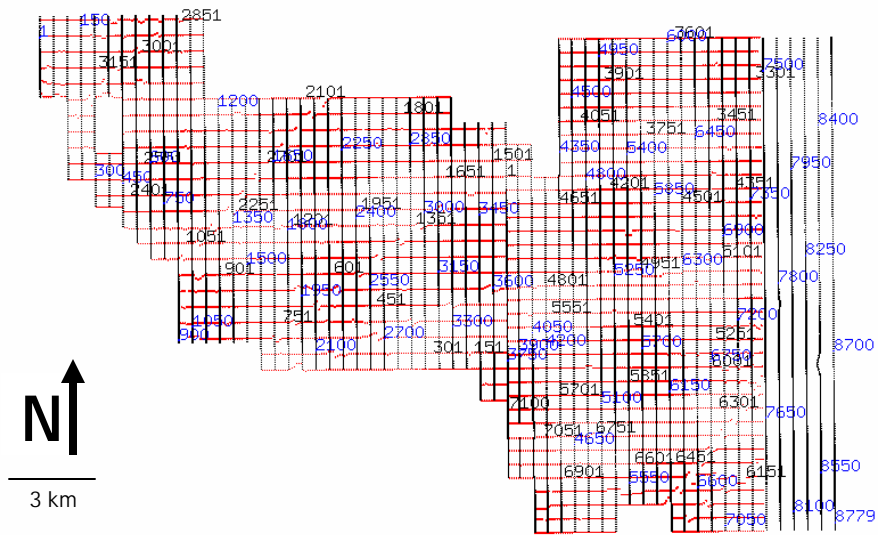
Figure 4.3 – The corrected shot and receiver stations of the Vacuum-Maljamar survey. Shots (red) fall along E-W shot lines, and receivers fall along the N-S receiver lines.

| 0.0 | 4.4 | 8.8 | 13.2 | 17.7 | 22.1 | 26.5 | 30.9 | 35.3 | 39.8 | 44.2 | 48.6 | 53.0 |
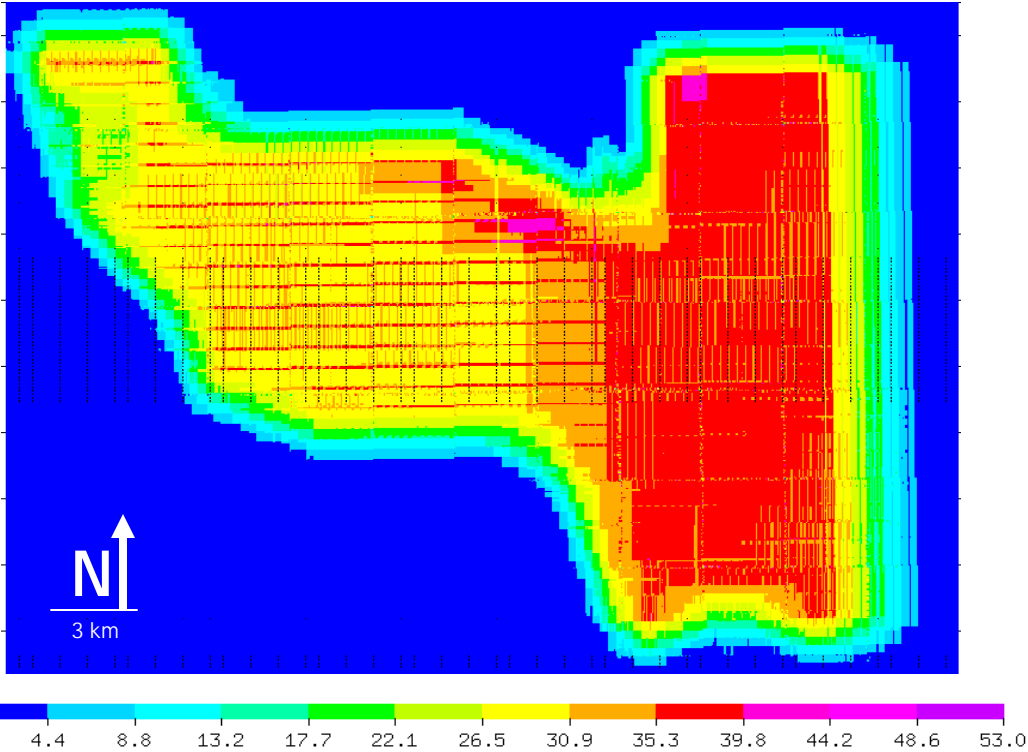
Figure 4.4 – Fold map of the Vacuum-Maljamar survey. The highest fold number is 36.
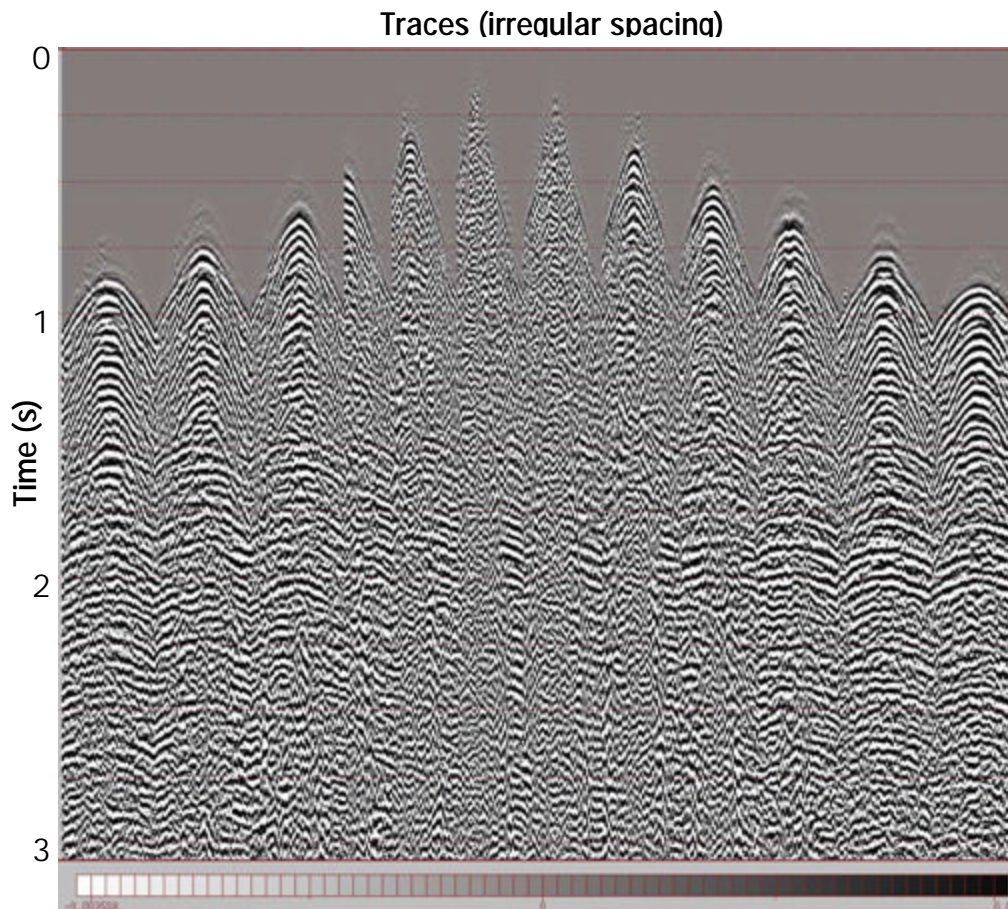
Figure 4.5 – A common shot gather of the Vacuum-Maljamar data set with no AGC applied. The amplitudes of the shallow and deep reflectors are balanced, implying that spherical divergence had been previously applied.

4.3   Reduction of Ground Roll

Rayleigh waves (commonly referred to as ground roll) come from the coupling of compressional (P) waves with the vertical component of shear waves (SV) traveling along a free surface (Yilmaz, 1987). Ground roll is typically characterized by low-frequency, high amplitude, low velocity, and strong back-scattering due to inhomogeneities near the surface.

The Vacuum-Maljamar data can be classified as having average to low signal-to-noise ratio. Reflections are seen to be continuous in the far offsets. In the near offsets,

these reflections are completely masked by ground roll (Figure 4.6). I identify several

velocity components of the ground roll, ranging from 1500 fps to 2000 fps (457 m/s to

610 m/s).
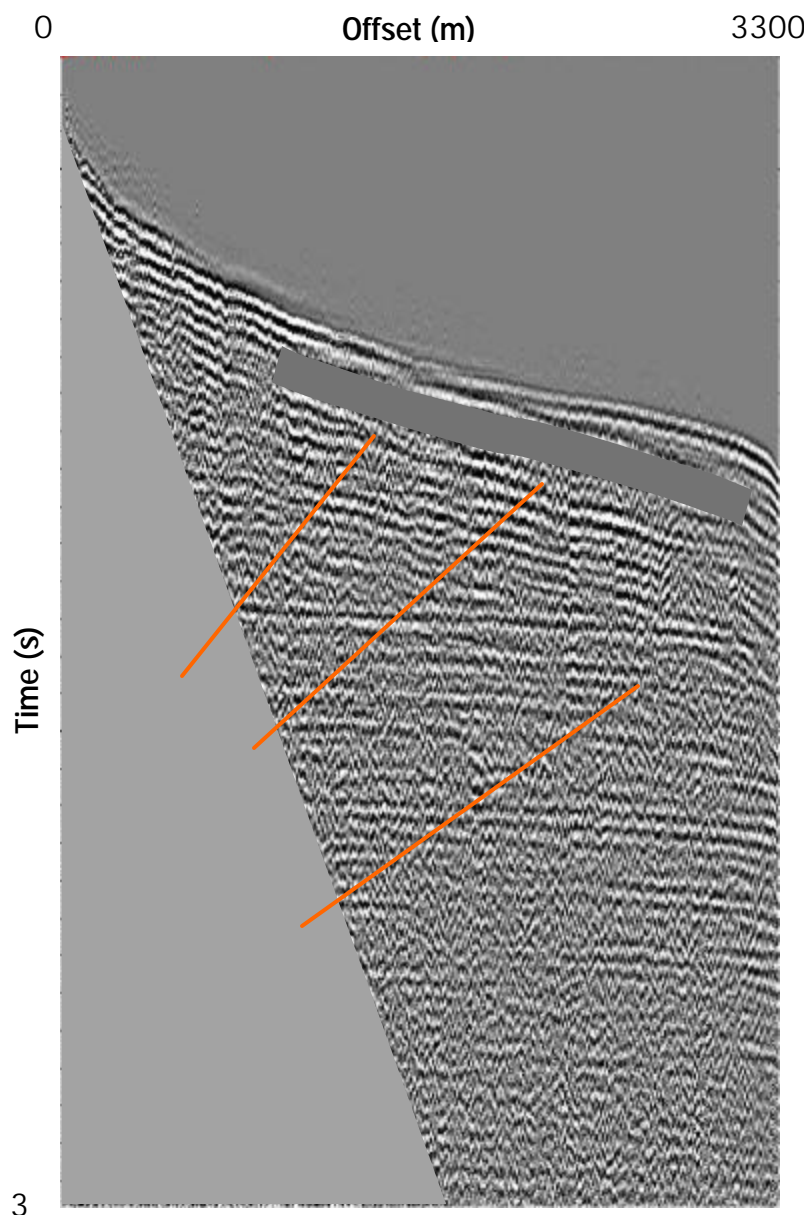
Figure 4.6 – Shot gather shown in Figure 4.5, now sorted by increasing source-receiver offset. The highly-aliased ground roll distorts the continuity of the reflectors in the near-offset traces (red triangle). Sorting results in the irregular trace spacing for the 3D spread. Head waves are indicated in the shot gather (teal box). Orange lines indicate the back-scattered noise component.

I follow the workflow used by D'Agosto et al. (2003) to remove the ground roll. I first flatten the ground roll by applying a linear moveout correction using a velocity of 2000 ft/s (610 m/s) (Figure 4.7). The signal is enhanced by extracting the coherent signal along the dominant dip direction and then summing the signal with the original trace. The dominant dip direction is calculated by measuring the maximum coherency along a range of dips from surrounding traces at each sample. No signal will be extracted if the maximum coherency is less than a user-specified threshold level. Coherency is then measured between the output signal and the original trace and is used to calculate a weight to apply to the signal prior to summing with the original trace.

To remove different velocity components, I apply the filter process in a cascading manner. I first applied a filter using an 1800 ft/s (550 m/s) linear velocity followed by a filter at 1700 ft/s (520 m/s), and down to the 1500 ft/s (457 m/s). After each application of the filter, I subtracted the output volume from the preceding volume in order to generate a noise volume. This acts as a quality control step after each filter to check if any desired reflections have been filtered out. With no obvious reflectors appearing in the noise volume, the filter process did not kill any signal and removed only noise. Figures 4.7 to 4.11 show the cascading filtering method applied on the Vacuum-Maljamar data set, with Figures 4.7a – 4.11a figures displaying the resulting filtered volumes from the preceding volume and Figures 4.7b – 4.11b showing the subtracted noise volume.
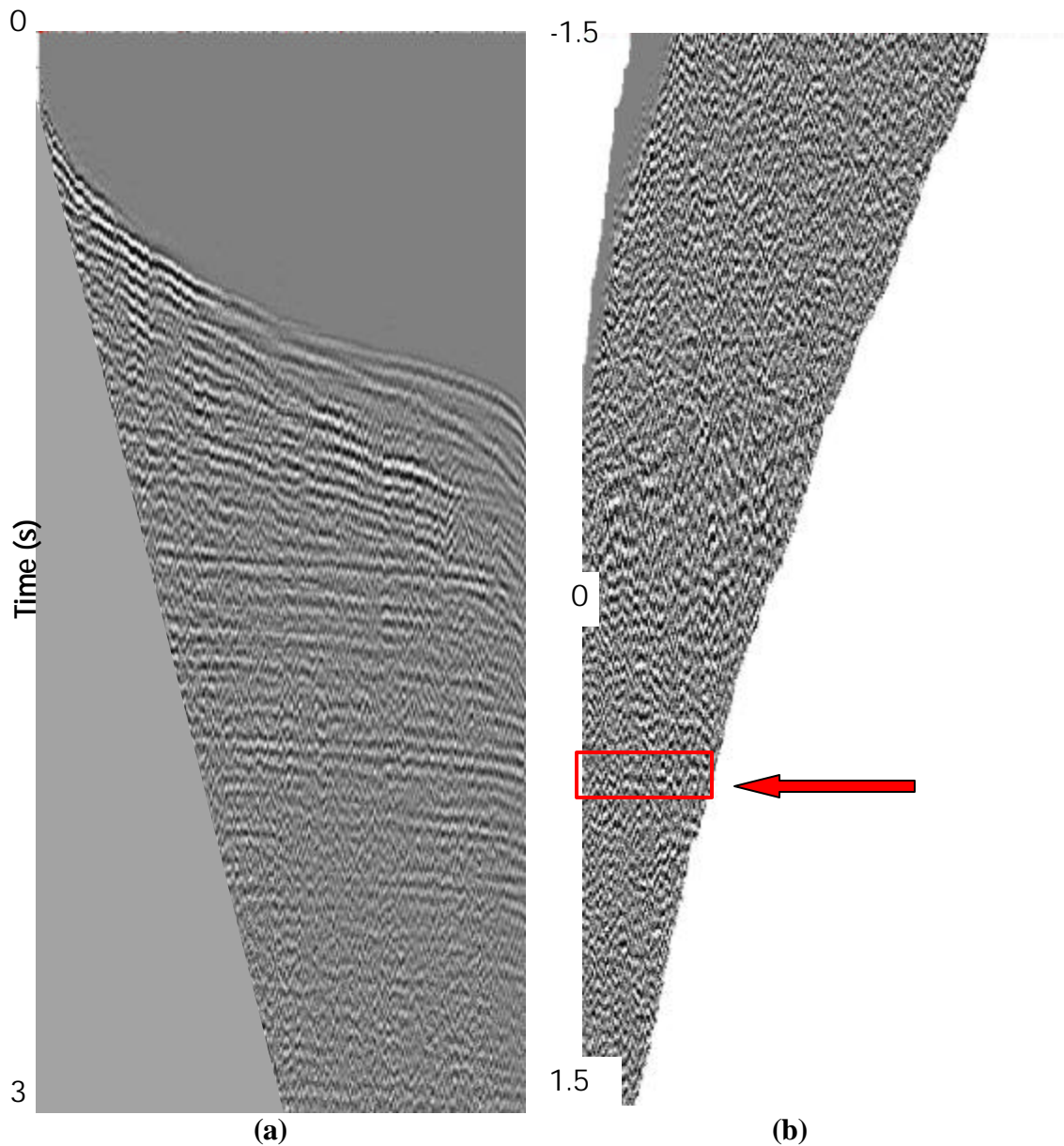
Figure 4.7 – Linear moveout (LMO) process to determine the linear moveout velocity of the different components of the ground roll. (a) The original data with the red triangle highlighting the ground roll noise cone. (b) The LMO-corrected data, with red arrows pointing to flattened ground roll components.

In Figure 4.8a, I encircle the aliased (red circle) portion of the forward propagating noise. In Figure 4.9b, which is the filtered noise of Figure 4.8a, I have encircled (red circle) that same aliased noise train that has been filtered out. This is

another QC step to verify that only coherent noise is filtered out and not the signal. This can also be seen in following images.

(a)   **(b)**
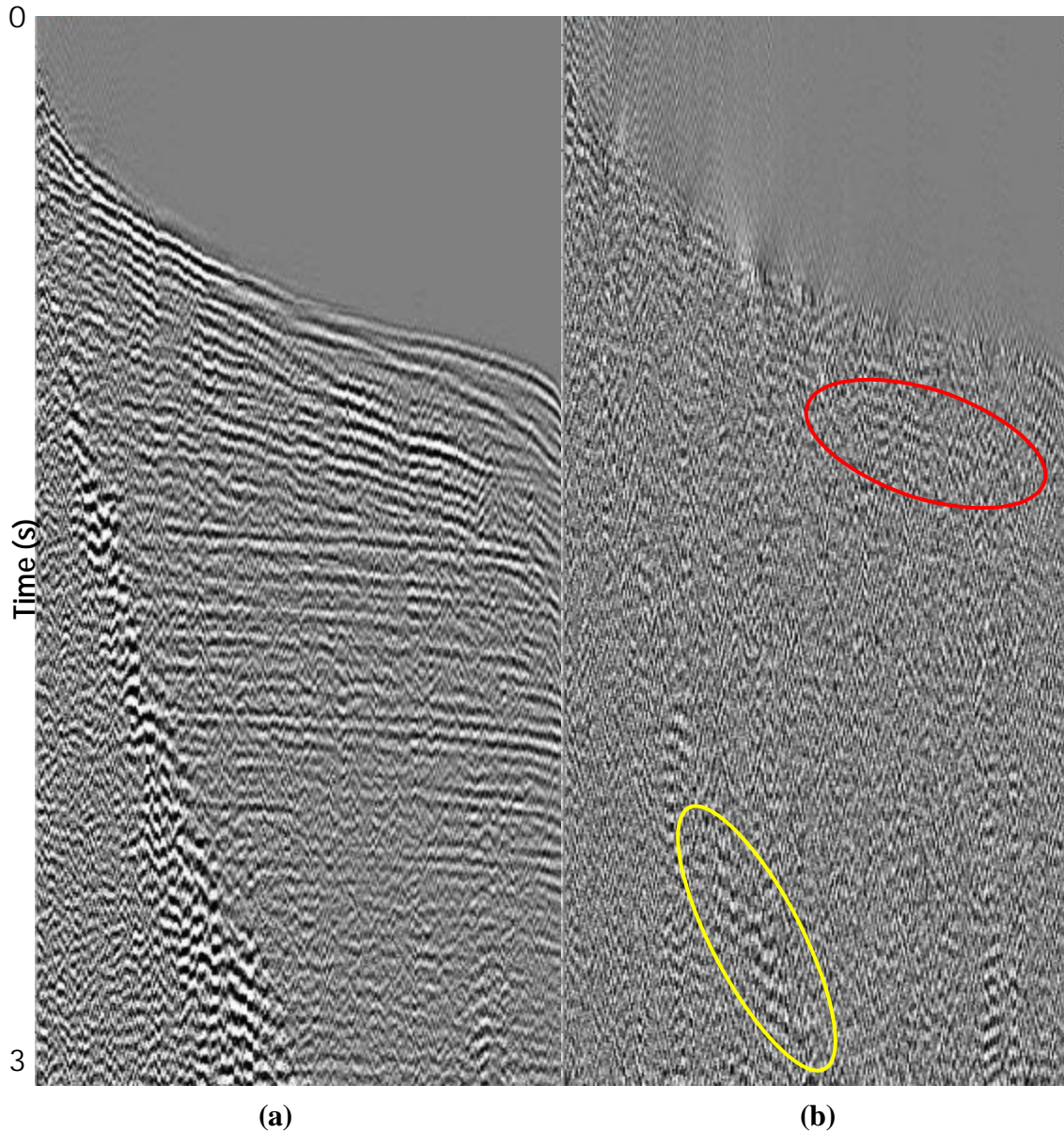
Figure 4.8 – The first pass of the linear moveout removal of ground roll. (a) The resulting data volume after the removal of the 1800 ft/s (550 m/s) component of ground roll; (b) the modeled noise volume removed from the seismic data obtained by subtracting from Figure 4.6. Some of the shallower dip energy (signal in red, noise in yellow) has also been rejected due to aliasing.
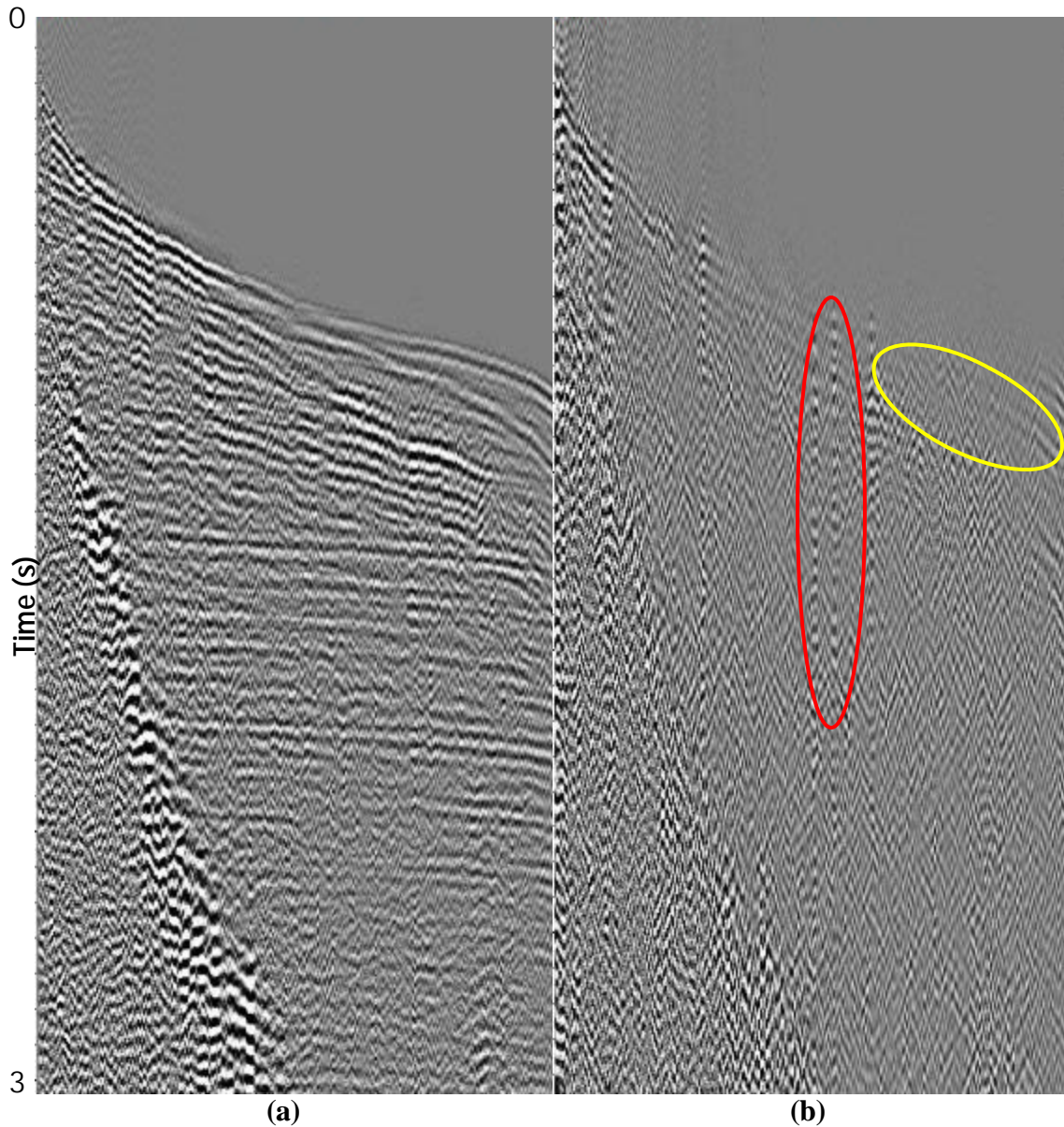
Figure 4.9 – (a) Result of removing the 1700 ft/s (520 m/s) component from the data displayed in Figure 4.8a. (b) The rejected noise obtained by subtracting the data shown in (a) from the data shown in Figure 4.8a. I interpret the "ground roll", indicated by the red circle, to be generated by head waves scattering off near-surface heterogeneities. The yellow circle indicates long offset reflectors that have leaked through the filter due to aliasing.
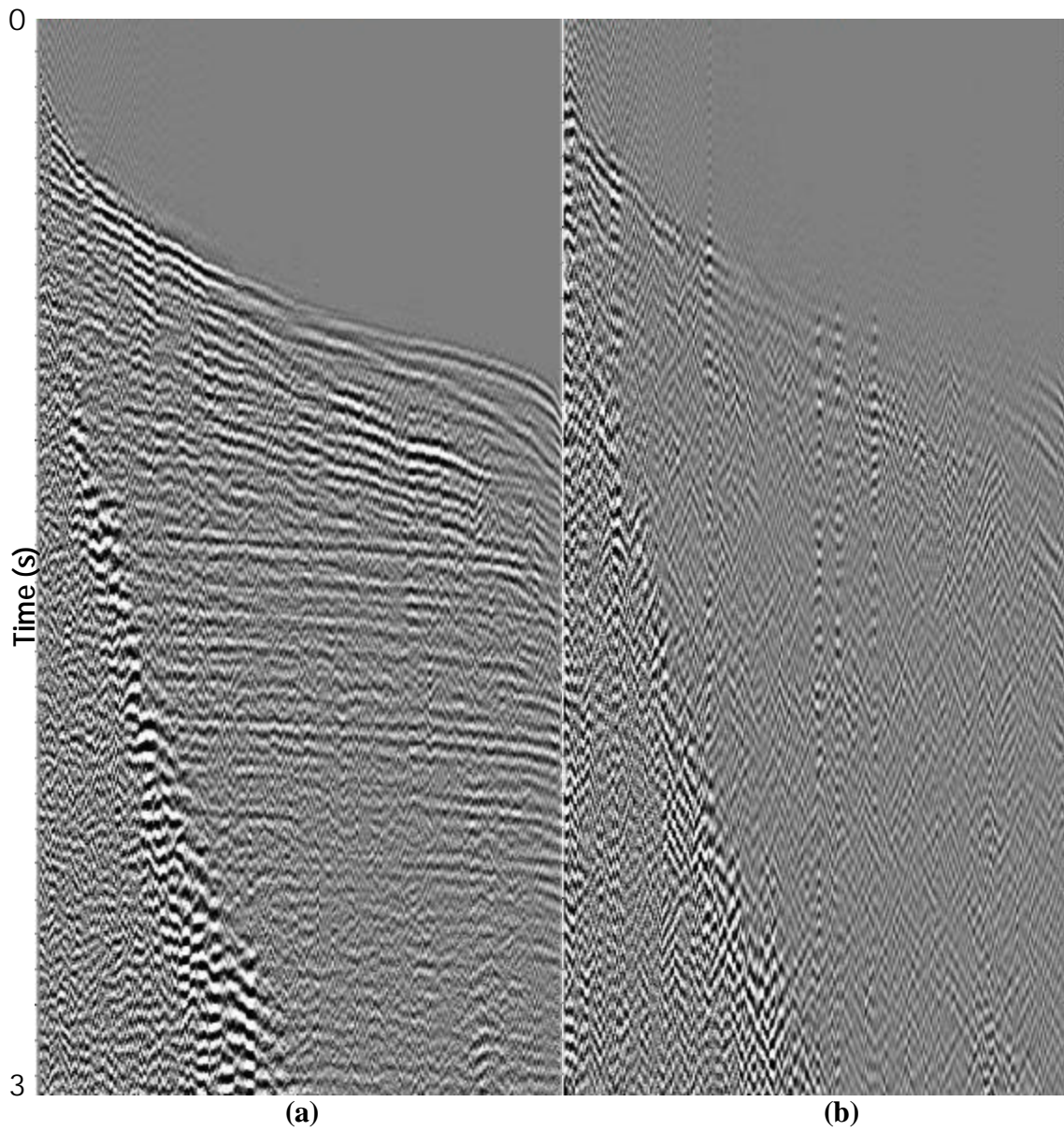
Figure 4.10 – (a) Result of removing the 1600 ft/s (487 m/s) component of the ground roll from Figure 4.9a. (b) The difference between the data volume shown in Figure 4.9a and (a).
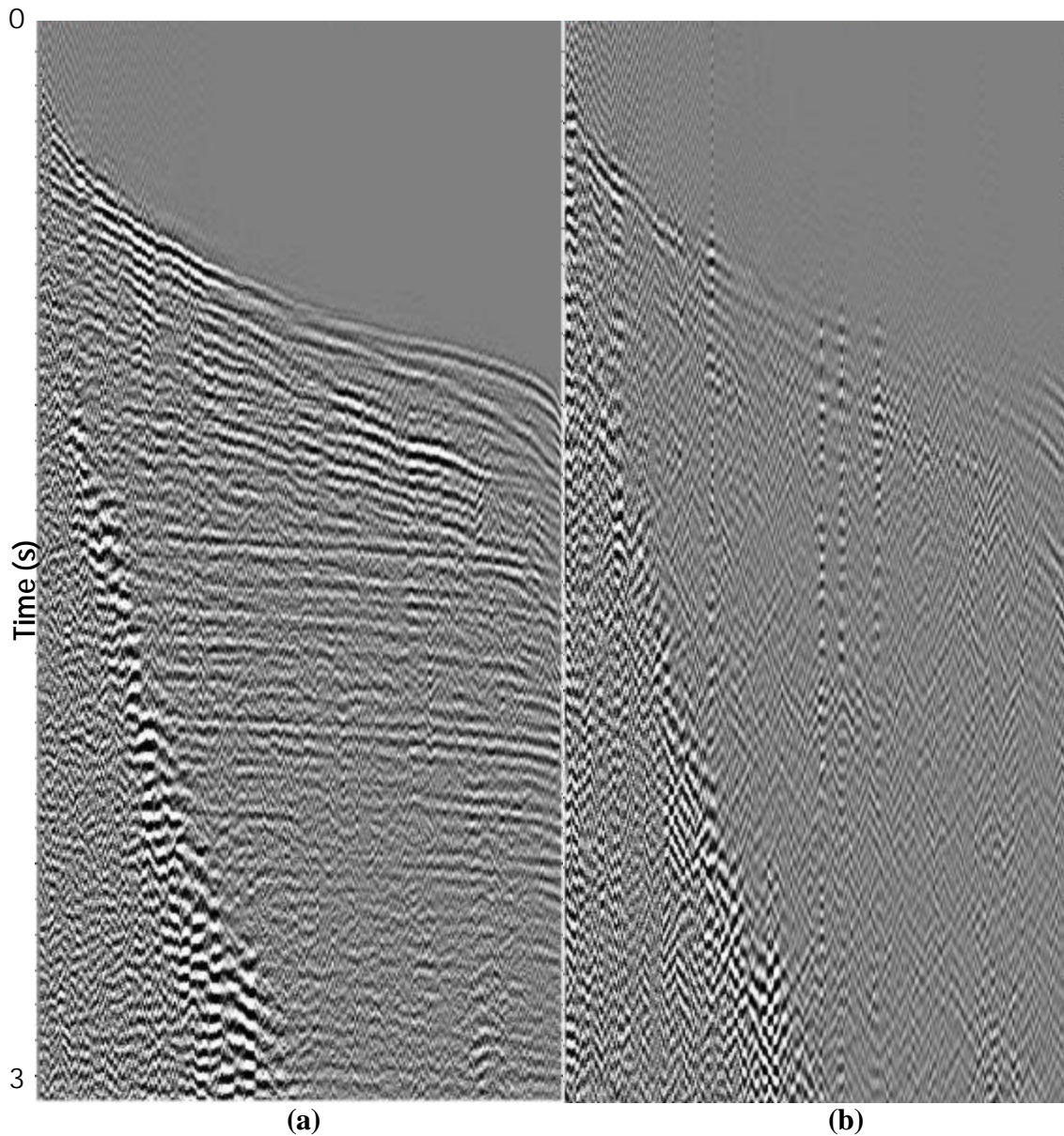
Figure 4.11 – (a) Result of filtering the 1500 **f**/s (457 m/s) component of ground roll from Figure 4.10a. (b) The difference between Figure 4.10a and (a).

Despite the cascading manner of application of the filter, part of the noise cone remains. In order to eliminate this, I applied an inner mute to remove the residual noise cone to improve the final images of the data.
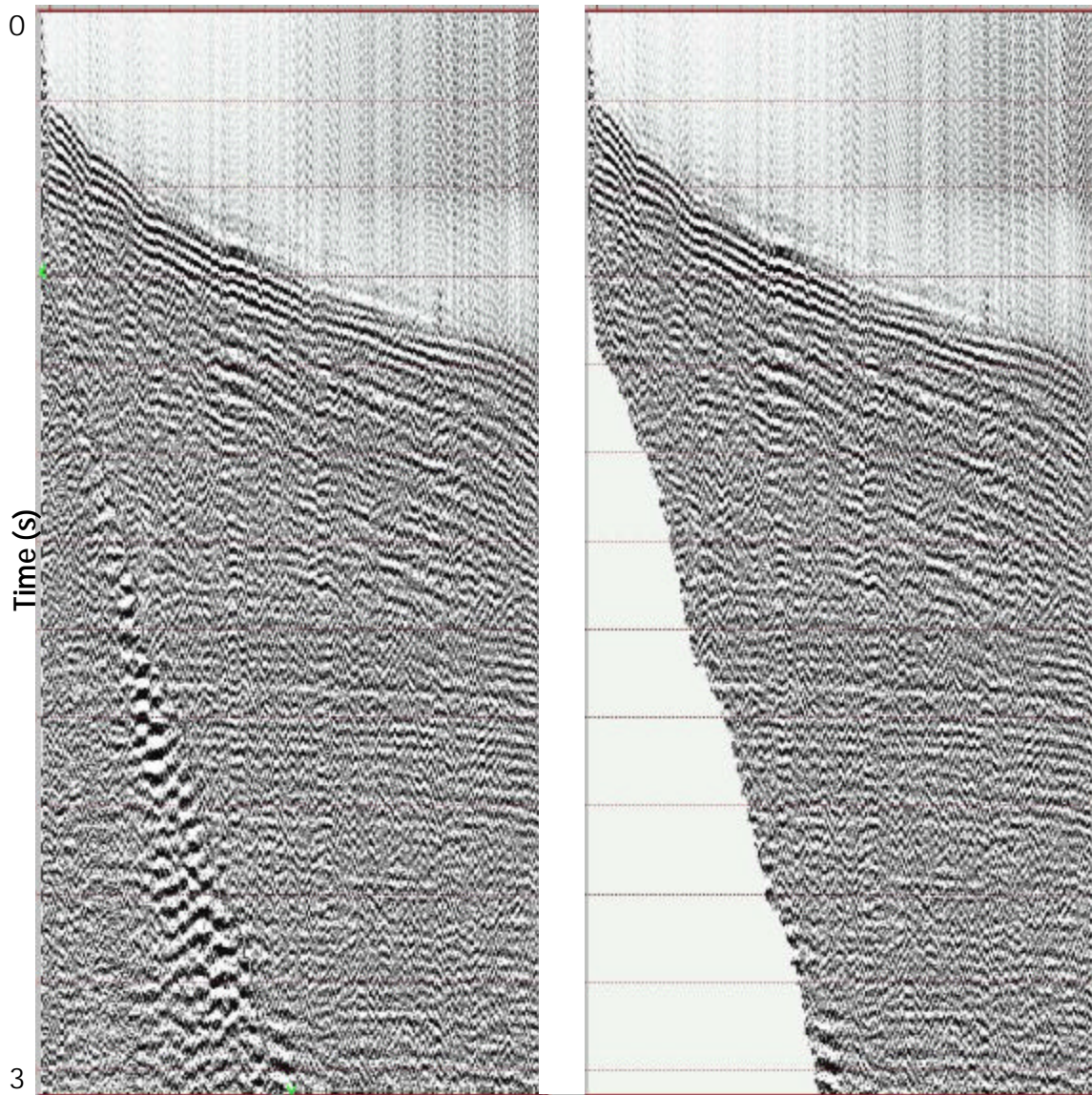
Figure 4.12 – Inside mute of the residual ground roll cone. This improves the signal-to-noise ratio and helps in subsequent steps in the processing stream, especially in estimating velocities.
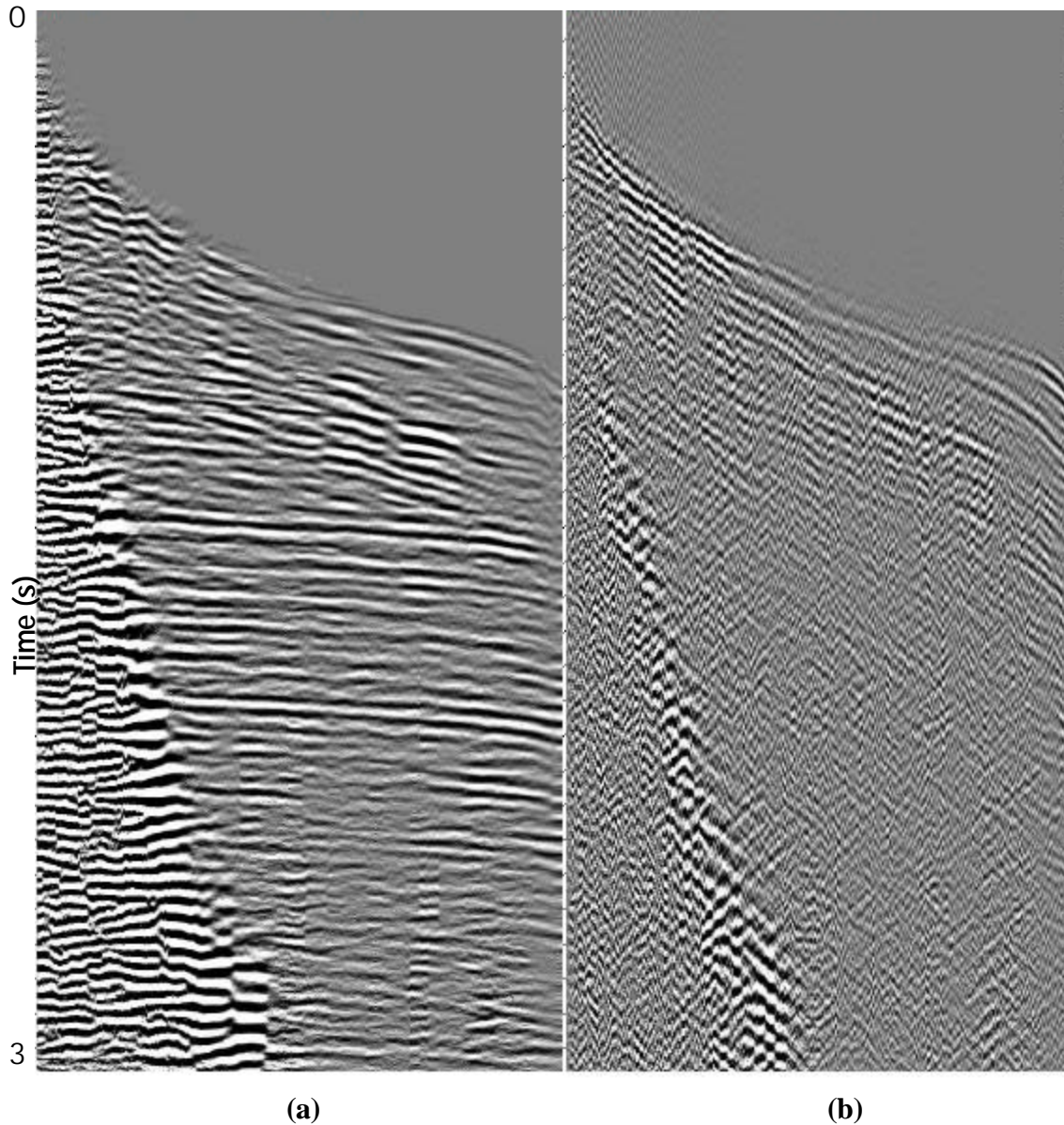
Figure 4.13 – Head wave filtering. Figure 4.13(a) shows the data volume after filtering out head waves. Figure 4.13(b) displays the modeled head waves filtered out. No part of the signal has been filtered out as seen in 4.13(b).

This workflow has proved effective in removing most of the coherent noise in the data and helps in the subsequent processing stream, especially velocity analysis. The near-traces are not as masked by the ground roll and the coherence of the signal is heightened, leading to better velocity picks. The residual incoherent noise train had no

effect in the velocity analysis. One drawback to this method I particularly do not like is that it lowers the frequency of the output data, which goes counter to the objective of this project.

4.4   Shot-consistent Deconvolution

Deconvolution was applied to the ground roll filtered data volume. The head wave filtering process degraded the data to a lower frequency, giving it a "wormy appearance." Deconvolution restores the seismic character of the data by preserving the frequency content of the data and reduces the residual low-frequency components that were not removed by the dip filters during ground roll filtering.

For the Vacuum-Maljamar data, I used the module FOCUS module SHDCON to perform a time-variant source signature deconvolution. SHDCON estimates the source wavelet of the seismic record, designs a filter and deconvolves the data (FOCUS Users Guide, 2005). Deconvolution in the frequency domain allows for editing of the frequency and after estimation of the operator, the low and high end frequencies can be limited in order to improve the S/N ratio of the output. Figure 4.14 shows the pre- and post-deconvolution seismic volume.
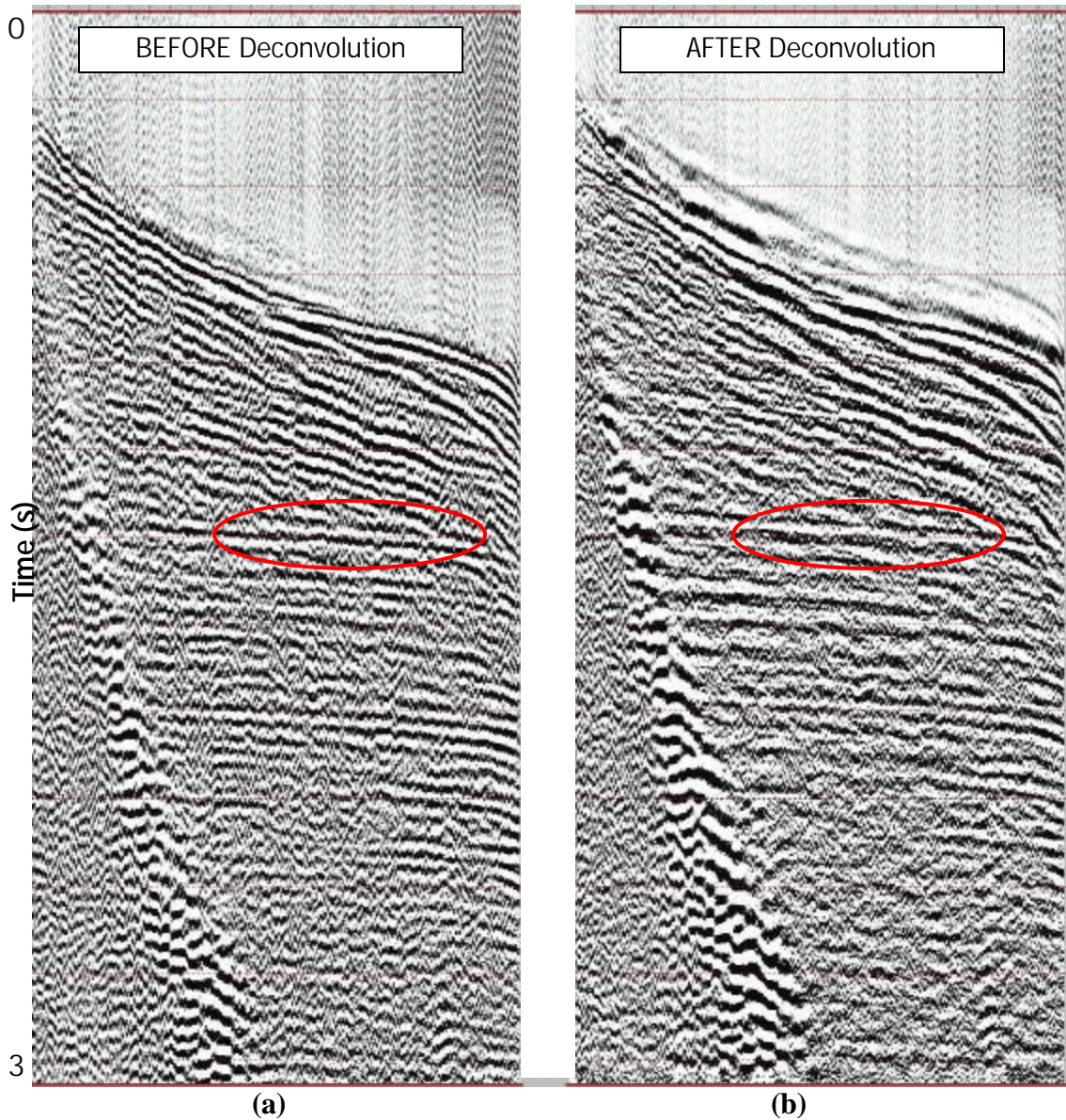
Figure 4.14 – Comparison of the seismic character of the data volume (a) pre- and (b) post-deconvolution. After deconvolution, the data has better seismic character and higher frequency (red circle).

4.5 Residual Static Correction

Sheriff (2002) defines statics as "corrections applied to seismic data to compensate for the effects of variations in elevation, near‑surface low‑velocity layer thickness, weathering velocity, and reference to a datum." The goal of statics corrections

is to shift each seismic trace by a constant time to approximate data measured on a flat plane without the presence of a low-velocity layer. Static corrections are assumed to be time-invariant, surface consistent, and independent of frequency. Surface consistent means that the same static values are applied to a particular source or receiver, depending on where it is located on the map.

(a)   (b)
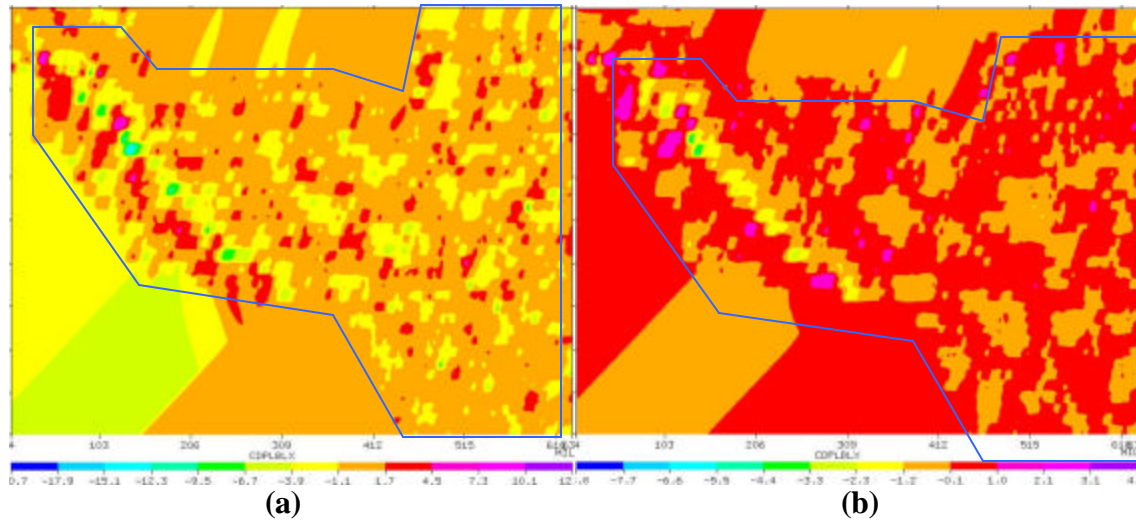
Figure 4.15 – Residual static correction for the shots with (a) the correction applied for the first run and (b) the total correction applied for the second run. The shape of the survey is outlined.

(a)   (b)
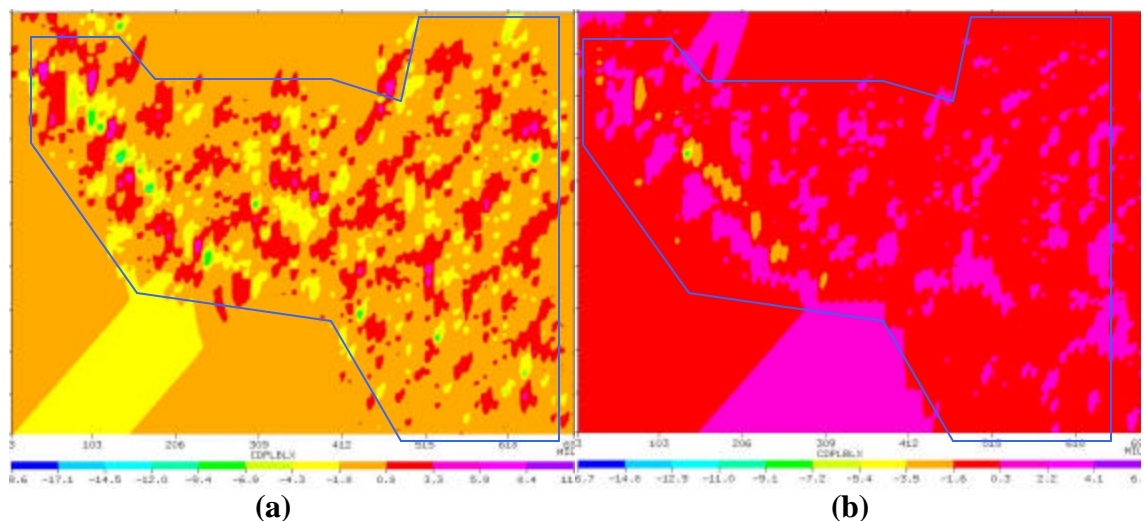
Figure 4.16 – Residual static correction for receiver with (a) showing the total correction applied for the first run and (b) the total correction applied for the second run. The shape of the survey is outlined.

45

I apply two passes of static correction to the Vacuum-Maljamar data set. The amount of correction to both source and receiver domains are shown in Figure 4.15 (source) and 4.16 (receiver). The first static run for the sources have corrections ranging from -12 ms to 10 ms, and the second run ranging from -3 ms to 3 ms. For the receivers, the first run correction ranges from -9 ms to 8 ms and the second run from -7 ms to 0.5 ms.

For both the sources and receivers, the first run of statics has a significantly larger range of the total shift compared to the second run. This implies that most of the shift was calculated in the first run and very little correction was done during the second run.

Figure 4.17 compares the difference between static corrected and uncorrected stacked sections. Figure 4.17a is a CDP stack *without* static correction and 4.17b is *with* static correction. The reflectors in the static-corrected stack show definition than in the uncorrected volume (teal box). This is particularly obvious in the shallow reflectors (yellow box). The reflectors are also more continuous in the corrected stack (red box). The same observations can be said about the deeper reflectors.
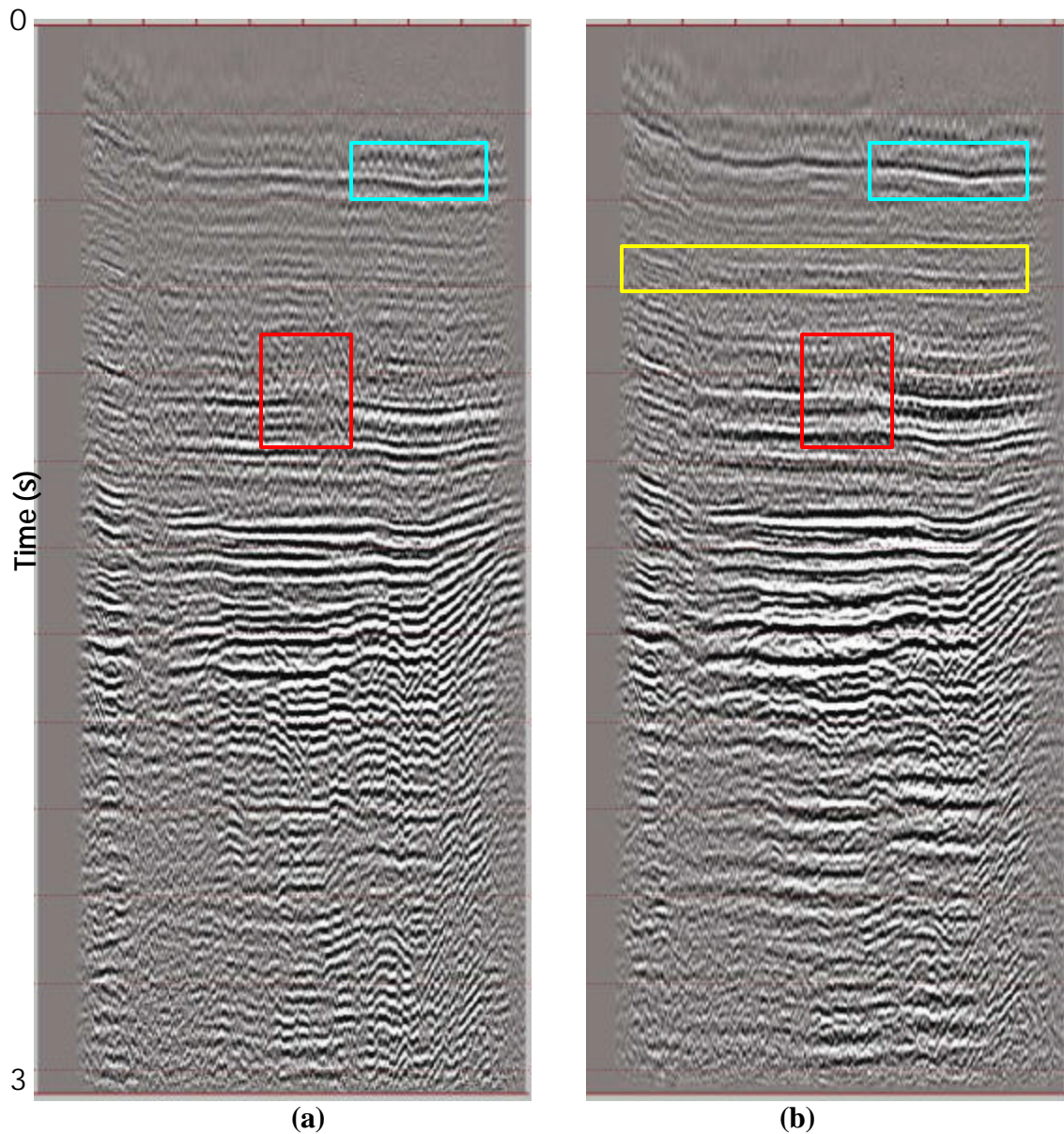
Figure 4.17 – A CDP stack displaying the Vacuum-Maljamar volume (a) with no static corrections and (b) with static corrections. The red box highlights a reflector that shows more continuity in the middle of the section in the section where static correction is applied. The teal box shows a shallow reflector that has better definition in the static-corrected section.

4.6 Velocity Analysis

To estimate velocities, data must be recorded at nonzero offsets and then sorted into common-midpoint gathers. These velocities can then be used to adjust for the

47

nonzero offsets and stack the seismic volume (Yilmaz, 1987). The normal moveout correction is used to check for the validity of the estimated velocity values. If the statics corrections have been applied, the structure is not too complex, and the offsets are small, hyperbolic approximation for traveltime works well.

As a QC step prior to detailed velocity analysis, I utilized a single velocity function for the entire survey (Figure 4.18). I will use the migrated image corresponding to this single velocity function as the baseline for all following migration volumes.

For the Vacuum-Maljamar data, I picked velocities from the velocity spectrum, where the coherency of the signal is displayed side-by-side with a graph of *velocity* vs. *zero-offset time* (Figure 4.19). The coherency of the CMP gather is computed in small time gates following a hyperbolic trajectory (Yilmaz, 1987). The stacking velocities are determined by selecting the velocity function that has the highest coherency with important event amplitudes. I ran two-passes of velocity analysis, with the first run on a coarse grid of 100 x 100 grid and the second run on a 50 x 50 grid.

Using the VELDEF module in FOCUS, I was able to determine interval velocities I used for quality control purposes using the Dix method:

$$V_{\mathrm{int}erval} = \sqrt{\frac{(V_{n+1}T_{n+1}) - (V^2{}_n T_n)}{T_{n+1} - T_n}} \text{, where:}$$

V_{interval}: Dix interval between two T-V_{rms} pairs,

T_n, V_n: are the time and V_{rms} of shallow control point, and

T_{n+1}, Vn_{+1}: are the time and V_{rms} of deeper control point (FOCUS Users Guide, 2005).
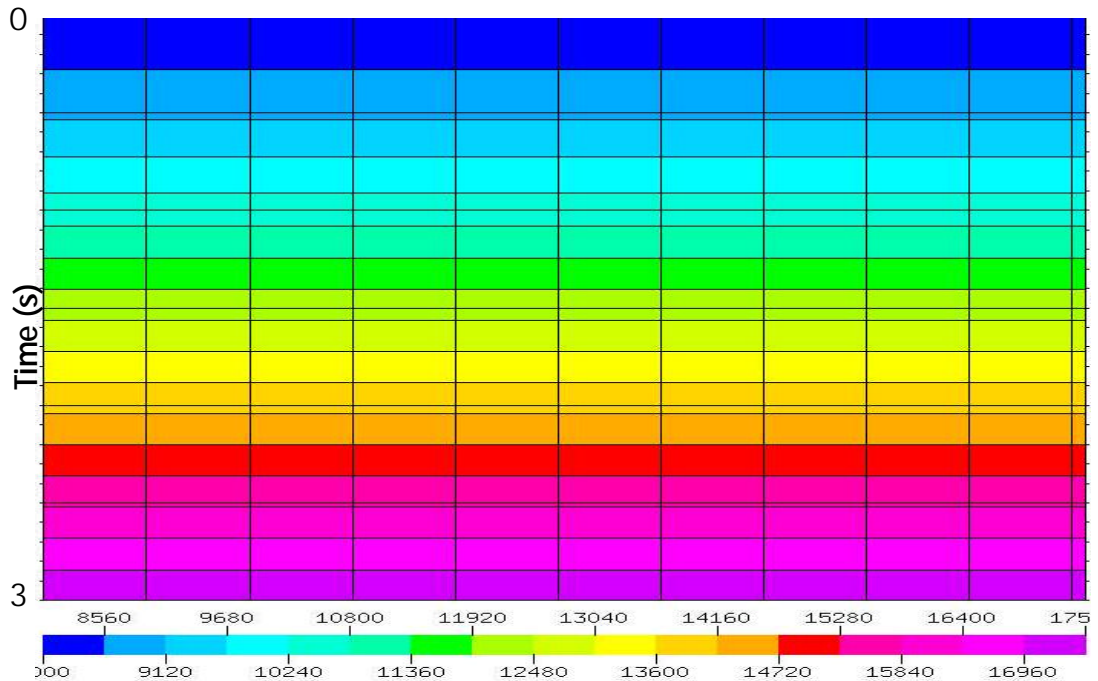
Figure 4.18 – Single velocity function used for the brute stack and migration. The output migration using this velocity function is used as the baseline volume for all proceeding volumes.

Figure 4.20 displays the velocity function picked on the coarse 100 x 100 CDP grid. The velocity function is relatively smooth and is comparable to the single function used for the brute migration. The relative smoothness of the velocity picks implies that the area is not a structurally complex and most of the reflectors are planar.

Figure 4.21 is a triangulation grid of the velocity picks. I use this grid as another quality control point to check the quality of the picks made on the velocity spectrum. This is complementary with the velocity profile of the picked velocity function. In the figure, the velocities are smooth throughout the whole survey and there are no picks that look out of place and edges of the survey are well-constrained.
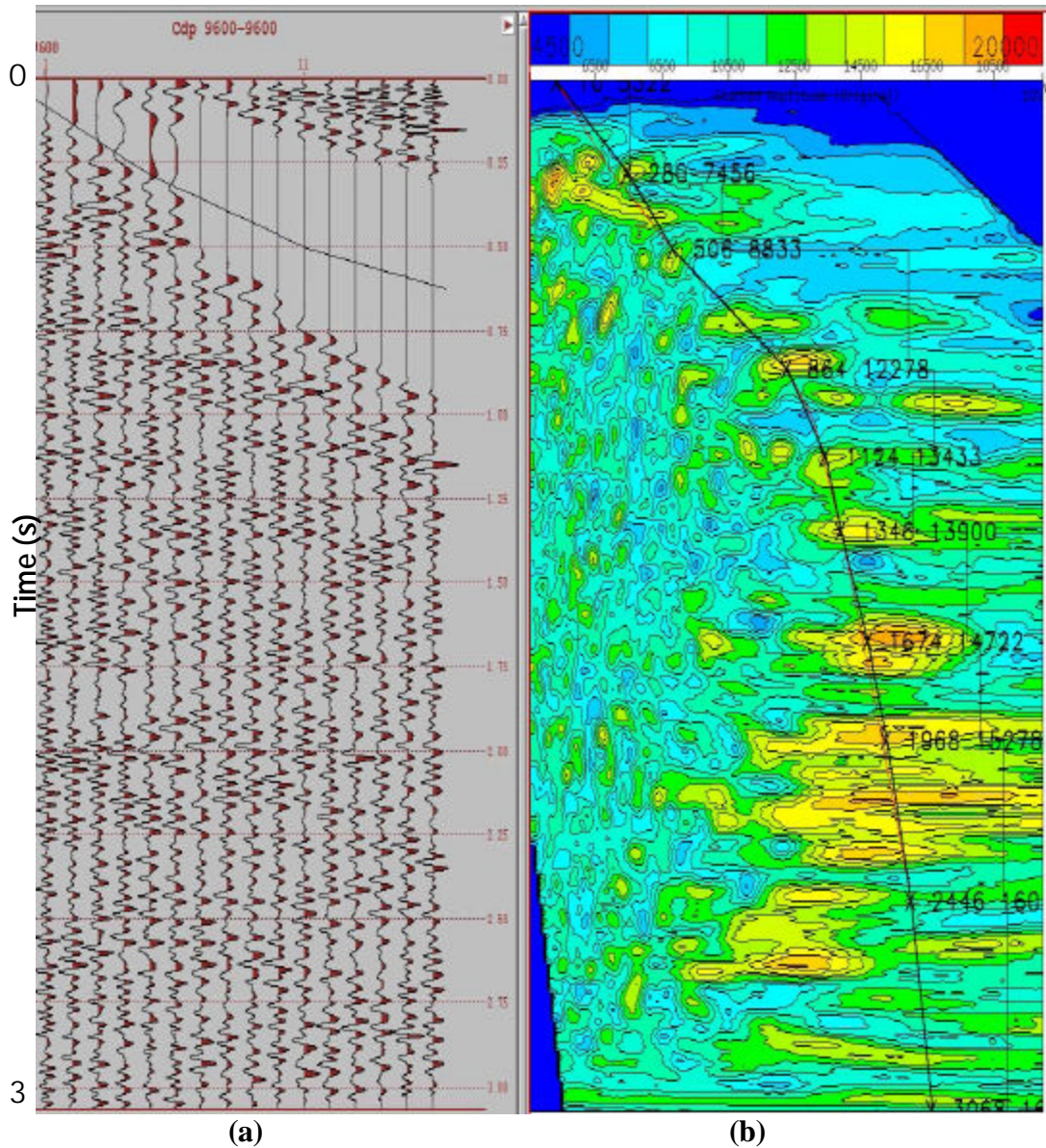
Figure 4.19 – Velocity estimation using the velocity spectrum. The panel on the left (a) is an unflattened wiggle plot of the data and the right panel (b) is a semblance plot of the seismic. The "bulls-eyes" on the semblance plot are parts of the seismic that has the highest semblance.
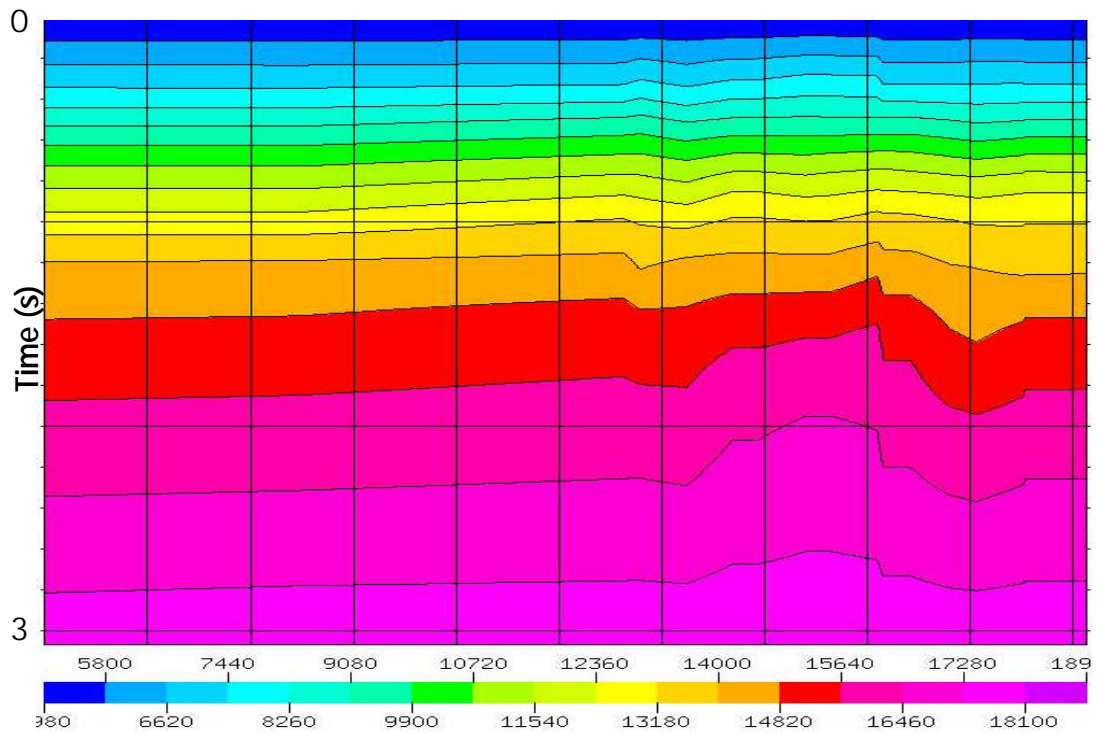
Figure 4.20 – Velocity pick based on a 100 x 100 grid. The smoothness of the velocity function implies that the area in question is not structurally complex and reflectors are planar (flat).
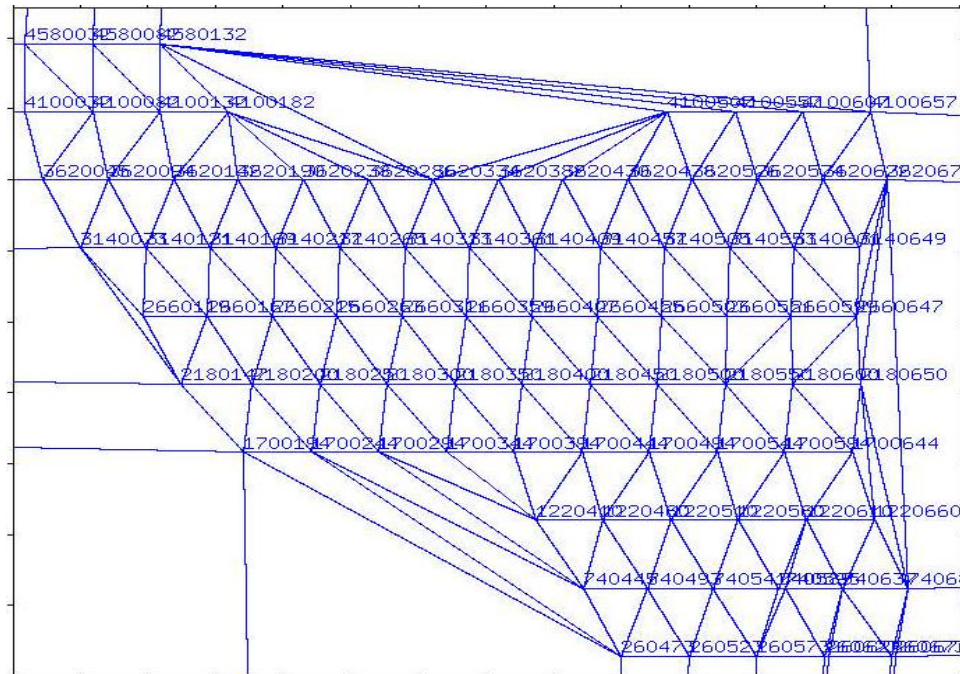
Figure 4.21 – Velocity grid triangulation across the survey. This display of velocity picking over the survey acts as a QC step to see there is no abnormal velocity pick across the survey, especially along the edges.

4.7   Migration

Migration is the process of moving reflectors and diffractors into their true location (Sheriff, 2002). I performed an *Omega-x* migration, a variation of the finite-difference migration, to the Vacuum-Maljamar data. *Omega-x* migration is algorithm that can handle steep dips and lateral velocity variations (Yilmaz, 1987). Figures 4.23 to 4.27 are displays of the same line A-A' as highlighted in figure 4.22.

52
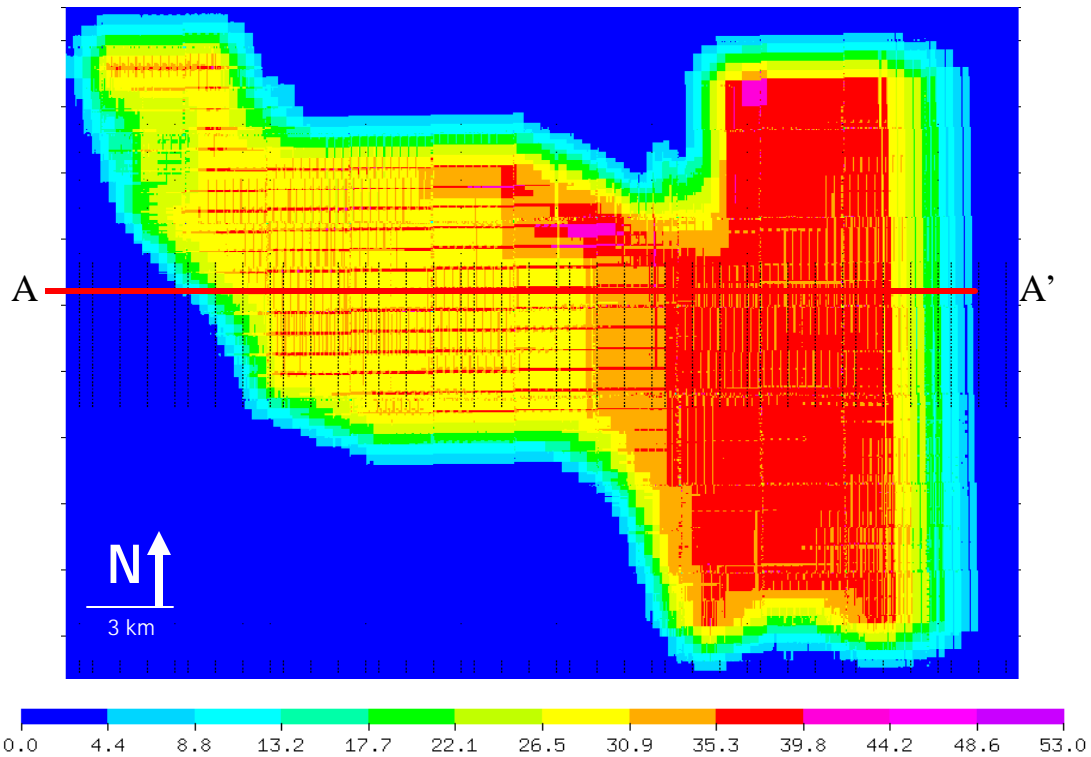
Figure 4.22 – Location of line A-A' superimposed over a map of the fold and inline and crossline numbers.

Figure 4.23 is a section from the brute migration. Despite no processing done on the volume other than a correction to a datum of 2000 ft (610 m) and using a single velocity function, structures are imaged in the section. In the shallow section, most reflectors are obscured by the residual noise (yellow box). Reflectors in the middle are relatively continuous through the section. Migration smiles can be seen in the deep sections.
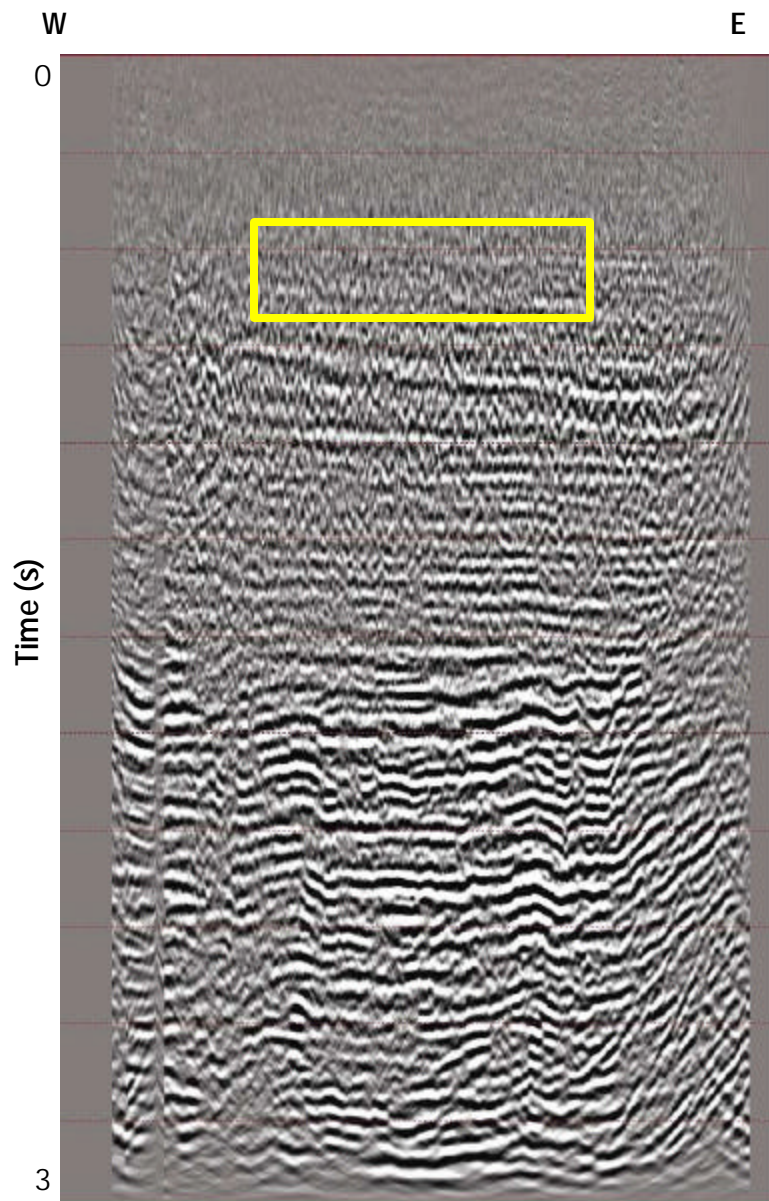
Figure 4.23 – Brute migration of the Vacuum-Maljamar data. The volume is used as a baseline standard for comparing all subsequent migrated volumes. No processing was done on this volume other than the datum correction to 2000 ft (610 m) above sea level. Refer to Appendix A.1 for details on the processing flow.

Figure 4.24 is a section from the brute migration with ground roll filtered out. All parameters and steps are exactly the same as to the true brute migration except that for this volume, ground roll is filtered out. Several differences can be noted between the two migration volumes. In the shallow section, the noise tails are not as pronounced

compared to the brute migration (yellow box). Some of the reflectors that were obscured

by the noise are more visible in the filtered volume. The reflectors are more continuous in

the middle of the section (red arrows) compared to the true brute.
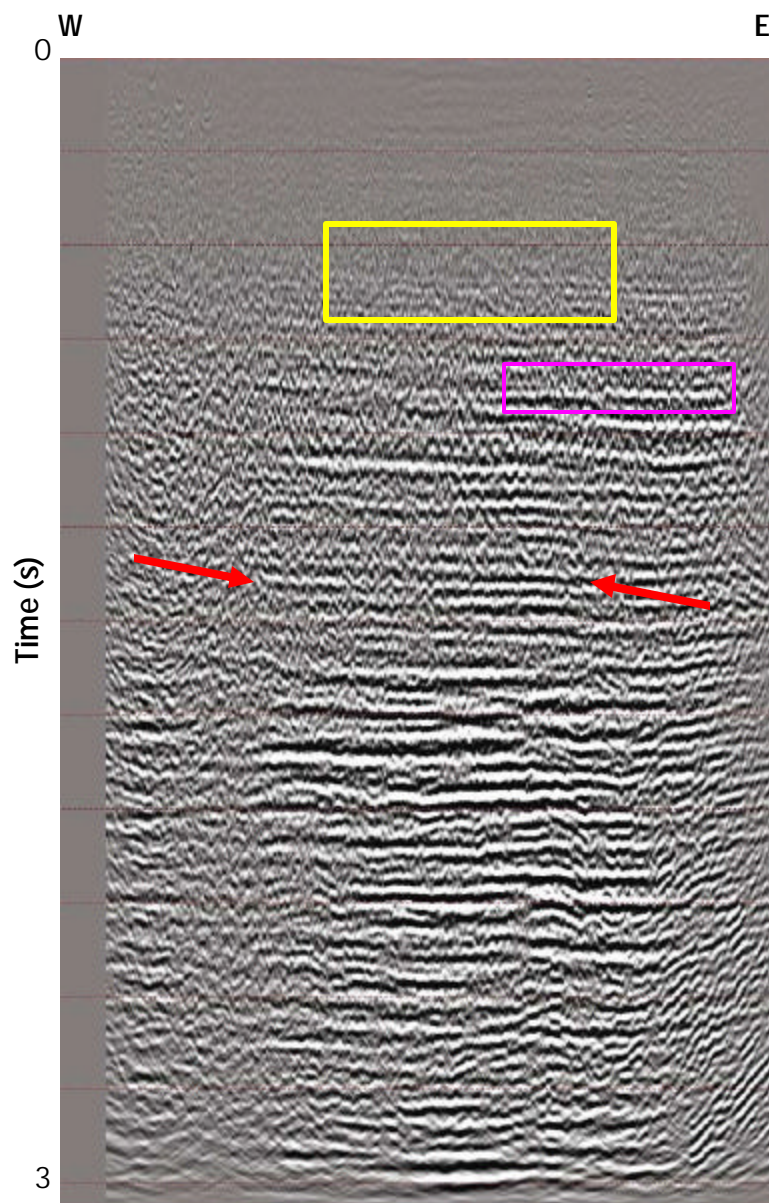
Figure 4.24 – Brute migration with ground roll filtered out. Compared with the brute migration, the shallow horizons show more continuity in the ground roll filtered migration. See Appendix A.2 for full details of the complete processing flow.

Figure 4.25 is a migration from a mid-process quality control point. For this migration, I performed the following processing steps:

- Ground roll filtering;

- Shot-consistent deconvolution; and

- Inside and outside mute.

I use the same single velocity function as the previous two brute migrations. The deconvolution restored some of the frequency content that was lost during the filtering of ground roll. This is most evident for the reflectors in the middle of the section (fuchsia box). Despite the efficiency of using the single velocity function for migration, some of the structures do not appear in their correct position. I point out the eastern edge (red arrow) of the section where two reflectors are crossing each other. This is remedied by using velocities picked across the whole survey. The subsequent volumes show the fact that the single velocity function utilized is not far off from the correct velocity values.
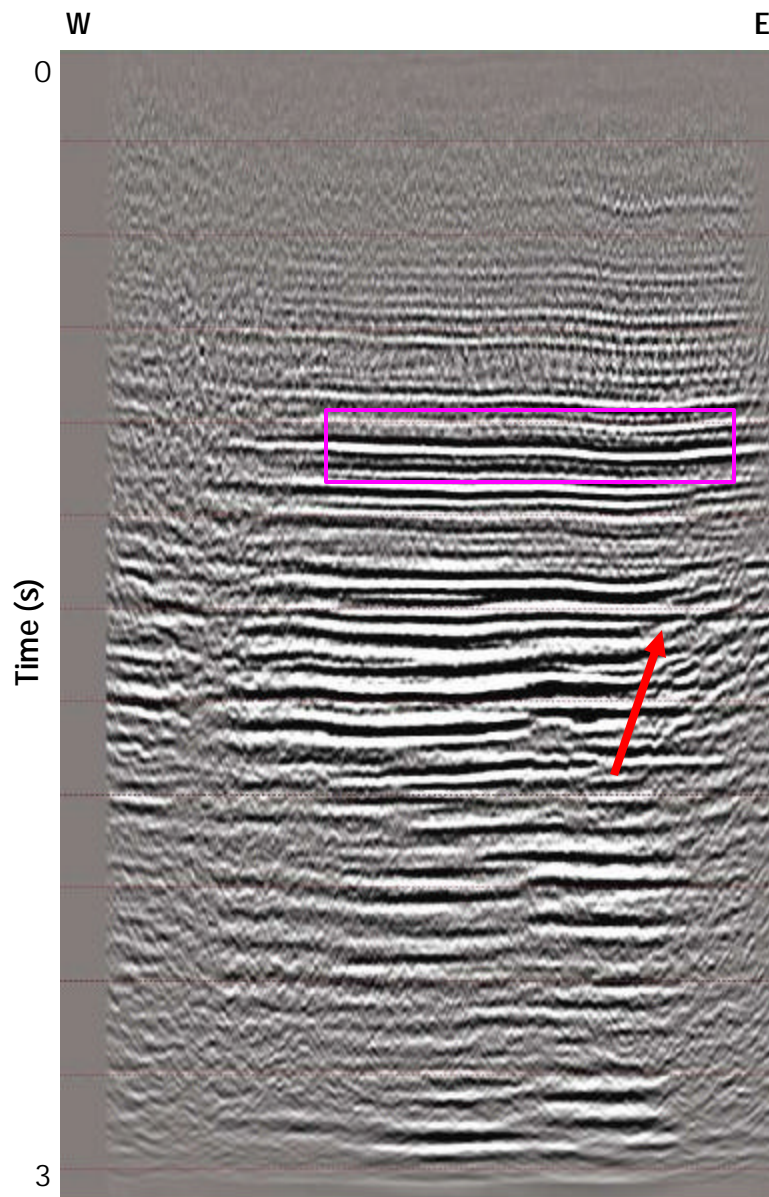
Figure 4.25 – Mid-process migration with migration and the first iteration of velocity analysis. See text for full description of the section and Appendix A.4 for full processing details.

Figures 4.26 and 4.27 are migrations from a full processing sequence, with 4.26 being *without* ground roll filtering and 4.27 is *with* ground roll filtering. All parameters used are the same for both volumes. The marked difference between the two volumes is in the imaging of the shallow reflectors. The unfiltered volume (Figure 4.26) has residual

57

noise leaking into the stack and masks the shallow section of the volume (yellow box). Comparing this to the filtered volume in Figure 4.27, there is still residual noise leaking into the stack but not as obtrusive as in the unfiltered volume.
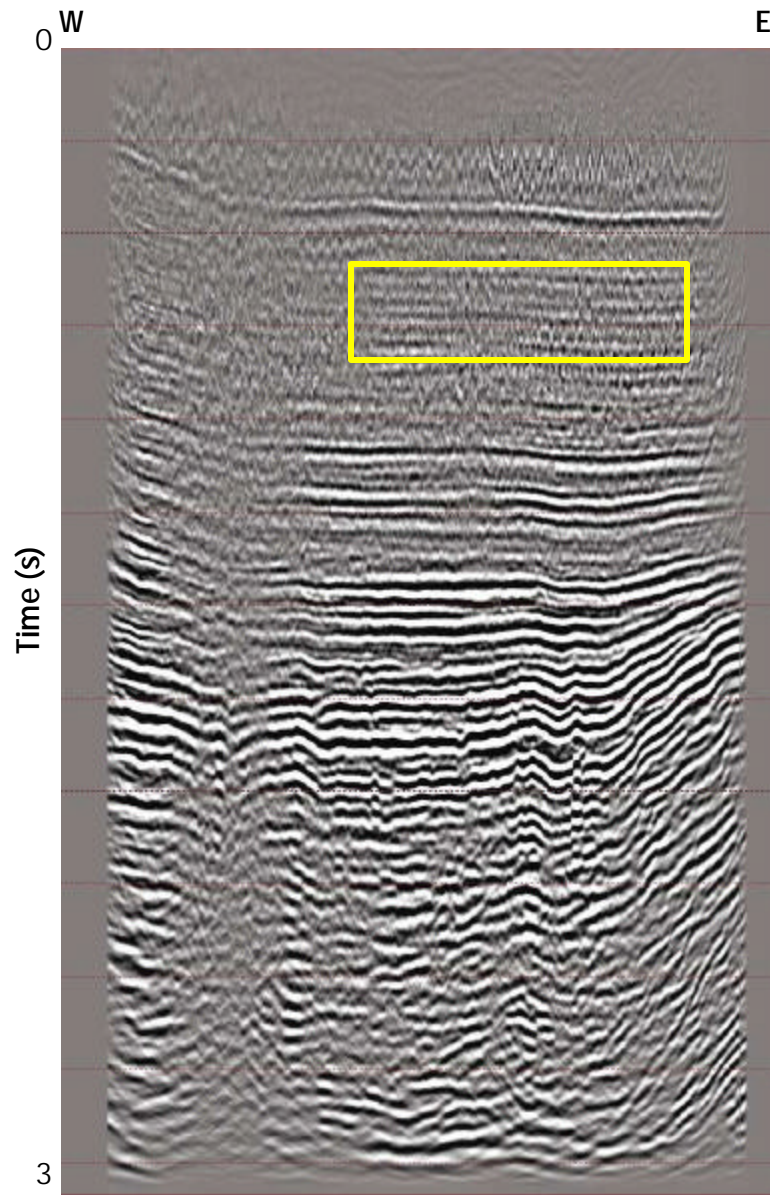
Figure 4.26 – Final migration *without* surface wave filtering. This volume was migrated using the best velocity from the 50 x 50 grid. See Appendix A.6 for full processing workflow.
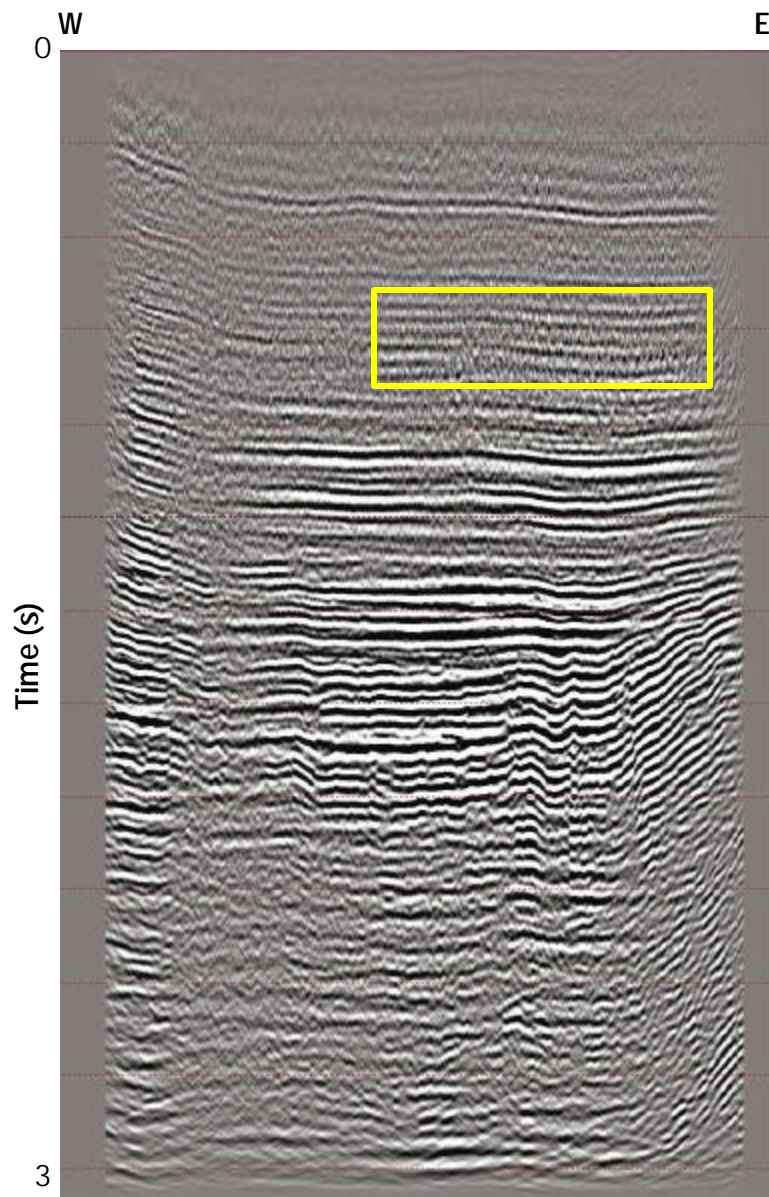
Figure 4.27 – Final migration *with* ground roll filtering. See Appendix A.7 for full the processing workflow.

4.8   Frequency Balancing

As a final comparative step, I applied a spectrum balancing process in order to increase the frequency content of the data. For this process, I used the FOCUS module SPEQ. SPEQ is a spectrum balancing module that performs a time-variant, zero-phase spectral balancing of seismic traces. The seismic input is divided into a series of gain

functions by computing the envelope of the band-pass filtered traces and apply the inverses of the gain functions to each frequency band and then summed (Yilmaz, 1987). This process is shown in Figure 4.26
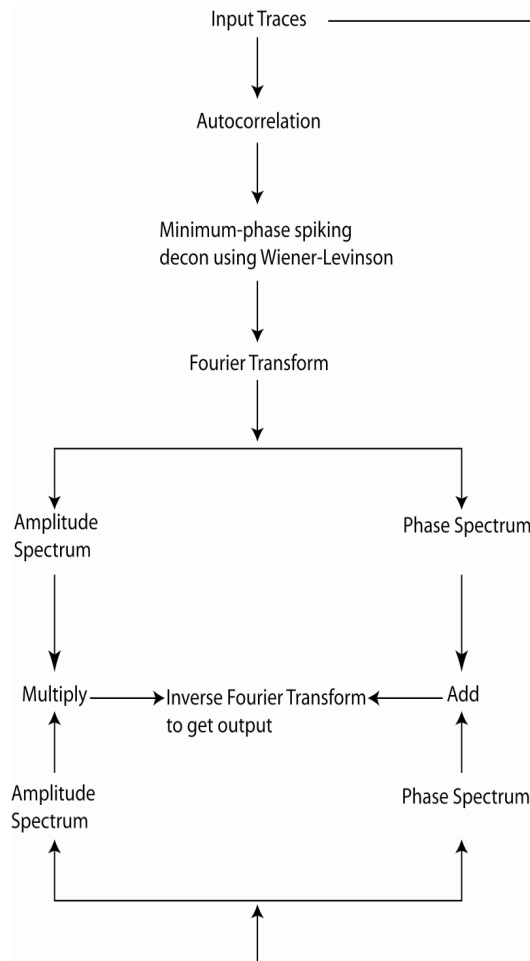
Figure 4.28 – Flowchart for frequency-domain for time-variant spectral whitening (Yilmaz, 1987).

Figure 4.29 is a comparison between migrated sections (a) *without* and (b) *with* and the spectrally-balanced migrated section. The balanced section (Figure 4.29b) shows a higher frequency content for the data than the original section. The shallow reflector (yellow box) has an overall better definition. The reflector in the red box shows better continuity in the balanced section. Comparing the two volumes, the residual coherent

noise in the unbalanced section (white box) has been greatly reduced in the balanced section.
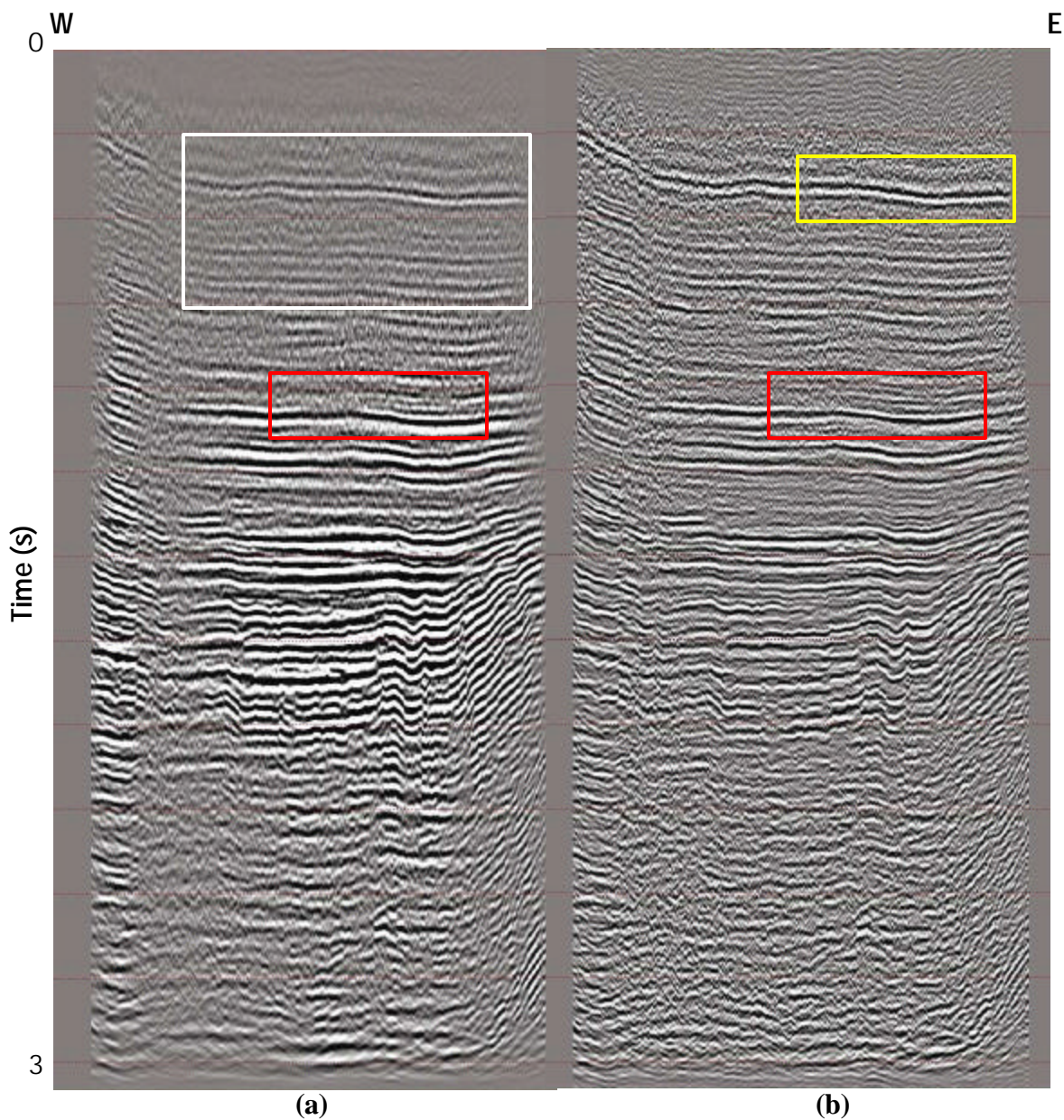
Figure 4.29 – Comparison between the (a) final stack, migrated data with (b) final stack, migrated data with spectral balancing. The shallow reflectors are better defined in the whitened section compared to the unbalanced section.

CHAPTER 5

COMPARISON OF GEOMETRIC ATTRIBUTES

In this section, I compare the sensitivity of geometric attributes generated from the migrated volumes of the different processing flows. An observed drawback of the multi-trace semblance- and variance-based estimates of coherence is that they are sensitive not only to waveform but also to lateral changes in seismic amplitude. My observations are shown through key time slices and compare the lateral resolution of structures and stratigraphic features through coherence, coherent energy gradient, and curvature volumes.

5.1   Coherence Volumes

Coherence is a powerful tool in imaging discontinuities and faults along a surface in time and horizon slices. I compare time slice images from the coherence cubes generated from the different seismic processing flows. White areas correspond to high coherence and black to low coherence.

Figure 5.1 is a comparison of coherence time slices at time t=1.2s from the brute migration (5.1a) and the brute migration with ground roll suppression (5.1b). The brute migration coherence is used as a baseline comparison for all following attribute volumes. In Figure 5.1a, the only visible feature is the NW-SE-trending fault-like feature (red arrow). In Figure 5.1b, acquisition footprint is enhanced compared to Figure 5.1a (yellow rectangle). This is expected as coherence is fairly sensitive to aliased noise that

leaks into the stacked section. Despite the prevalence of acquisition footprint, homogeneity is starting to appear in the northeast section of the survey in Figure 5.1b compared to 5.1a (teal pentagon). The NW-SE trending fault in the western side of the survey is better defined as the more coherent areas give a better contrast to identify the fault.
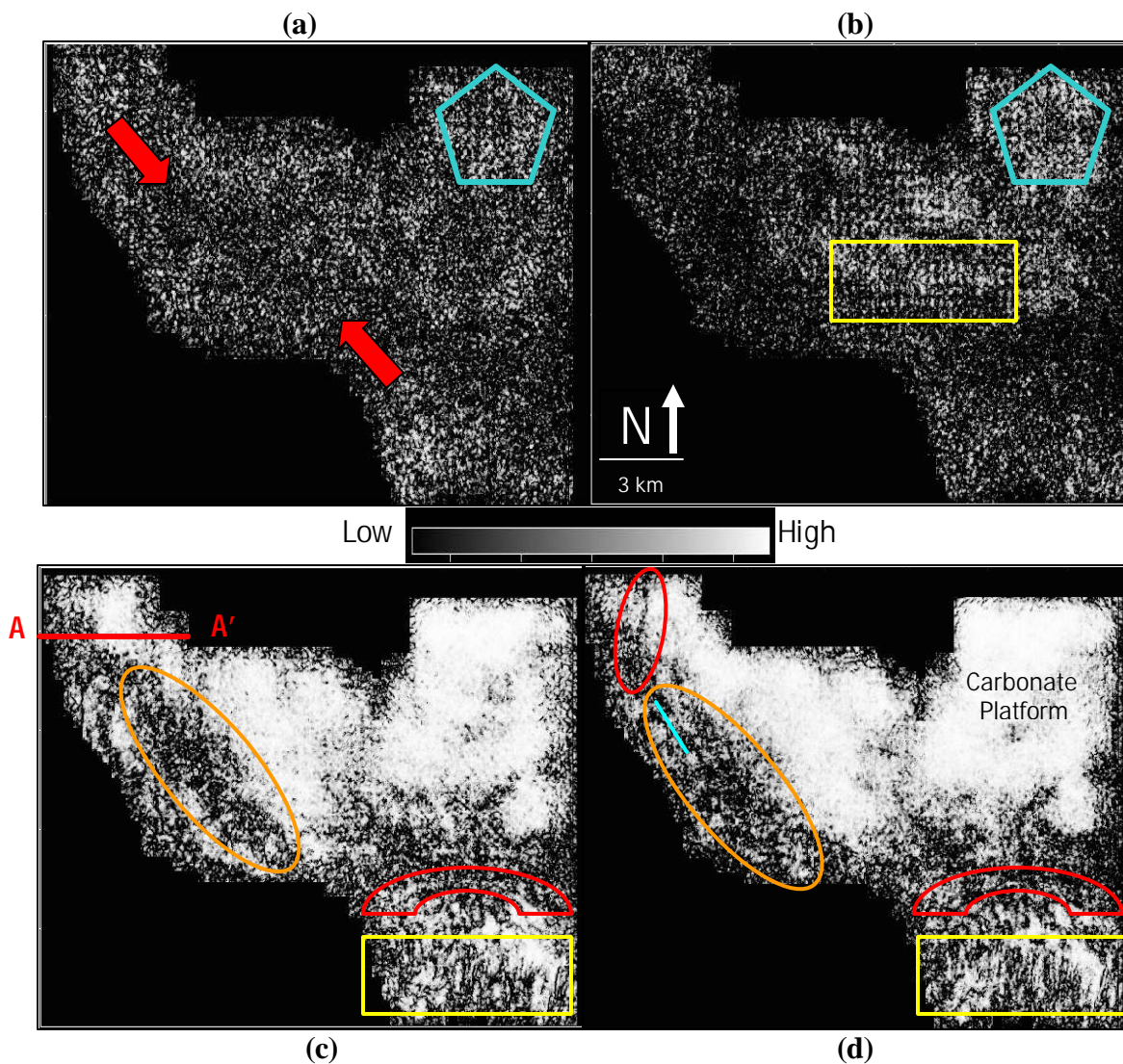
Figure 5.1 – Time slice taken from the coherence volume at time t=1.2s. (a) Coherence from brute migration; (b) from brute migration *with* ground roll filtering; (c) from full processing flow with no ground roll filtering; (d) full processing *with* ground roll filtering. See text for full description.

Figure 5.1c and d are time slices through coherence volumes from the full conventional processing flows. Figure 5.1c has no ground roll filtering while Figure 5.1d has ground roll filtering. Expectedly, subsurface features image much better in the full processing flow than in the brute processing flows. The northeast side shows greater coherence on both time sections. Acquisition footprint is still visible on the time slices. The northwest-trending feature identified in Figure 5.1a is now better defined in the full processing volumes (gold oval). In the ground roll-filtered volume, I identify segments of the fault (teal line) that are better defined than in the unfiltered volume. On the Northwest corner of the survey in Figure 5.1d, I identify a channel feature (red oval) that is not imaged in Figure 5.1a. Even in a full-sequence flow, the fault is also not imaged (Figure 5.1c). This fault is identified in the vertical cross-section (Figure 5.2). I interpret this as a fault and not as a processing artifact since it appears consistently on the vertical seismic section throughout the areal extent that appears on the coherence time slices. Based on time and cross-section views, I interpret this to be a reverse fault.
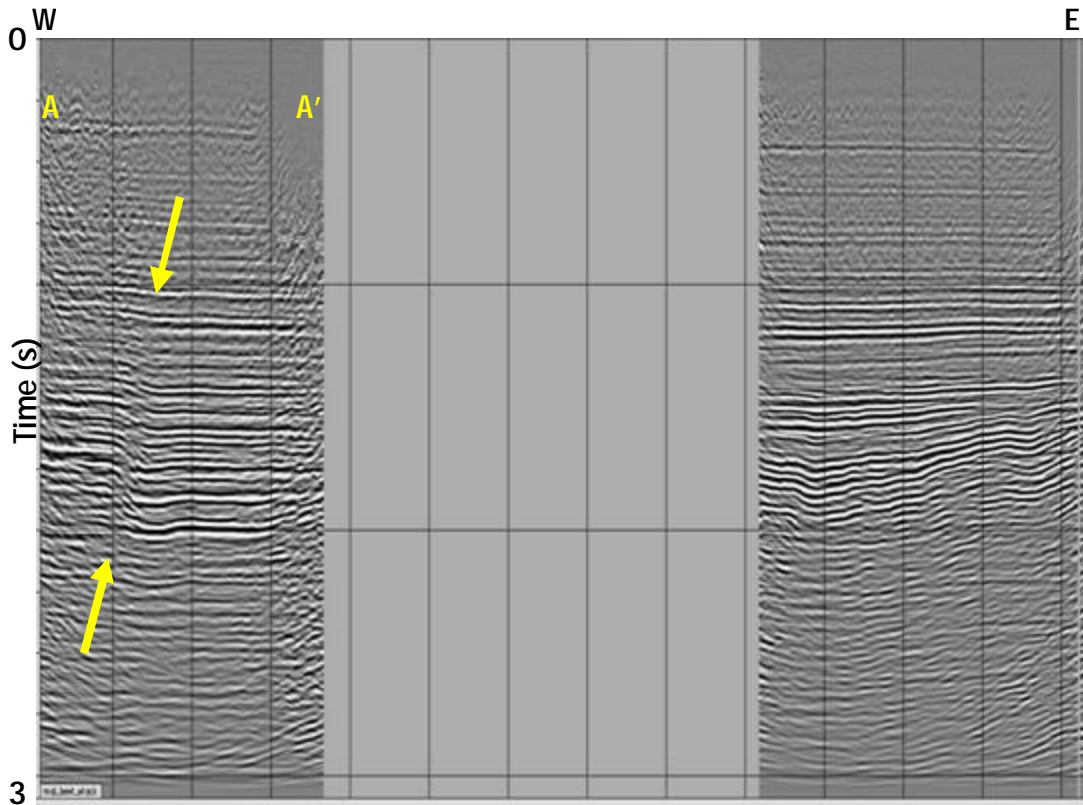
Figure 5.2 – Cross-section view of the Vacuum-Maljamar survey running through A-A'. The fault identified by the red circle in Figure 5.2b is identified by the yellow arrows.

The red arcs identify the demarcation between the platform and the collapse (slump) feature. There is a difference in imaging the southern area of the survey (yellow box). The slump deposits in the southern section of the survey have more character than in the volume without ground roll filtering. The slump features are particularly hard to correlate laterally on the conventional seismic. Removal of the ground roll noise train and its back-scattered components results in the improved lateral resolution of the slump features.

Figure 5.3 are time slices taken at t=1.6s. In Figure 5.3a, I show the brute volumes *without* ground roll filtering and *with* ground roll filtering in 5.3b. The center of the survey (red circle) demonstrates a marked difference in the imaging of the two

volumes. In Figure 5.3a, the center of the survey is very incoherent. Acquisition footprint is also fairly visible in this volume. In Figure 5.3b, the same area is more coherent, while the imprint of the acquisition footprint is diminished. The NW-SE trending fault identified in Figure 5.1 is more visible in this section as well (yellow arrows). On the east side, coherence is also greater. A channel feature is now visible in this area of the survey (purple arrows), as compared with the unfiltered volume where it is completely masked by noise. The southern section of the survey displays better lateral resolution of the slump features.

Figure 5.3c and d are the same time slices at t=1.6s from the full-processing volume *without* (Figure 5.3c) and *with* (Figure 5.3d) ground roll filtering. The ground roll filtered volume to have more coherent areas. In Figure 5.3d, I identify features that have a marked improvement. The fault I identified in Figure 5.2 continues down into this level. The edges of the fault in the filtered volume are better defined (Figure 5.3d) while in the unfiltered volume, there is a break in the continuity of the fault near its southern extent (Figure 5.3c, red box). The NW-SE fault identified is also better resolved, having a sharper definition of its edges (red arrow). I delineate a channel feature trending N-S on the eastern section of the survey of 5.3d (green arrow). This channel is less visible in the unfiltered volume. This channel feature will be better imaged using the coherent energy gradient attribute. The slump features to the south exhibit crisper edges and more definition in the ground roll filtered volume.
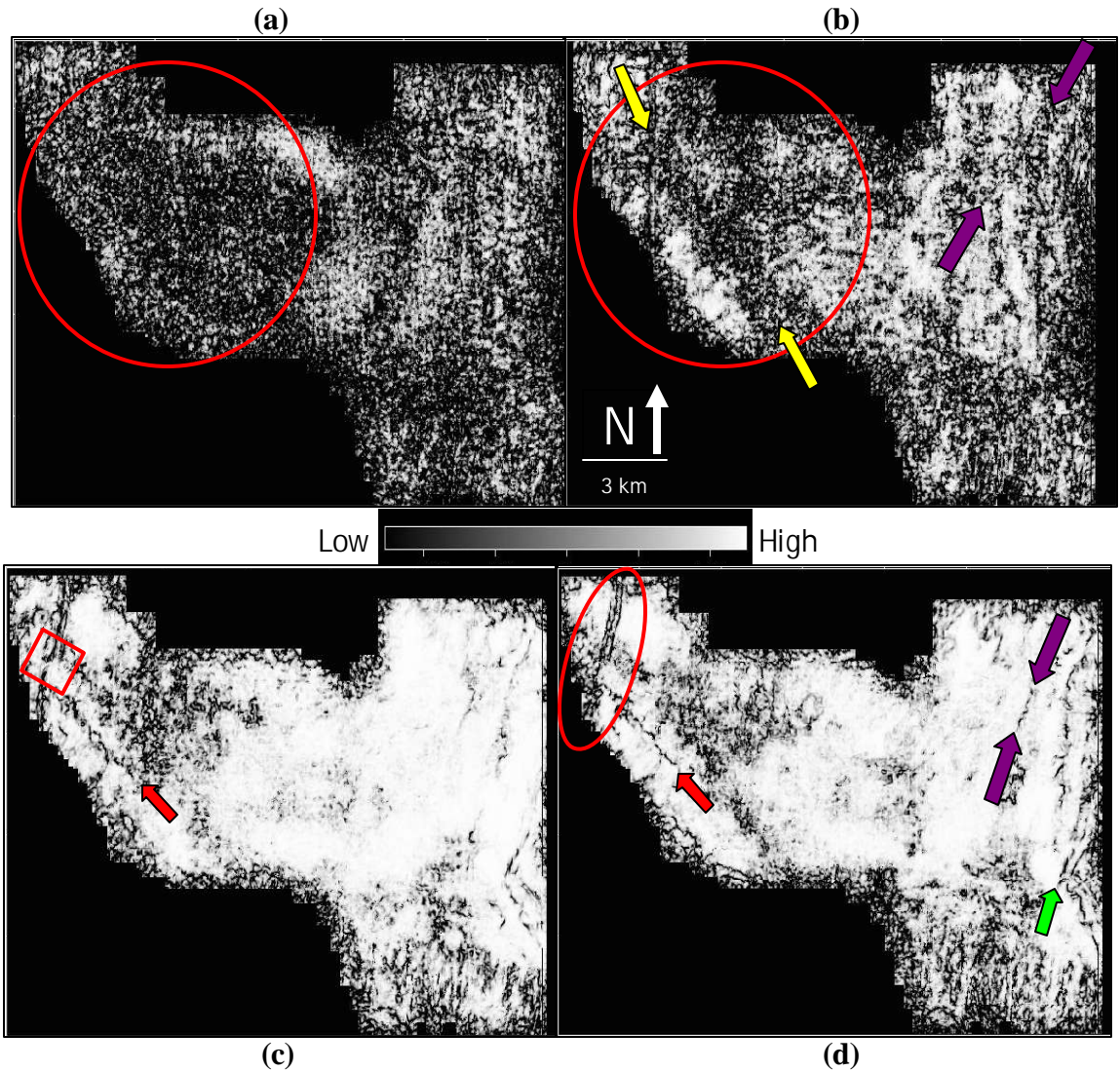
Figure 5.3 – Coherence time slice at t=1.6s. Figure 5.5b is coherence volume *with* ground roll filtering. Channel features (green, purple arrows) are better resolved in 5.5b compared to 5.5a. The fault in the NW corner is continuous in the filtered volume, while it is broken in the unfiltered volume (red box).

5.2   Coherent Energy Gradient Volumes

Like coherence, coherent energy gradients are useful in mapping faults and fractures through the volume. The advantage of coherent energy gradients is that values will be large when there is varying high amplitude coherent energy, and small when the reflectivity is either smoothly varying, low amplitude, or incoherent. In this manner, the

coherent energy gradient images are quite complimentary to coherence images. For purposes of this study, I find them highly effective in delineating thin channels when there are subtle changes in tuning.

In Figure 5.4a, white arrows point to a channel edge that starts to appear in the center of the survey. Despite the limited processing, the margin between the carbonate platform and the Brushy Canyon siliciclastics to the south (fuchsia arrows) can be faintly imaged. The slump to the south has no discernible character (yellow box). I identify a feature in the NW corner of the survey (green box) to be a processing artifact. The feature is too linear to be anything of natural origin.

A few points of difference in the ground roll filtered volume (Figure 5.4b) are observed from the previous volume. The filtered volume shows enhancement of the acquisition footprint, especially in the center of the survey. I ascribe this to residual coherent noise that leaks into the stacked volume as the algorithm seeks out the coherent segments of the data. The slump deposits to the south (yellow box) exhibits better seismic character as I can see channel features have better lateral resolution. The artifact identified in 5.4a is no longer imaged.
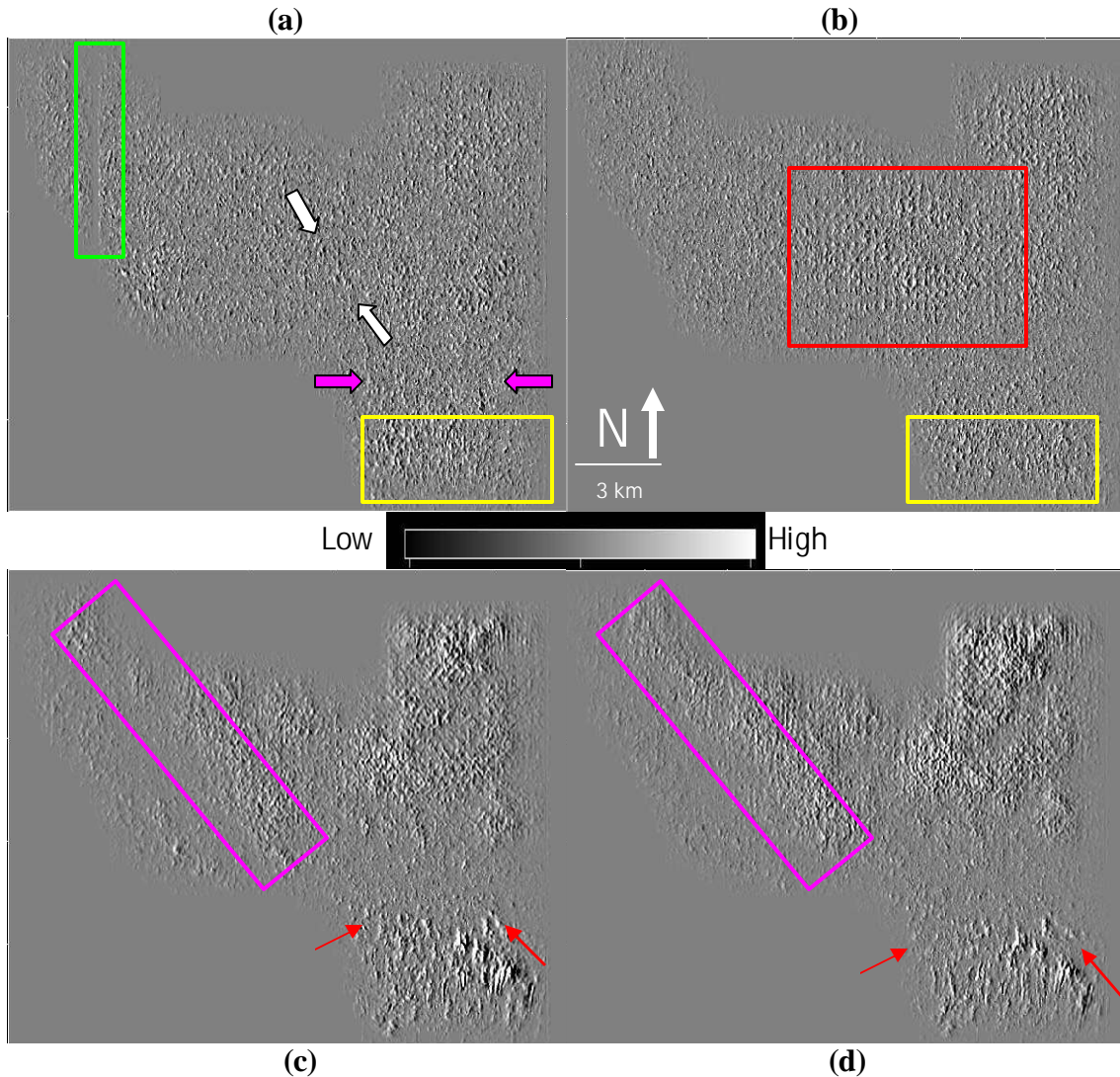
Figure 5.4 – East-west component of the coherent energy gradient from t=1.2s. (a) From the brute volume *without* ground roll filtering; (b) brute volume *with* ground roll filtering; (c) from full processing volume *without* ground roll filtering; (d) *with* ground roll filtering. See text for full description.

Figure 5.4c and d are the same time slice at t=1.2s from full processing volumes

(c) *without* and (d) *with* ground roll filtering. Acquisition footprint is still fairly prevalent

in both volumes, although more structures can be seen despite this. In both volumes, I

identify the edge of the platform margin (red arrows). This corresponds to the

demarcation seen in the coherence volume of areas of high coherence of the platform and

the low coherence in the slump features. The slump features to the south are better resolved in the filtered volume, with the edges of the channel features. Individual channels could be identified in this volume. To the north, the ridges have a greater areal extent in the filtered volume. In the fuchsia box, the NW-trending ridge has better detail in the filtered volume.
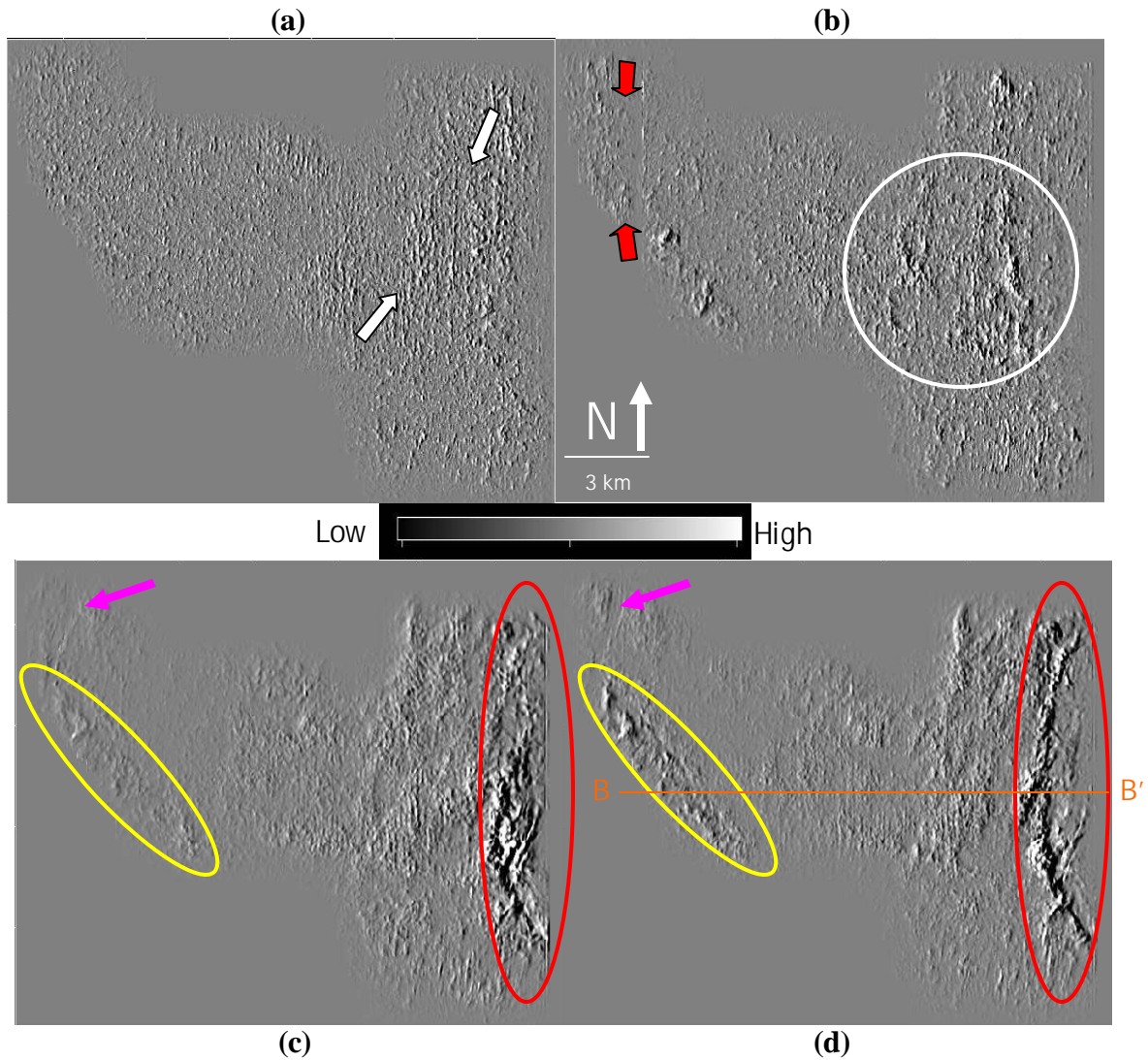
Figure 5.5 – East-west component of the coherent energy gradient from t=1.6s. (a) Brute section *without* ground roll filtering; (b) *with* ground roll filtering; (c) full processing sequence *without* ground roll filtering and; (d) *with* ground roll filtering. See text for full description.

Figure 5.5 are time slices of the east-west component of the coherent energy gradient at t=1.6s. In 5.5a, the brute volume does not show many features. In the east side of the survey (white arrows), a channel feature starts to be visible. I do not quantify this as a processing artifact since it does not follow a north-south trend as is common when the east-west component of the coherent energy gradient is used. The red arrows in 5.5b point out a feature I interpret as a processing artifact as it follows a linear N-S trend to be a natural feature. On a visual comparison alone, Figure 5.5b has more surface relief than 5.5a. Most features included in the white circle are later identified to be channel edges.

Figure 5.5c and 5.5d are from the full processing flow. These two figures show the most dramatic difference in imaging of the geometric attributes. On the southwest section of the survey, there is a difference in the relief of the ridge trending NW-SE (yellow oval). To the east of the survey, I see a major difference in the imaging of the channel running N-S. In 5.5c, the channel is imaged well in the sense that the edges of it are clearly defined and the areal extents of it can be delineated. It is only towards the northern end of the channel that it loses definition. In the filtered volume of Figure 5.5d, the imaging of the channel is improved, with the northern end of the channel having better resolution. The edges of the channel in the filtered volume are crisper than in the unfiltered volume. The fault identified in Figure 5.1 (red arrow) appears grayed out. Since the coherence identified this as an area of low coherence, it appears as a zero in the coherent energy gradient as shown by the color bar. Despite all the improvements in the imaging, there is still a small imprint of acquisition footprint.

As another point of comparison, I also evaluate any differences in the resolution of features as it goes through a smoothing process. I show this comparison in Figure 5.7, where I again show the time slice at t=1.6s from the final processing flow with ground roll filtering. Figure 5.7a is the volume with no smoothing done and 5.7b is the volume that has undergone 2-pass smoothing. Overall, aside from miniscule enhancements, I do not see a major difference in the resolution of both volumes and it can be argued that there is even no difference in the two volumes.
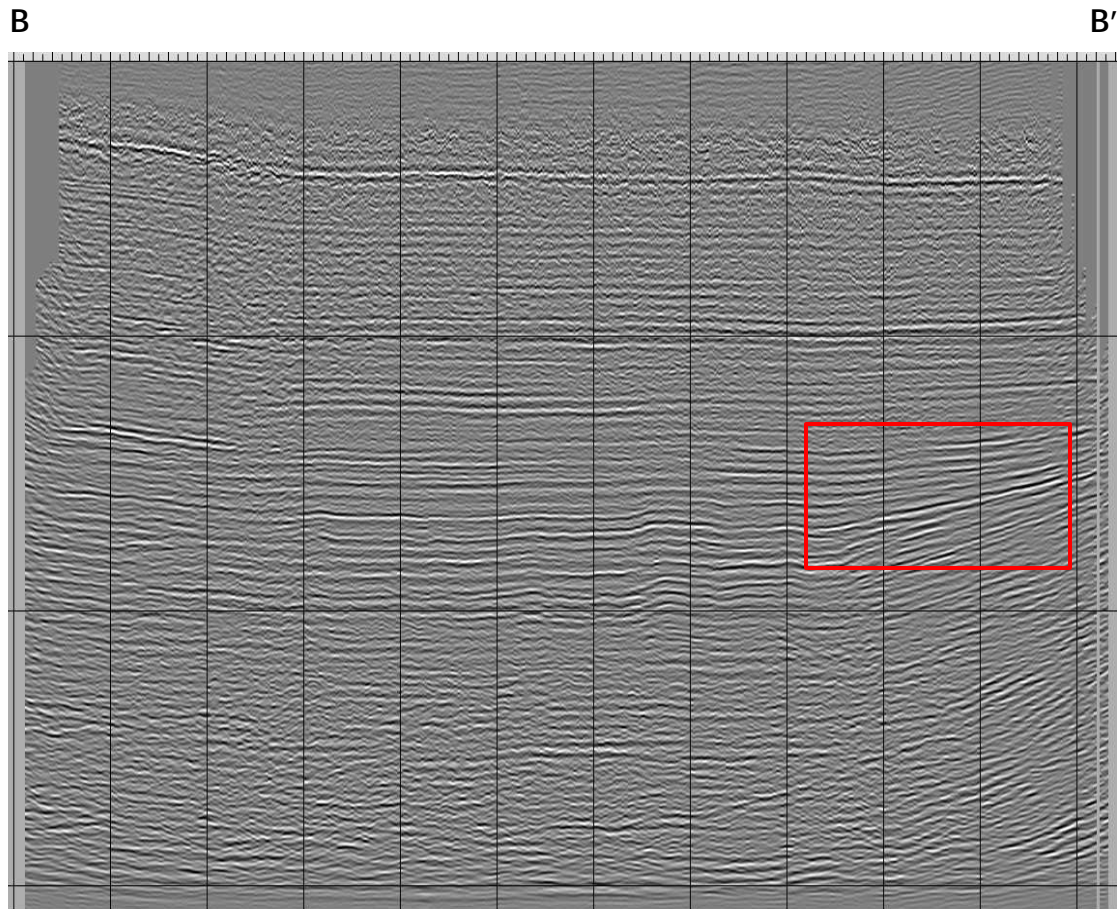
Figure 5.6 – Vertical section along B-B'. Red box highlights the channel system imaged in Figure 5.5 c and d.
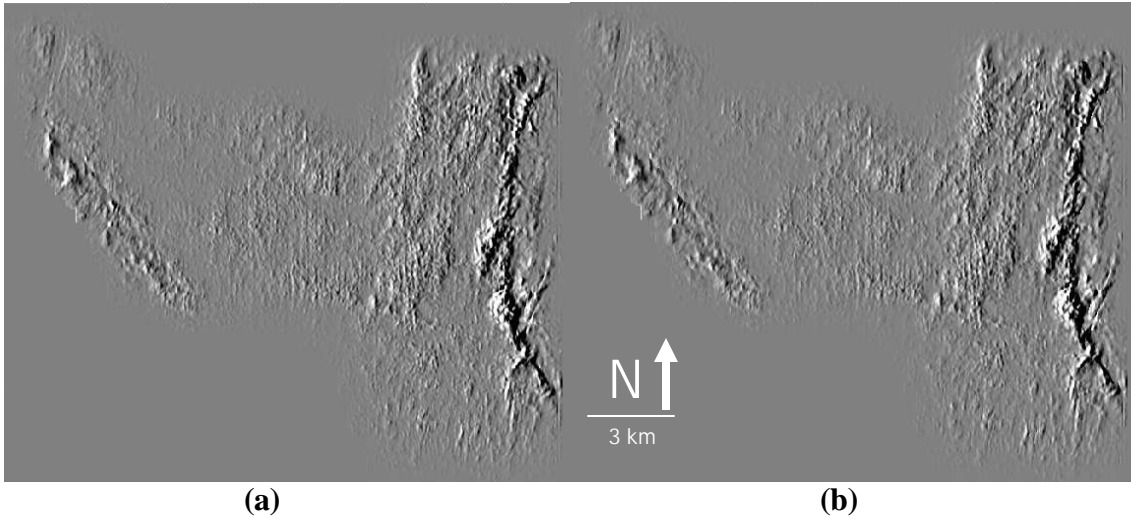
Figure 5.7 – Time slice at t=1.6s from the full processing flow with ground roll filtering. (a) No smoothing; (b) 2-pass smoothing. See text for complete discussion of comparison.

5.3 Most Negative Curvature Volumes

I find that most negative and most positive curvatures to be efficient in delineating faults, folds, fractures, and flexures. These curvatures represent the maximum curvature at any point on the plane. Most negative curvature images synforms and bowl-like features effectively.

Figure 5.8 are curvature time slices taken at t=1.2s. Figure 5.8a displays the brute processing time section. As expected, I do not see any features in the section. The (red box) processing artifact identified from Figure 5.4a again manifests itself in the section. Figure 5.8b is the brute volume with ground roll filtering. What is imaged is consistent with what I have observed so far. In the ground roll-filtered brute volume, acquisition footprint is enhanced (white box). The ground roll filtered volume has a slightly higher coherence than in the unfiltered volume. This is visible despite the enhancement of acquisition footprint. Not much else can be imaged in both volumes.
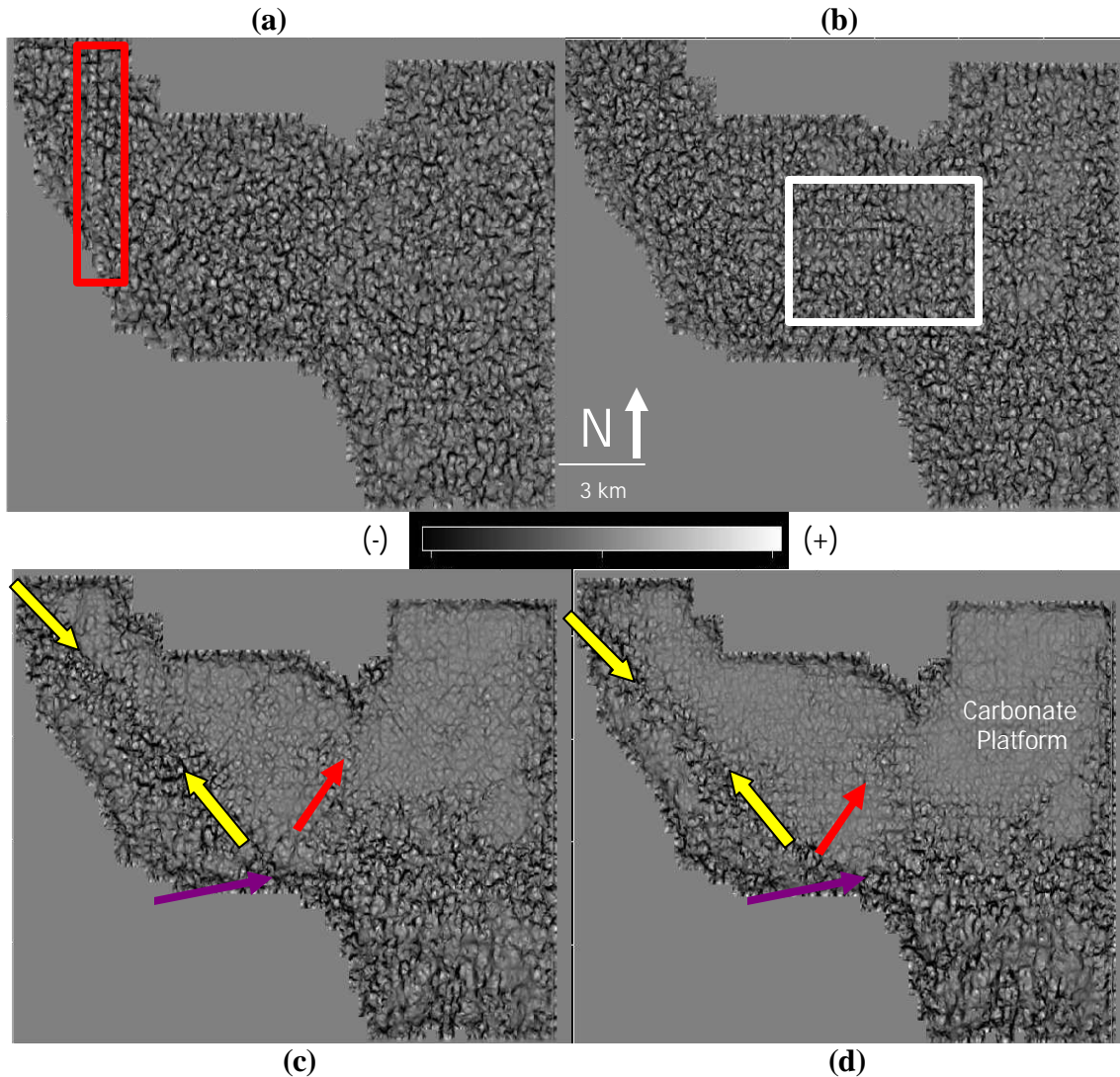
Figure 5.8 – Most negative curvature taken at t=1.2s. (a) Brute volume *without* ground roll filtering; (b) brute volume *with* ground roll filtering; (c) full processing *without* ground roll filtering; (d) full processing *with* ground roll filtering.

Figure 5.8 c and d are time sections at t=1.6s from the full processing volumes. I

now see some features that can be correlated to the other attribute volumes. The NW-SE

running platform edge is fully imaged in both volumes (yellow arrows). In the ground

roll filtered volume, the fault is imaged with the edges better resolved. The carbonate

platform to the NE of the survey has a curvature of approximately zero. This can be

correlated to what was interpreted on the coherence section (Figure 5.1) as having the

highest coherence. The area had very few incoherent areas and is confirmed in both the coherent energy gradient and curvature volumes. In the middle of the survey, a channel feature is slightly imaged (red arrow). This feature has a slightly wider lateral extent in the ground roll filtered volume. The margin between the platform and the slump deposits (purple arrow) is imaged in both volumes. The many faults and channels that run along the slump deposits are resolved better, giving them a higher negative value.

Figure 5.9 are time slices at t=1.6s. Figure 5.9a is the brute volume. The tip line of the NW-SE fault (red arrow) is still imaged down to this level. The unfiltered volume (Figure 5.9a) shows little coherence compared to the filtered volume, especially in the middle of the survey. I identify a channel feature to the south of the survey (white arrow) in the unfiltered volume. Channels to the east of the survey start to be imaged in the Figure 5.9b (purple oval). These are not imaged in the unfiltered volume.
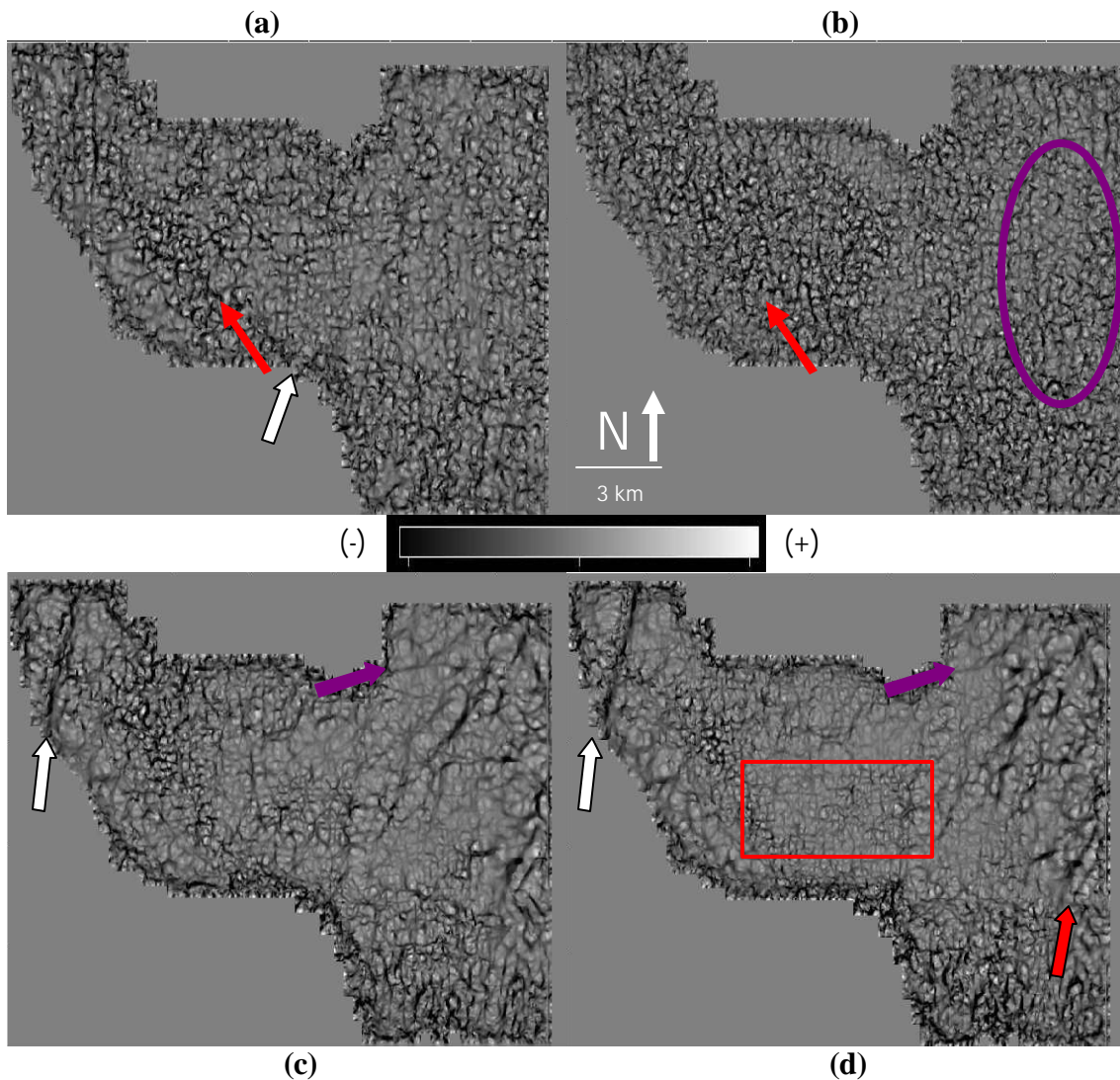
Figure 5.9 – Most negative curvature from time t=1.6s. (a) Brute processing *without* ground roll filtering; (b) brute processing *with* ground roll filtering; (c) full processing *without* ground roll filtering; (d) *with* ground roll filtering. See text for full description.

Figure 5.9 c and d are taken from the fully processed volume. The fault in the NW corner of the survey is imaged by both volumes (white arrow). This fault does not appear in the brute volumes. There is a difference in the imaging of the edges of the fault. The edges are crisper in the filtered volume. The removal of ground roll gives the fault a higher absolute negative value in the filtered volume than in the unfiltered one. The center of the survey has significantly less distortion in the filtered volume (red box).

The large channel imaged in Figure 5.6d is identified in the eastern section of the survey (red arrow). The morphology imaged in the coherent energy volume is in agreement with what is imaged in the curvature volume.

5.4   Most Positive Curvature Volumes

Most positive curvature is effective in imaging features such as antiforms, domes, and saddle-type forms.

Figure 5.10 is a time slice taken at t=1.2s through the most positive curvature volumes corresponding to the four processing flows. The artifact that appears consistently in all attribute volumes shows up here as well (Figure 5.10a, green box). The only feature I can delineate in figure 5.10a is the margin between the Carbonate Platform and the Brushy Canyon deposits (red arrow). This is also slightly imaged in the Figure 5.10b (red arrow). In the filtered volume (Figure 5.10b), I can see the imprint of acquisition footprint through the center of the survey. Overall, not much is imaged in the brute curvature volumes.

In 5.10c and 5.10d, I display the time slices from the fully processed volumes. The fault on the NW corner of the survey (white oval) is imaged slightly but is not even imaged in the unfiltered volume. The major fault trending NW-SE (red arrow) has better preserved edges in the filtered volume. The east side of the survey remains consistent with what was imaged in the other volumes as there are no features of note running across the carbonate platform. The slump features to the (yellow box) south show minor differences in imaging. Some of the channels to the south have an overly linear trend,

giving it an over-processed look. A channel in the middle of the survey (white arrows) is

imaged well in the unfiltered volume, though just slightly visible in the filtered section.

(a) **(b)**

N 3 km

(-) (+)

Carbonate Platform

(c) **(d)**
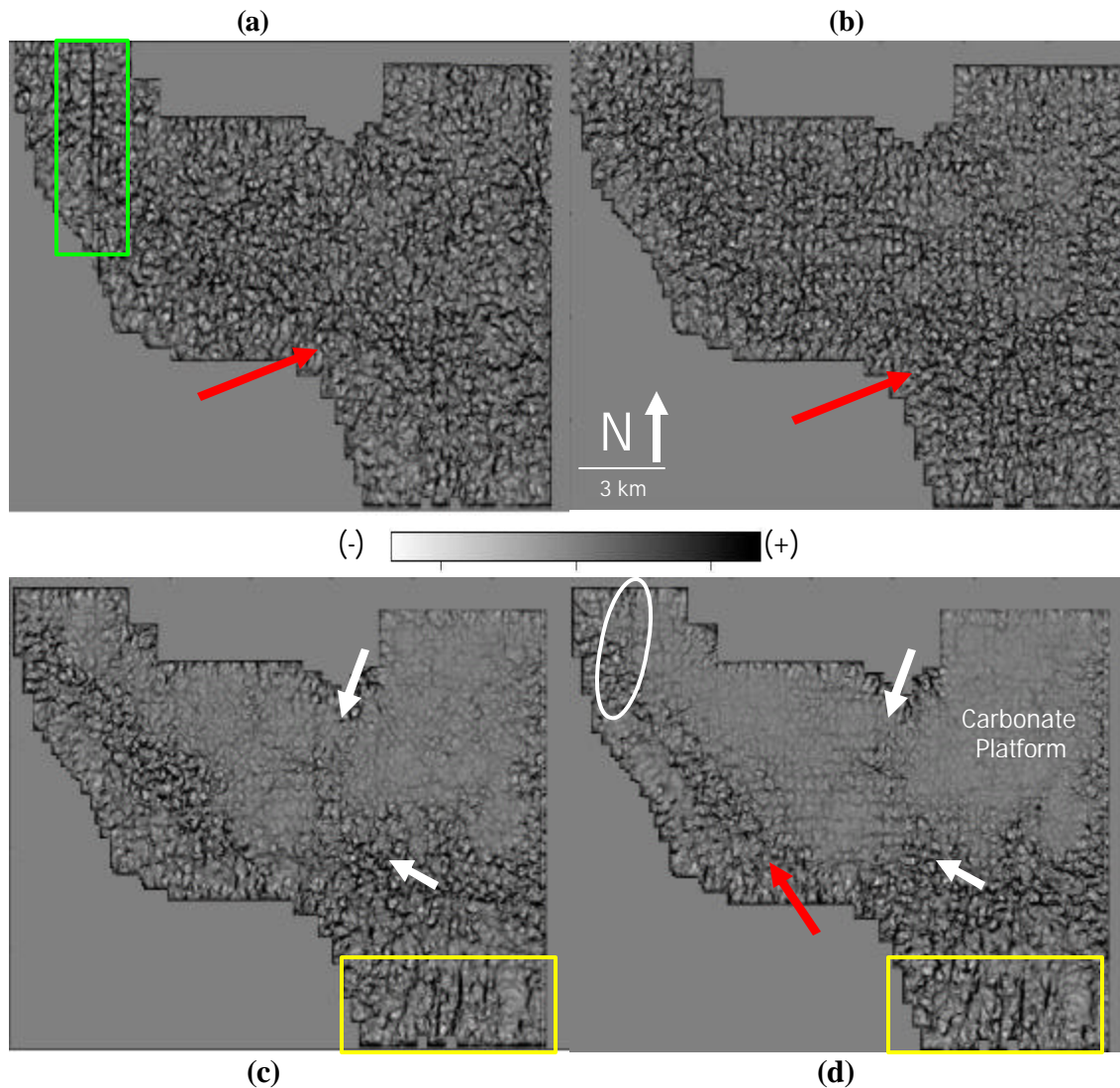
Figure 5.10 – Most positive curvature time slices taken at t=1.2s. (a) Brute processing; (b) brute processing *with* ground roll filtering; (c) full, conventional processing *without* ground roll filtering; (d) *with* ground roll filtering.

I display a time slice at t=1.6s in Figure 5.11. In the brute volume, the edges of

the channel imaged in Figure 5.5d can be seen (white box).

(a) **(b)**

(c) **(d)**
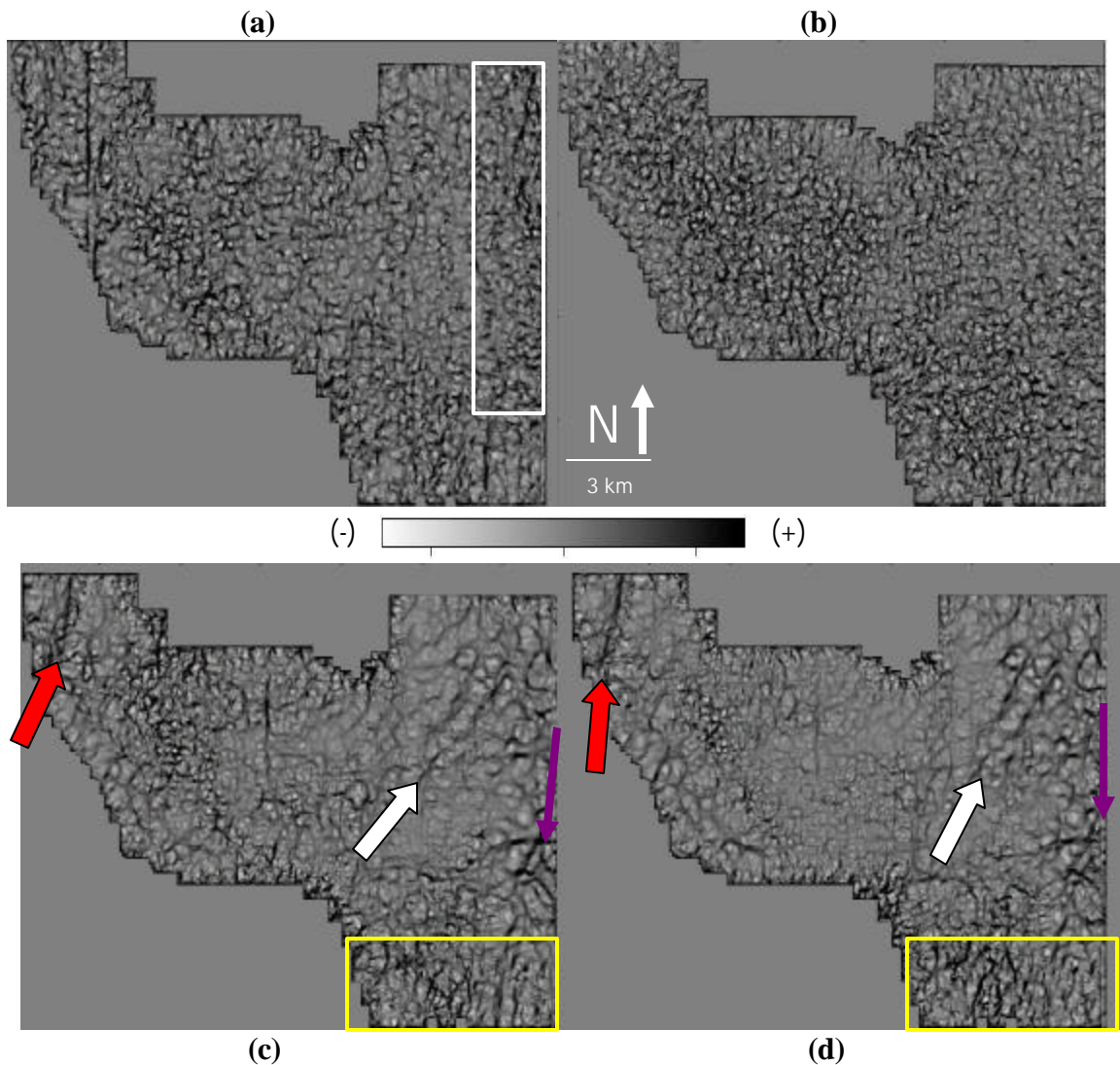
Figure 5.11 – Most positive curvature time slice taken from t=1.6s. (a) Brute processing; (b) brute processing *with* ground roll filtering; (c) full, conventional processing *without* ground roll filtering; (d) *with* ground roll filtering.

Figure 5.11 c and d are from the full processing volumes. The fault on the NW corner of the survey is imaged well on both volumes, with the filtered volume (Figure 5.11b) showing better edge preservation, i.e. higher curvature values at the fault edges. The channel edges in the eastern section of the survey are also crisper than in the

unfiltered volume (white arrows). The edges of the large channel imaged in Figure 5.5d is delineated in both volumes with fairly similar results (purple arrows).

In Figure 5.12, I display side-by-side time slice t=1.6s from the (a) most negative curvature and (b) most positive curvature volumes. This is to show that the attribute volumes do image the same features but they highlight different sections of the same feature. The yellow arrows on both sections point to the same fault in the time section but image different sections of it. In the most negative curvature slice (Figure 5.12a) the fault extends across the whole extent of the NW corner of the survey. In Figure 5.12b (most positive curvature), the fault dies towards its southern extent. The center of the fault has the highest negative curvature value imaged while its edges have a curvature value of approximately zero. The color bar confirms the curvature values exhibited by the fault.

(a)   **(b)**
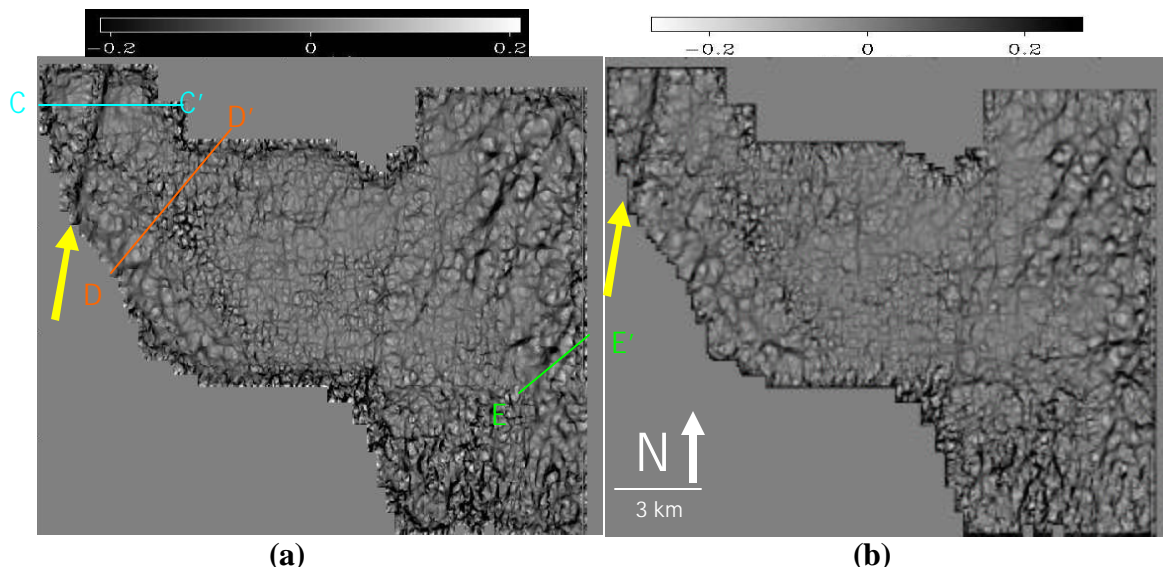
Figure 5.11 – Side-by-side comparison of most negative (a) and most positive (b) curvature at time t=1.6s. The algorithm highlights different segments of the imaged fault (yellow arrows), showing that the algorithms are independent of each other.

Figure 5.12 are cross-sections taken across the Maljamar survey, as identified in Figure 5.11a. This cross-sections are used as a quality control step to verify the geologic structures imaged in the attribute volumes. Cross-section C-C' is across the fault in the NW section of Maljamar. This fault is pointed out in the section (red arrow). Comparing the fault in the vertical section with the structure imaged in both the most negative and most positive curvature volumes, the sections of the fault corresponds to the localized structure imaged.

Section D-D' is across the platform margin. The platform margin is identified with the purple arrows in Figure 5.12b. In Figure 5.12c, cross-section E-E' crosses two faults running in the SW section of the survey. The two faults are parallel with each other in the time sections and possibly borders a channel system (Figure 5.5d). These faults are imaged better in the most negative curvature volume and its appearance in the vertical section correlates with this.

(a)   **(b)**   **(c)**
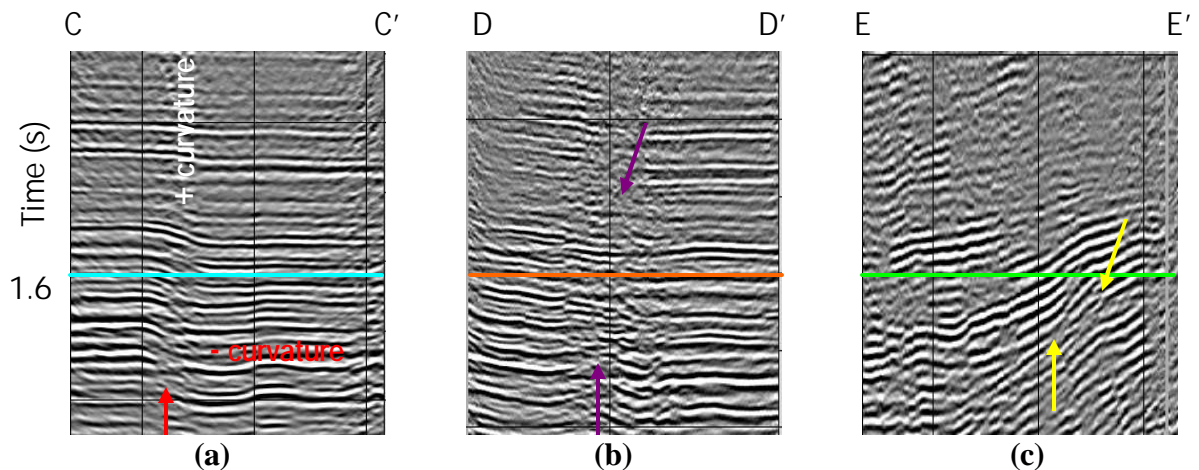
Figure 5.12 – Cross-sections taken across Maljamar survey. (a) Section C-C'; (b) Section D-D'; (c) Section E-E'.

CHAPTER 6

Horizon Extractions from Vacuum-Maljamar Field

In this chapter, I perform horizon slice interpretation of the Maljamar data set that I processed as described in Chapter 4 and combine this with my horizon slice interpretation of the Vacuum Field survey.

Vacuum Field and Maljamar are two separate surveys that overlap, with Maljamar being the more westerly of the two. The Maljamar data that I processed occupies overlaps a third of the more eastern Vacuum Field survey. One quality control that I use to check the validity of my processing is to compare the areas of the two surveys that overlap (Figure 6.1). The blue box outlines the extent of the Vacuum Field survey while the black box outlines the Maljamar survey. Cross-section A-A' is shown in Figure 6.2.
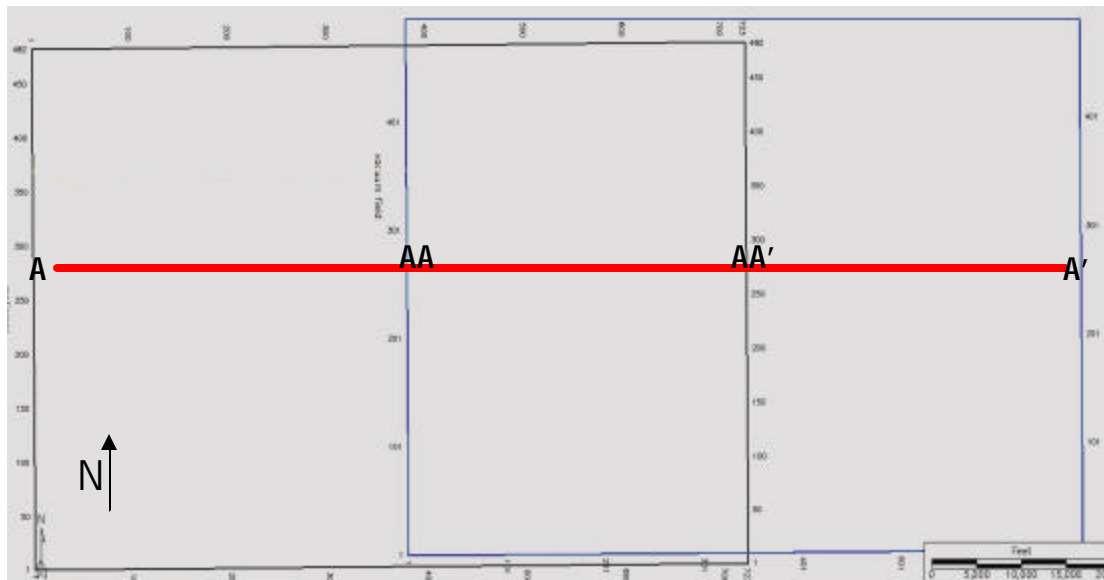
Figure 6.1 – Areal extents of the Maljamar and Vacuum Field surveys. The western survey is the Maljamar (black box) and the eastern survey is Vacuum Field (blue box). AA-AA' is the section of the two surveys that overlap.
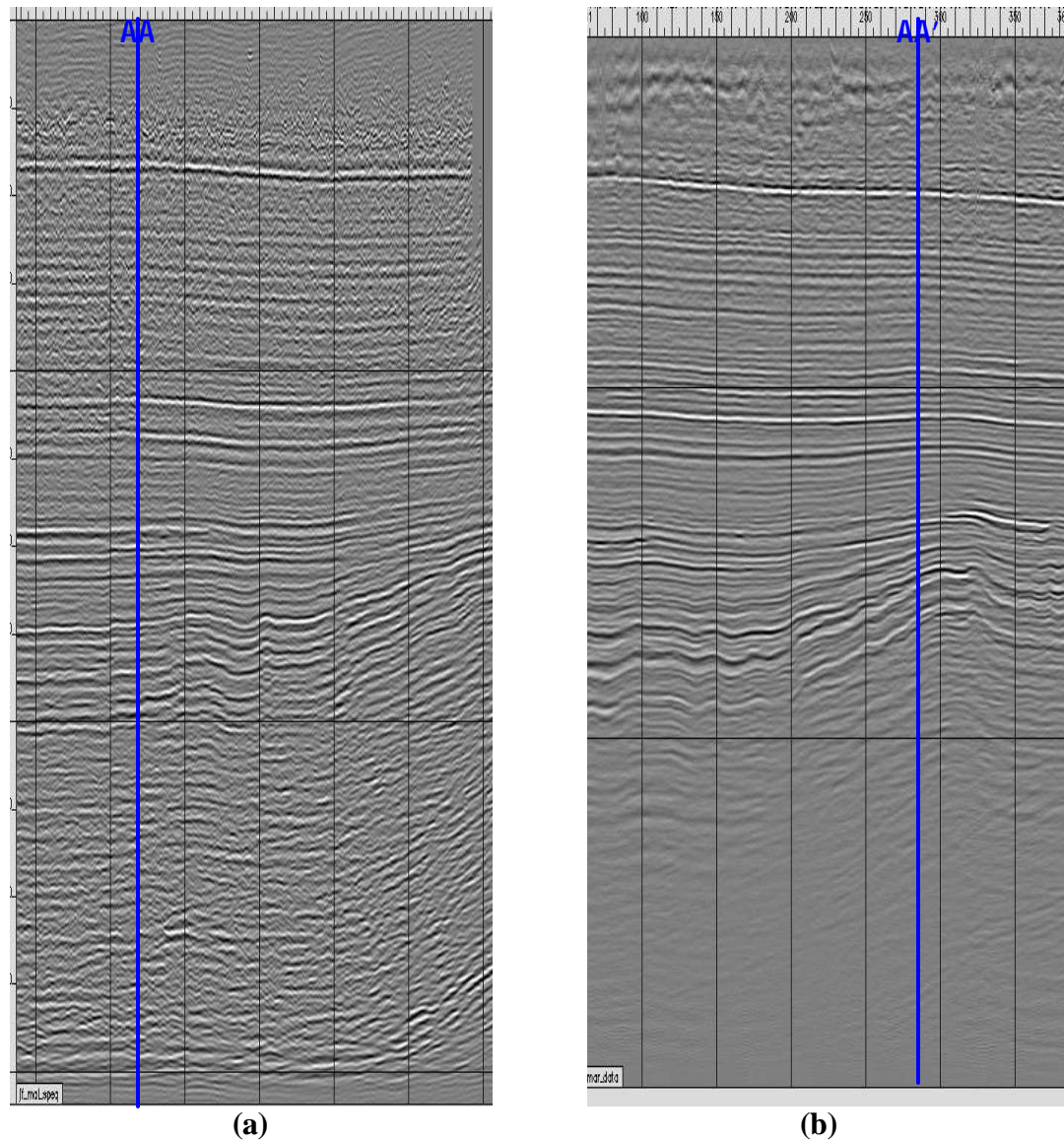
Figure 6.2 – A vertical section showing the seismic volumes taken along cross-section A-A'. (a) Maljamar; (b) Vacuum Field. The bounds of the overlapping section between the two surveys across line AA-AA' is indicated by the blue line.

Figure 6.2 is a vertical cross-section of the overlap between the two surveys. I use this cross-section as a quality control step. The red line is the line of intersection between the two surveys. Looking beyond the obvious differences in the imaging due to processing, the structure imaged in the Maljamar survey is analogous to the structure in the Vacuum Field data.

6.1   Grayburg Formation

I examined horizon extractions through the different geometric attribute volumes to analyze geologic structures seen on time slices as well as horizons of interest. The first horizon of interest picked and extracted is the Grayburg. The stratigraphic location of the Grayburg is shown in Figure 6.3 (red line).
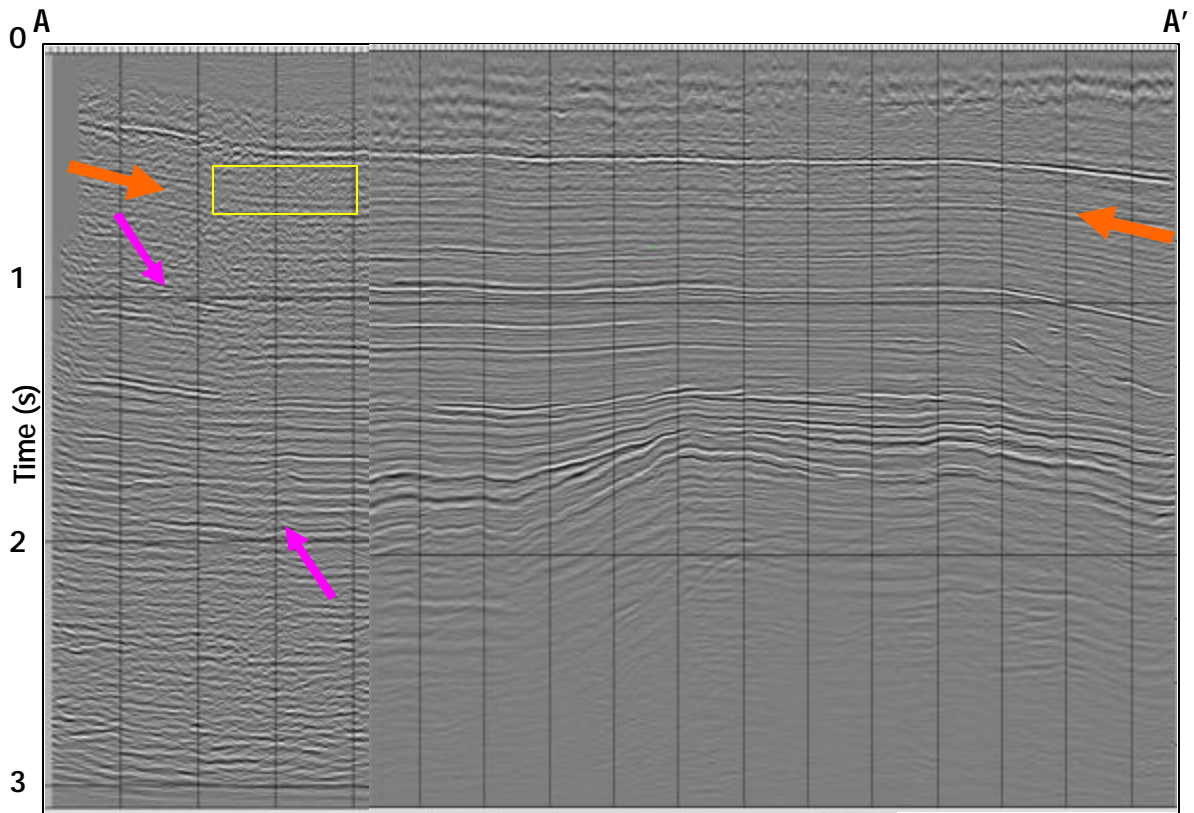
Figure 6.3 – The Grayburg Formation is indicated with orange arrows. Fuchsia arrows point out a fault cutting through the volume. This is verified in the coherence section in Figure 6.4 (red arrows).

Coherence was extracted along the Grayburg horizon through the two surveys. The Grayburg coherence extraction is shown in Figure 6.4. Areas of high coherence are in white whereas the less coherent areas are dark. Acquisition footprint is highly visible in both surveys, especially in Vacuum Field. The lack of coherence Maljamar side of the

Grayburg can be traced back to the vertical cross-section (Figure 6.3, yellow box). In the vertical section, the Grayburg Formation is continuous though somewhat broken up.

Despite the general low coherence of the Maljamar side, a fault is visible across in the coherence section, as pointed out in Figure 6.4 (red arrows). Acquisition footprint is visible in both surveys, especially on the Vacuum field side (red box). On the eastern side (Vacuum Field), the margin between the carbonate platform and the Brushy Canyon/Cherry Canyon siliciclastic slumps and slope deposits starts are imaged at this level (blue arrows). The slope deposits to the south are less coherent as in deeper sections, i.e. at the level of the Glorieta Formation (~1.2s). The Grayburg shelf progrades out over the Brushy Canyon slope.
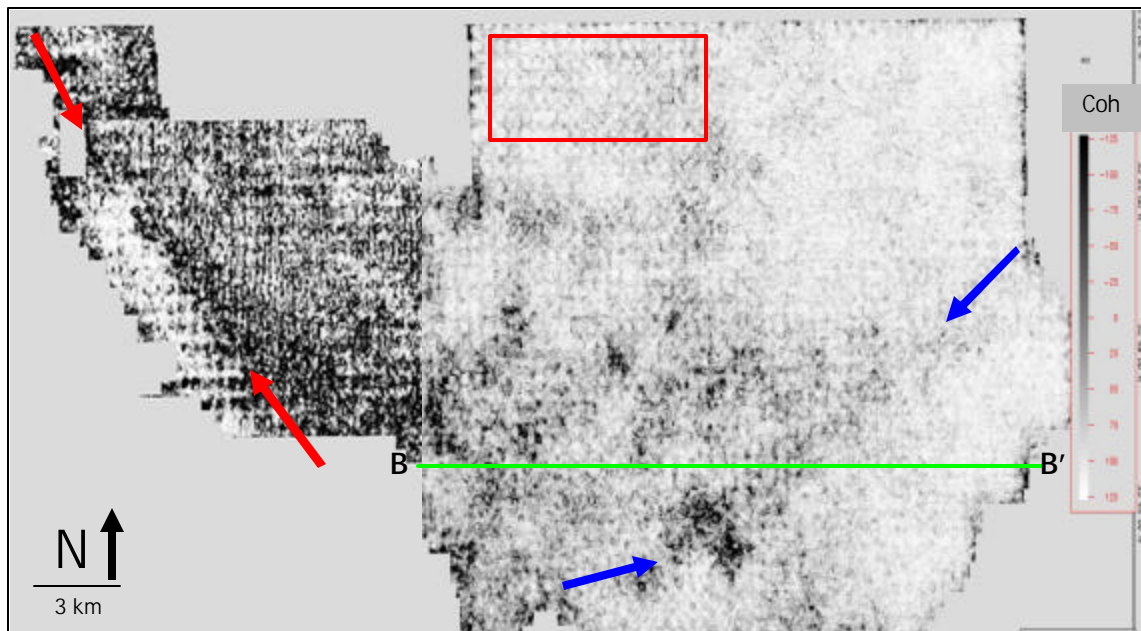
Figure 6.4 – Coherence extraction along the Grayburg horizon through the two surveys. The red and blue arrows point out the same fault which is the margin between the carbonate platform and the Brushy Canyon slump deposits

Figure 6.5 is the coherent energy gradient extraction of the Grayburg Formation. Faults identified on the coherence extraction are confirmed on this section and show up as low energy (zero values) on both surveys. The fault on the Maljamar side (red arrows) can be extrapolated to run across to Vacuum Field (yellow curve) and is in fact, the continuation of the buried platform margin. On the Vacuum Field side, the margin is not a true fault yet, as there is no visible trend in the vertical cross section B-B'. I show this in Figure 6.6. This feature has lower energy than the surrounding area and maybe the tip line of the fault. Channel edges close to the platform margin are imaged faintly (blue arrows). The N-S trending features to the north (fuchsia box) are acquisition footprint and not real geologic features.
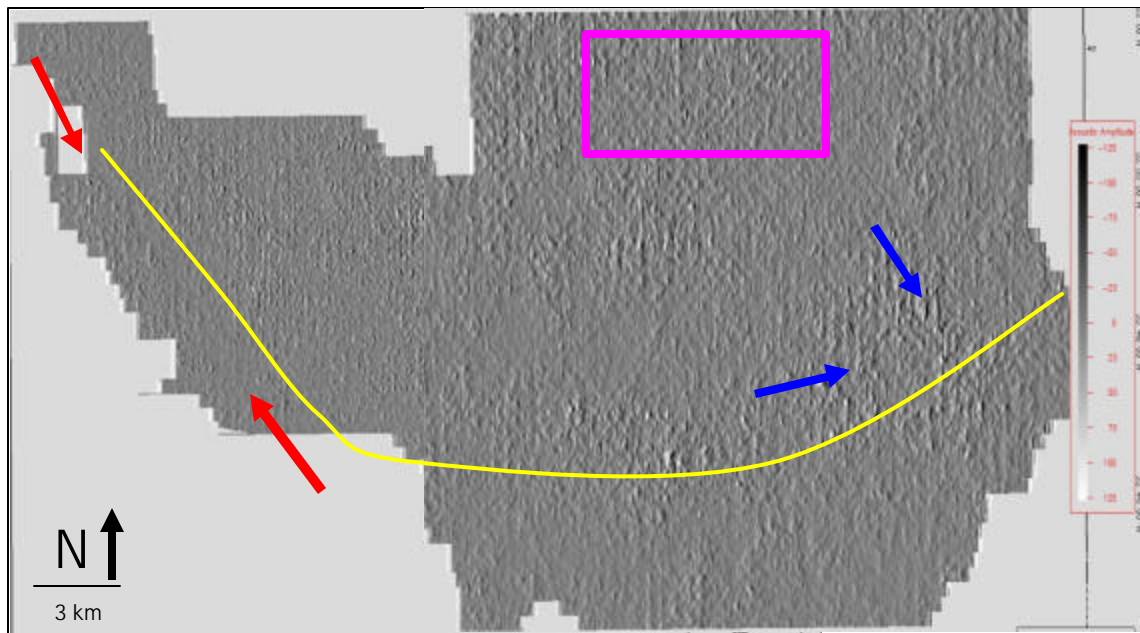
Figure 6.5 – Coherent energy gradient extraction along the Grayburg horizon through the two surveys. Acquisition footprint is still prevalent in both surveys, especially towards the north. The platform margin extends across the two surveys. Since the faults are highly incoherent, this has very low coherent energy of nearly zero.
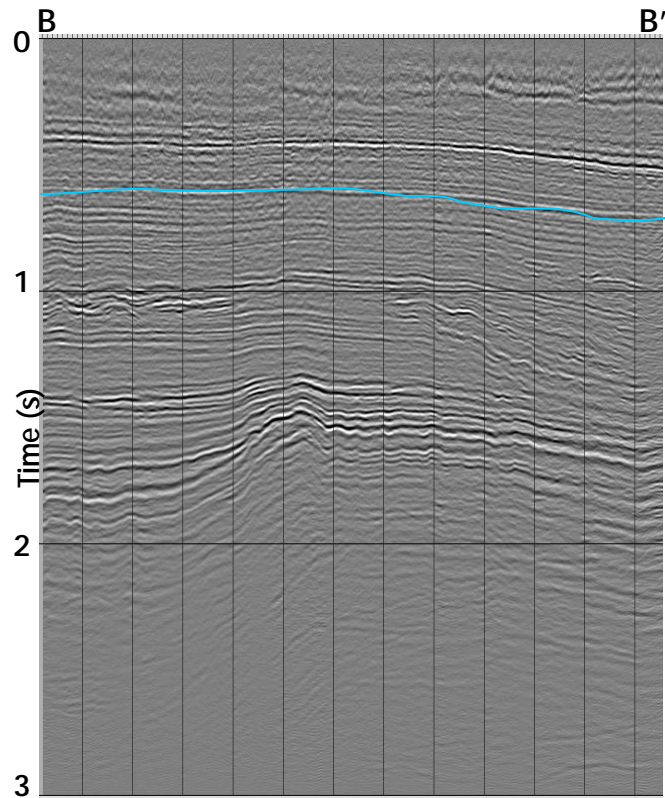
Figure 6.6 – Cross-section B-B' across Vacuum Field. The Grayburg is shown with blue pick. The Grayburg is relatively flat-lying and not heavily faulted across Vacuum Field.

The most negative curvature extraction of the Grayburg is shown on Figure 6.7 Features to the north of both surveys are not actual geologic structures but are acquisition footprint.   The platform margin faulting is imaged better in the negative curvature volume. I outline the extent of the fault in the red feeform.   In general, the fault has close to zero energy.   Edges of a deeper channel are imaged near the middle of the Vacuum Field survey (yellow arrow). The southern extents of the surveys do not display the slump deposits as the Grayburg shelf prograded over the older shelf margin.
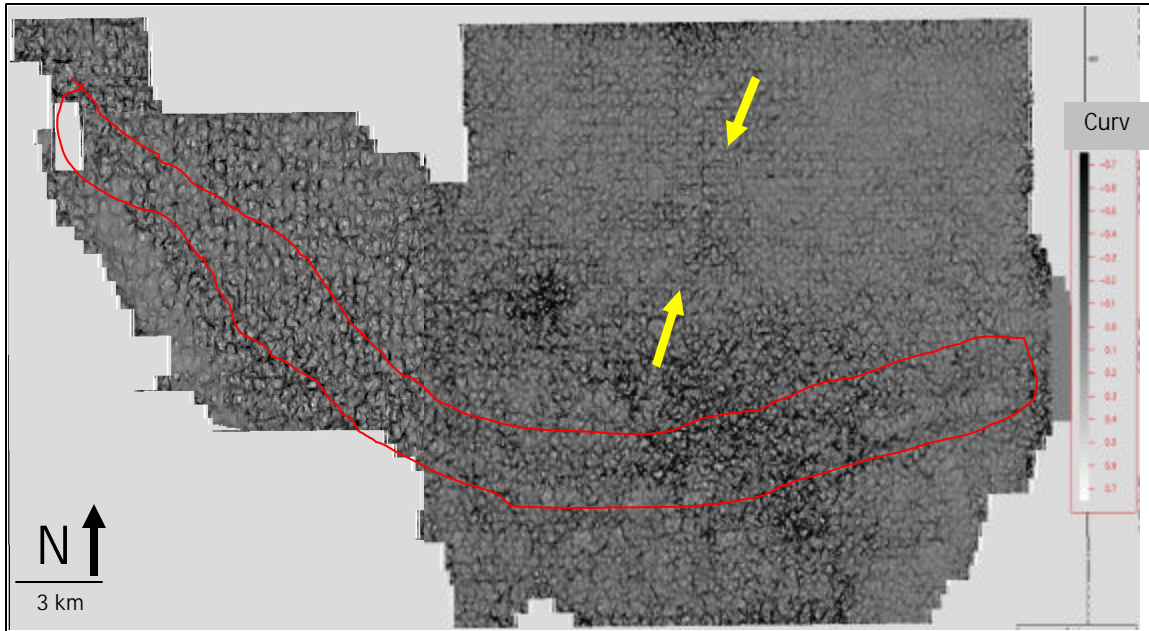
Figure 6.7 – Most negative curvature extraction along the Grayburg horizon through the two surveys. Compaction and faults along the platform margin are imaged nicely in this section.

Figure 6.8 is the most positive curvature extraction along the Grayburg horizon. Acquisition footprint is imprinted on both surveys, especially in the northern section. There is not much structure imaged in the Maljamar survey. The platform margin is still imaged along the section and is continuous across the two sections. Since negative and positive curvature are mathematically independent of each other, both volumes image slightly different segments of the same fault. The northern edge of the platform margin is highlighted in the positive curvature volume (red arrows), which is expected since this would have the highest relief/elevation before the horizon starts to dip south into the slumps.
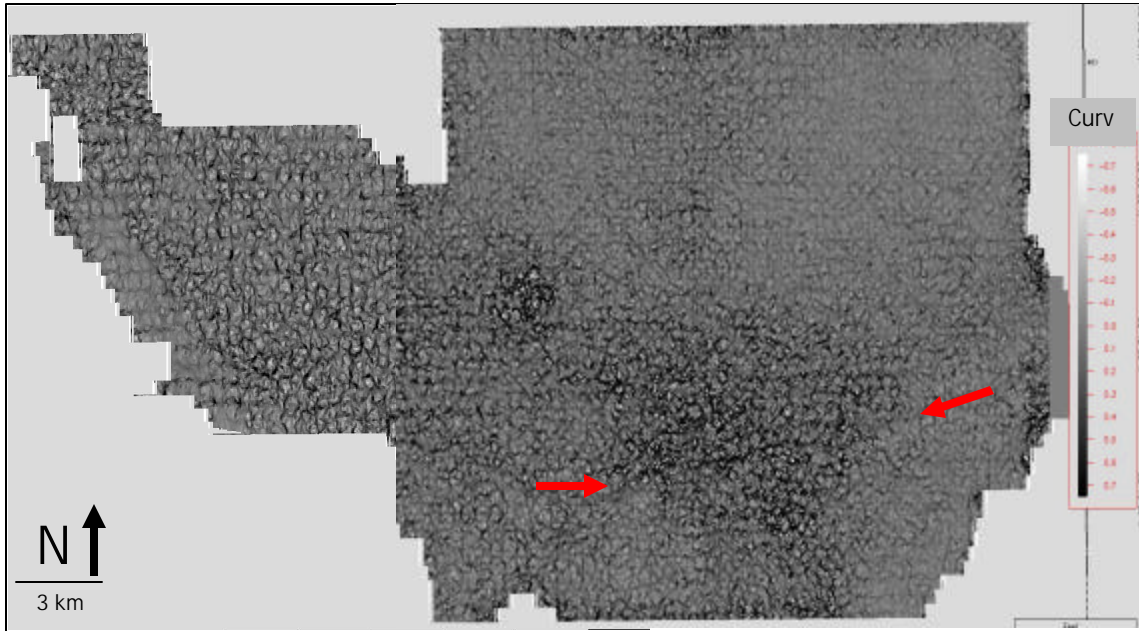
Figure 6.8 – Most positive curvature extraction along the Grayburg horizon through the two surveys. Red arrows point out the northern edge of the fault where the positive curvature attribute highlights this edge compared to the negative curvature.

6.2   Glorieta Formation

I extract the same suite of attributes along the Glorieta Formation. This horizon is important as this interval contains one of the more prolific reservoirs in the area. The Glorieta is situated at about 1.3s two-way traveltime (TWT), or approximately 1.5 km deep. I highlight the Glorieta in Figure 6.9. In the vertical section, the Glorieta appears to be relatively flat. Seismic attribute extractions show that there is a lot more subtle structure in the Glorieta.
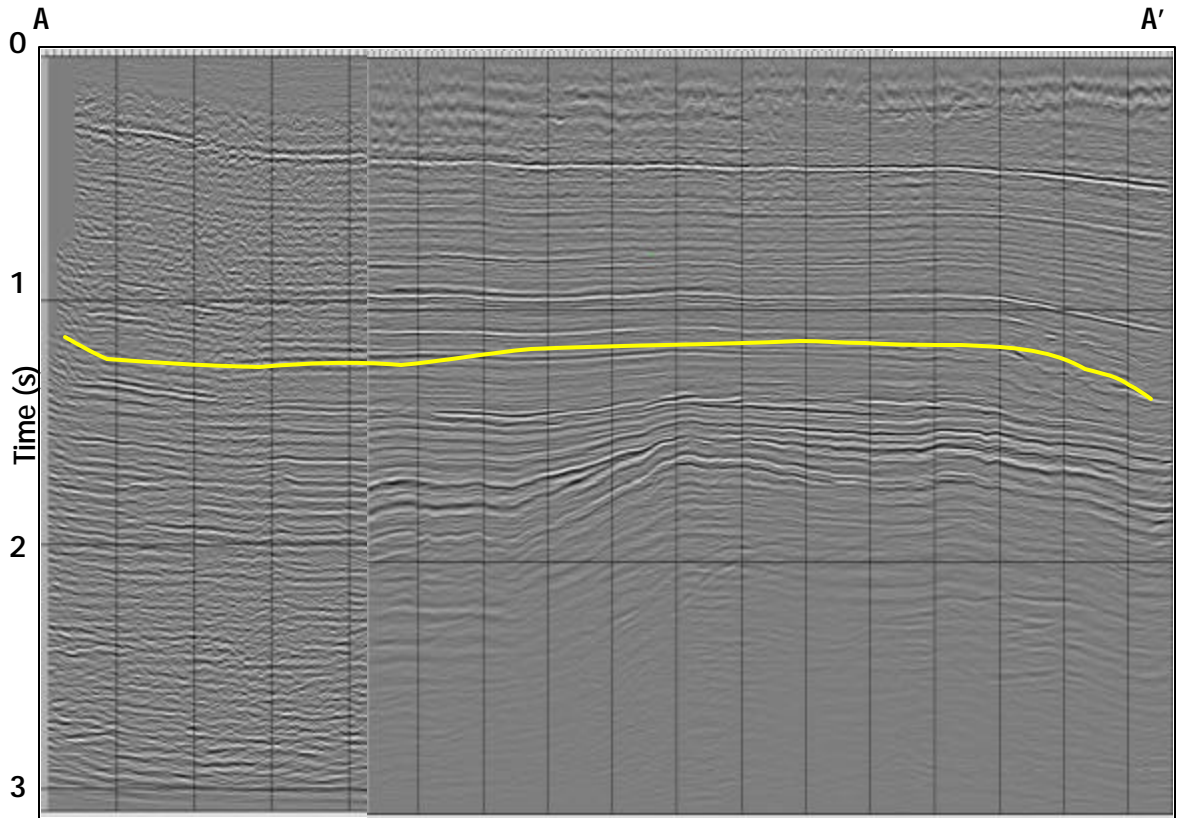
Figure 6.9 – Reference cross-section of the merged Vacuum-Maljamar survey showing the stratigraphic location of the Glorieta Formation. The Glorieta is situated at about 1.3s TWT, or approximately about 1.5 km deep.

Figure 6.10 is a coherence extraction through along the Glorieta horizon across the two surveys. Acquisition footprint is still slightly visible in both surveys, although not as pronounced as in the Grayburg level. The faults dividing the carbonate platform from the slump deposits are better defined at this level (red arrows). Crown faults delineating the breaking off of the slump deposits occur just slightly below the Grayburg. This platform margin is now more easily traced across the two surveys. The platform margin is nicely imaged in the coherence extraction as areas of low coherence.
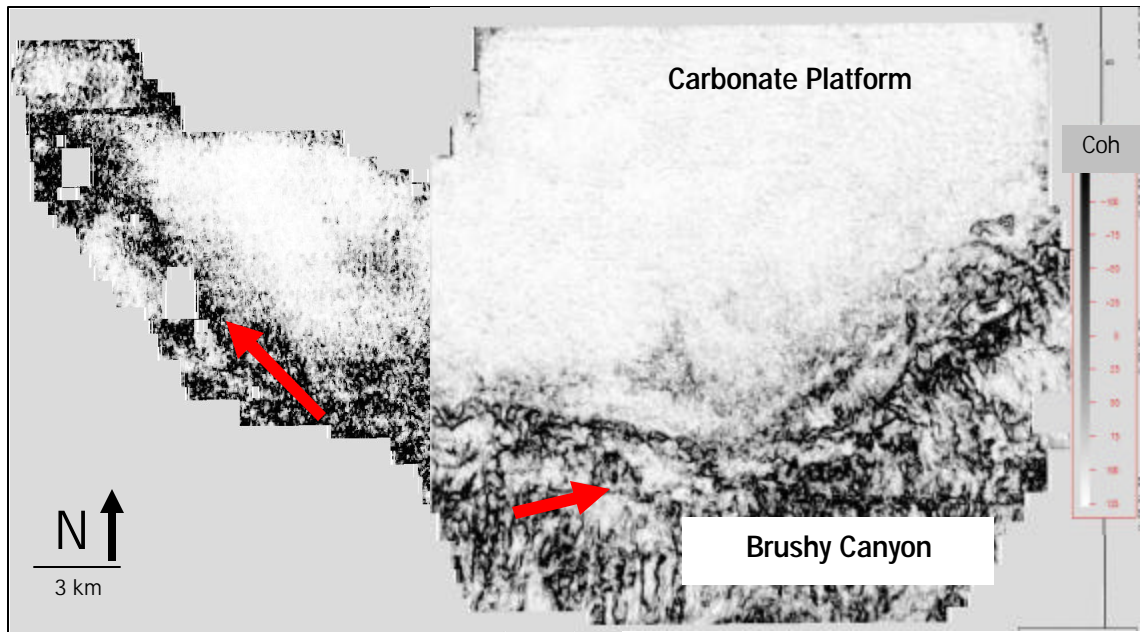
Figure 6.10 – Coherence extraction along the Glorieta horizon through the two surveys. Red arrows point to the margin between the carbonate platform and the slumps of the Brushy Canyon sediments.

Figure 6.11 is the coherent energy gradient extraction along the Glorieta horizon. This attribute proves efficient in imaging channels and fault edges at this level. The northern section of the survey is not too complex and hence is structurally quiet. A part of the channel system is imaged in the central part of the Vacuum Field survey. In the coherent energy volume, the margin is a low energy zone (yellow outline). The zones of low coherence in the Brushy Canyon are imaged in the coherent energy gradient volume as slump margins.
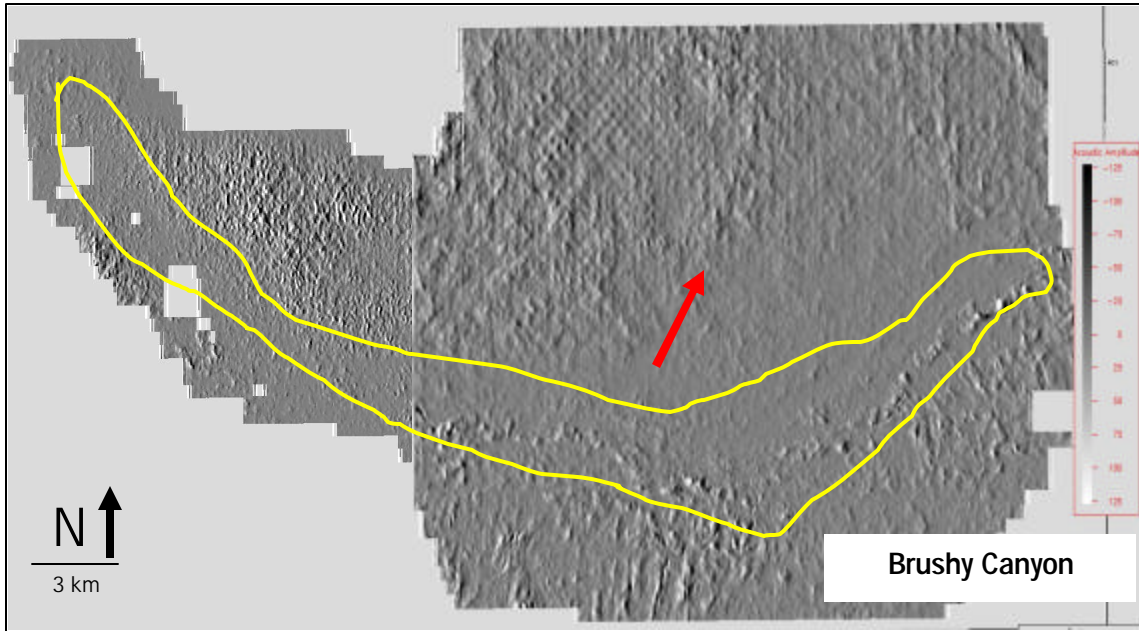
Figure 6.11 – Coherent energy gradient extraction along the Glorieta horizon through the two surveys. A channel is imaged in the middle of the Vacuum survey as pointed by the red arrow. The margin between the platform and the slump sediments is outlined in yellow. Slump edges are also imaged within the Brushy Canyon deposits.

The most negative curvature horizon extraction along the Glorieta is displayed in Figure 6.12. As in the preceding volumes, the northern section of the survey is structurally quiet. The negative curvature attribute works very well in imaging the platform margin. The imaging of the platform margin displays the robustness of the algorithm for calculating curvature. For the Vacuum Field survey, I picked the Glorieta horizon and interpolated across possible fault contacts. In the Maljamar survey, I have small zones where there are no horizon picks as the data is too chaotic to pick across the horizon (fuchsia boxes). The curvature algorithm is robust enough to identify changes in the energy within the vertical analysis window and image discontinuities despite it not confined to picked horizons as in Vacuum Field, or areas of no picks, like in Maljamar.
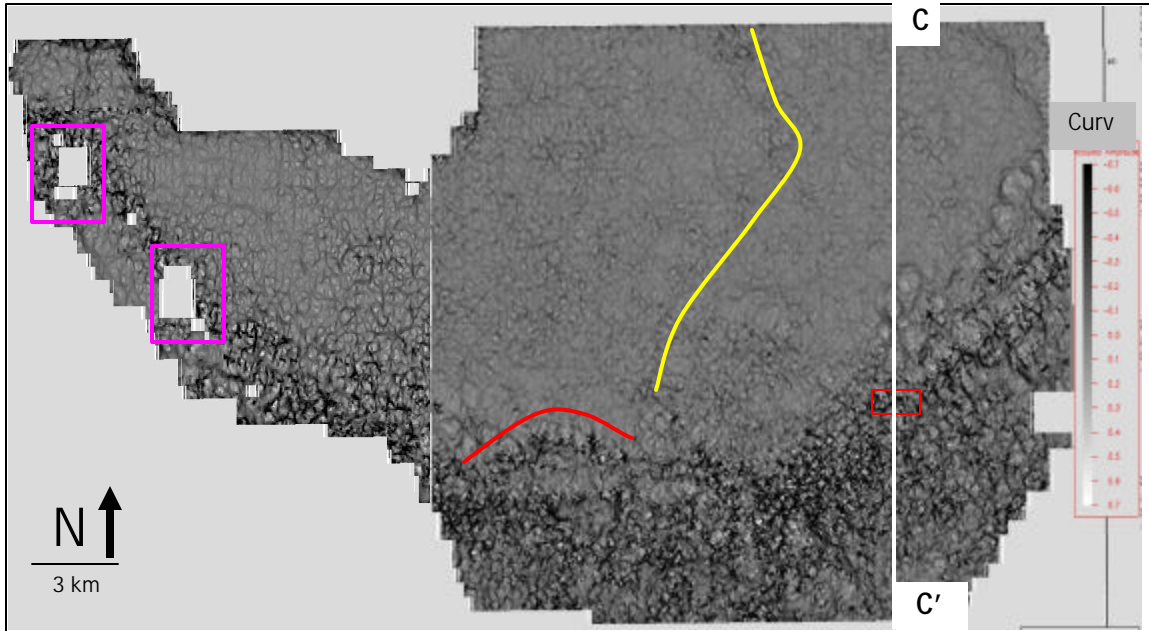
Figure 6.12 – Most negative curvature extraction along the Glorieta horizon through the two surveys. The red rectangle along line C-C' is the feature identified in Figure 6.14b. See text for full discussion.

A curvilinear feature is highlighted in the middle of the Vacuum Field survey (Figure 6.12, yellow curve) in the most negative curvature volume. Deeper horizons show this to be part of channel features. This feature is also visible in the most positive curvature volume, but not as clearly resolved. In the southwest part of the Vacuum Field survey, I identify a fault just slightly north of the slump deposits (red curve). This same fault is even more clearly imaged in the most positive curvature extraction. This shows the maximum curvature values are more positive than negative.

Figure 6.13 is the most positive curvature extraction along the Glorieta horizon. The channel imaged in the most negative curvature volume is not as visible in this section. The arrows point to features that show computational independence of the most negative and most positive curvatures. I display cross-section C-C' along the N-S direction in Figure 6.14a and a zoomed image of the Glorieta in 6.14b. In the zoomed

section, the arrows indicate the segments along the cross section that were imaged by the most negative and most positive curvatures. The most negative value found along the platform margin in Figure 6.12 corresponds to the concave feature on the picked Glorieta horizon (Figure 6.14b).
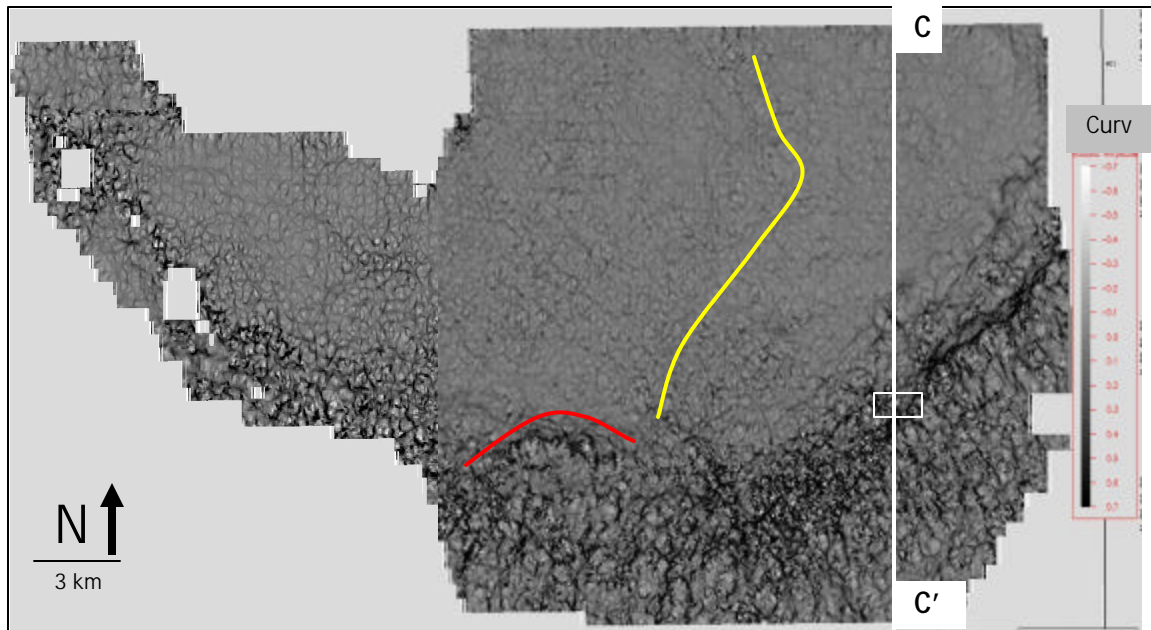
Figure 6.13 – Most positive curvature extraction along the Glorieta horizon through the two surveys. The white rectangle is the positive feature identified in Figure 6.14b. See text for full discussion.

In Figure 6.13, I label the most positive curvature value along the platform margin (white rectangle). I correlate this to the vertical section of cross-section C-C'. The margin corresponds to a segment along the Glorieta that convexes prior to sliding down the slump slopes (Figure 6.14b). The algorithm is robust enough to delineate between the two features despite the close proximity to each other.

(a)

(b)
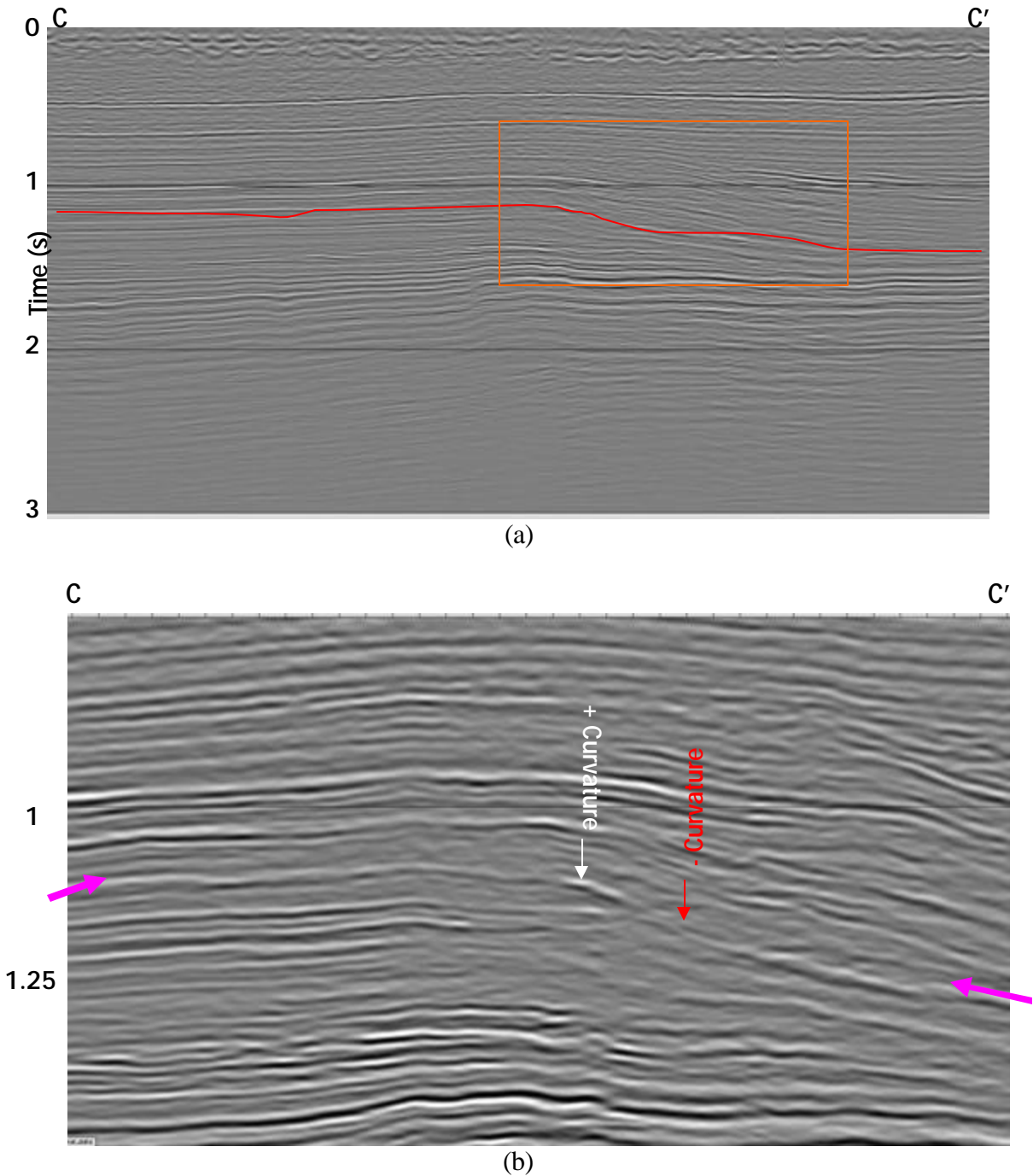
Figure 6.14 – Cross-section C-C' running N-S across the Vacuum Field survey. (a) The full three-second record; (b) A zoomed section as defined by orange box 6.14a with the Glorieta Formation indicated by arrows.

6.3 Mississipian Formation

Figure 6.15 is the reference cross-section of both Maljamar and Vacuum field showing the stratigraphic location of the Mississippian Formation. This level features several geologic structures, as the Mississippian strata have been affected by Pennsylvanian tectonic activity.
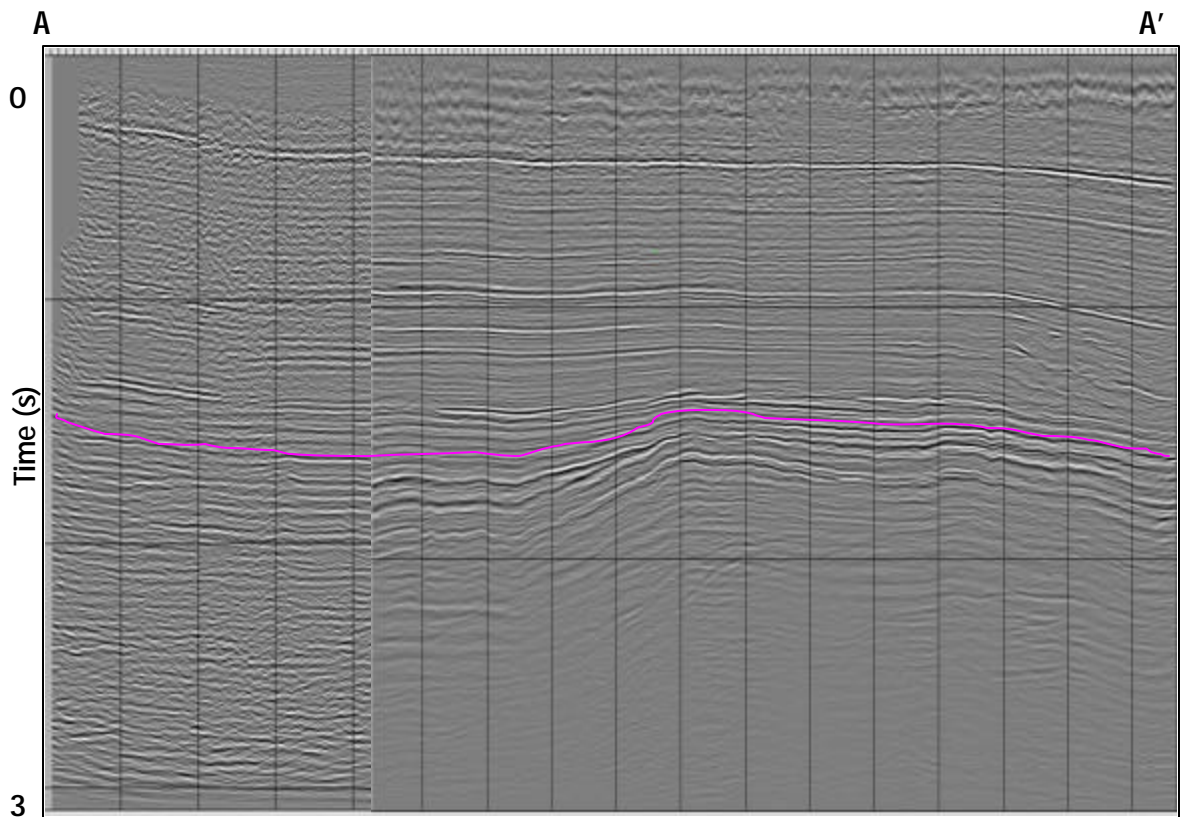
Figure 6.15 – Reference cross-section of the merged Vacuum-Maljamar survey showing the stratigraphic location of the Mississippian Formation (fuchsia line). The Mississippian is situated at about 1.6s TWT.

The coherence extraction of the Mississippian across both surveys is shown in Figure 6.16. As this horizon is deeper than the previous picked horizons, acquisition footprint is not seen at this level. The Mississippian has a fairly high coherence across

the surveys, although several faults cut across the horizon. The remnants of the platform margin can be seen along the NW side of the Maljamar survey. The faults on the east side of the Maljamar survey can be interpolated to connect across to the Vacuum Field survey and run towards the north. Two other faults cut across Vacuum, one in the southern extent which I highlight with red arrows, and one running E-W near the eastern side (green arrow). The slope deposits of the Brushy Canyon are still visible, though the southern section of Maljamar is more coherent than in the shallower sections.
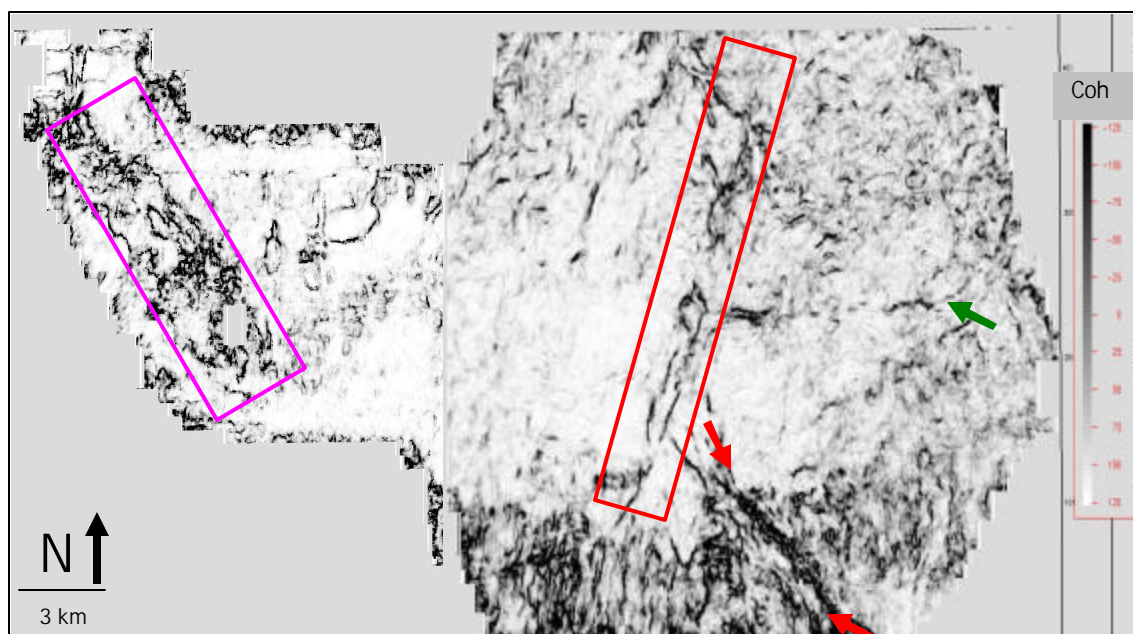
Figure 6.16 – Coherence extraction along the Mississippian Formation across the Maljamar and Vacuum Field surveys. At this level, the horizon is relatively clear of acquisition footprint and is cut by several faults.

Figure 6.17 is the coherent energy gradient extraction of the Mississippian Formation. The remnant of the platform margin in Maljamar (yellow polygon) is faintly imaged. The Vacuum Field side shows more structure than the Maljamar side. The fault I identify in the eastern side of Vacuum is imaged in this horizon slice (yellow arrows). I

also point to a fault that is well defined in the coherent gradient section (teal arrows), although in the coherence slice, only the northern extent is imaged. A marked improvement of the coherent energy gradient over the coherence section is that channels are imaged to reside within the extents of the faults (red box).
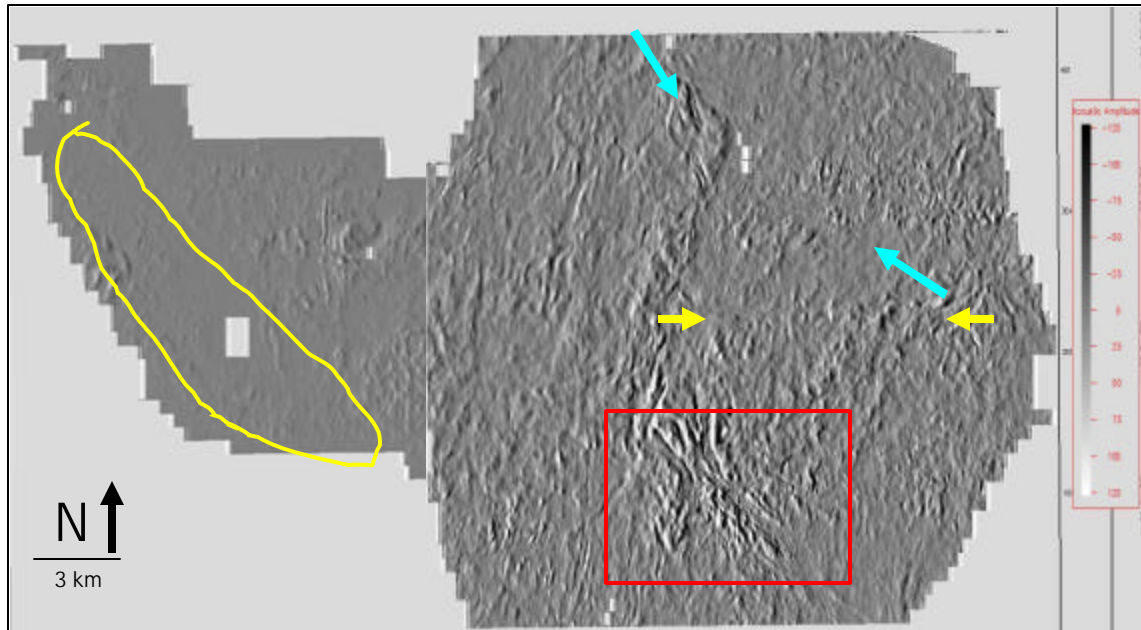
Figure 6.17 – Coherent energy gradient extraction along the Mississippian Formation across the Maljamar and Vacuum Field surveys.

Figure 6.18 is the most negative curvature extraction along the Mississippian across both surveys. The attribute shows the faulting across Vacuum Field very nicely. The channels imaged within the faults in Figure 6.17 are better defined in the most negative curvature volume. The fault trending N-S across both surveys actually extends to the south into the slope deposits. The edge of the remnants of the platform margin is crisper in both curvature volumes.
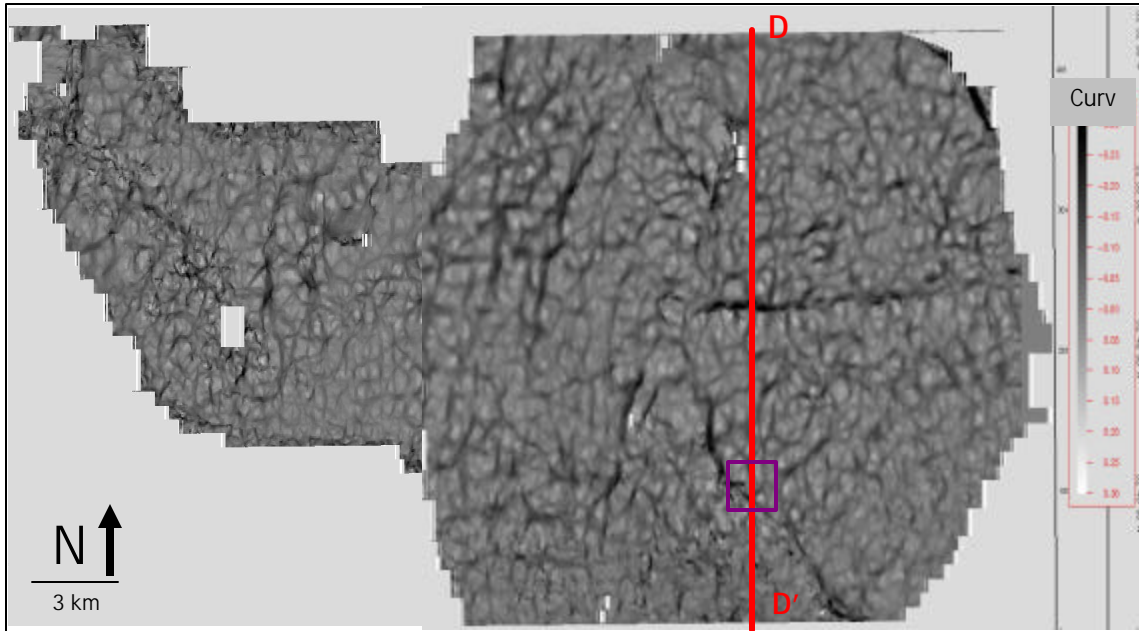
Figure 6.18 – Most negative curvature extraction along the Mississippian Formation across the Maljamar and Vacuum Field surveys. See text for discussion.

Figure 6.19 is the most positive curvature extraction of the Mississippian Formation. Cross-section D-D' runs N-S across Vacuum Field. Figure 6.20 shows cross-section D-D' across vacuum Field. Local highs along the horizon correspond with displays as most positive maximum curvature (yellow box) in the most positive curvature extraction. A fault break near the southern section (Figure 6.19, purple box) correlates to the maximum negative value in the most negative curvature extraction.
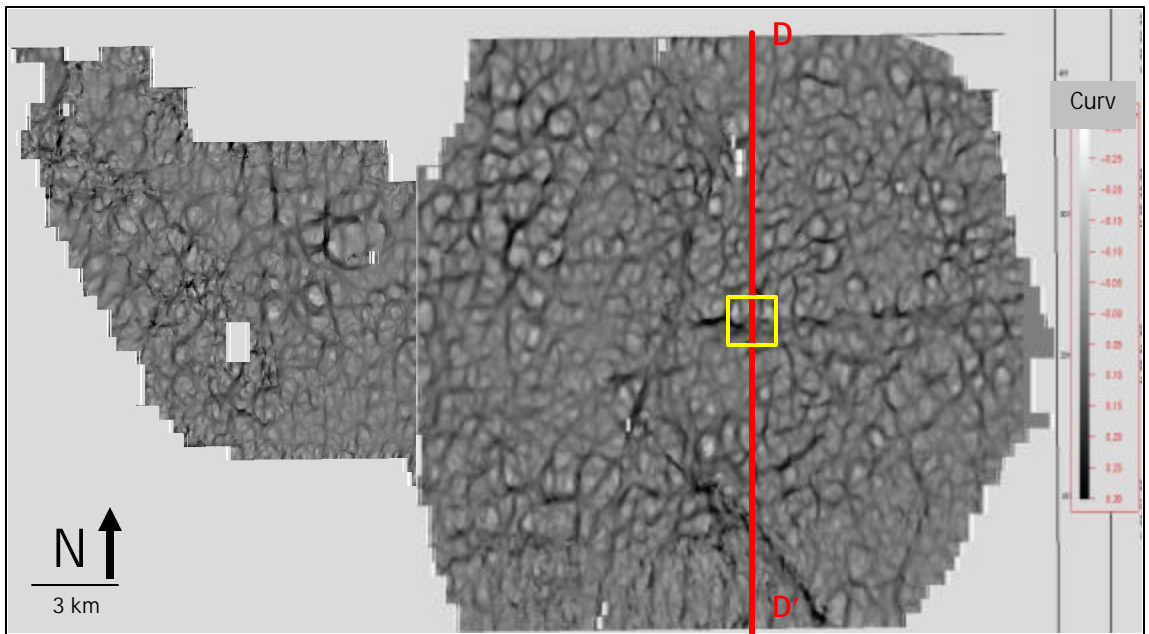
Figure 6.19 – Most positive curvature extraction along the Mississippian Formation across the Maljamar and Vacuum Field surveys.
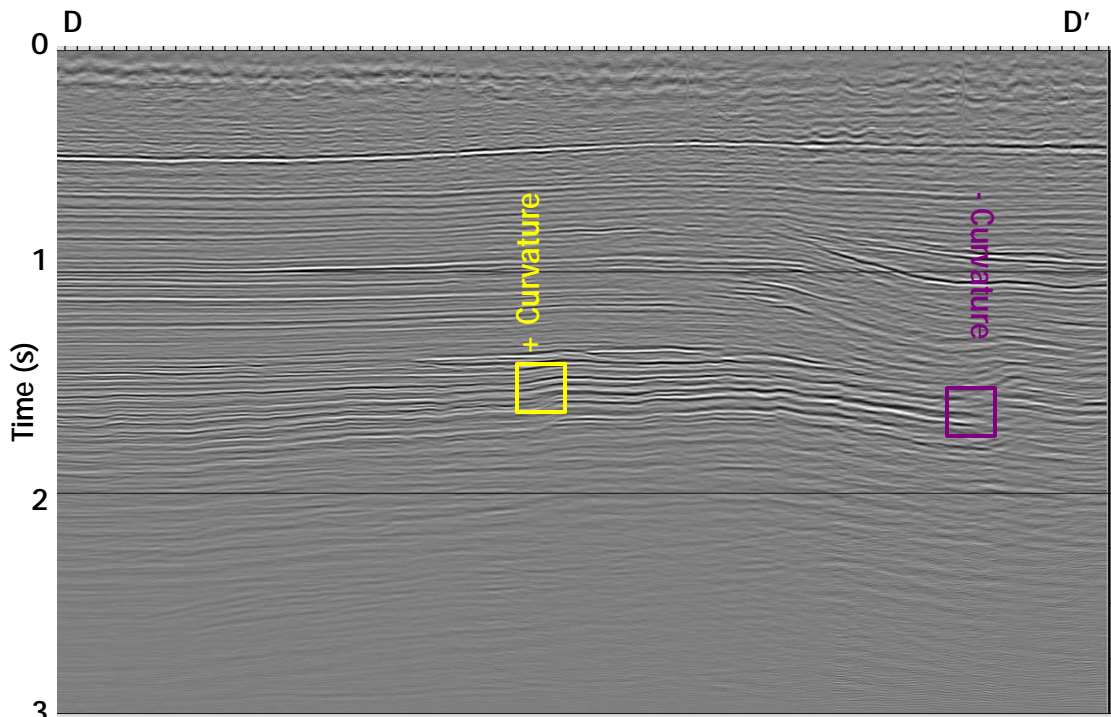
Figure 6.20 – Cross-section D-D'. The yellow and purple boxes correspond to the features highlighted in Figure 6.18 and 6.19.

Chapter 7

CONCLUSIONS AND FUTURE DIRECTION

The use of geometric attributes like coherence, coherent energy gradients, and curvature provides a means of evaluating alternative processing parameters and workflows in terms of the imaging of geologic features on time slices. In my workflow, ground roll filtering proves effective in removing most of the components of coherent noise and provides the most significant improvement on the imaging of geologic features. Ground roll filtering also helps in the subsequent processing stream, especially velocity analysis, where the near-offset traces are more continuous. In the final migrated sections, reflectors in the ground roll filtered volumes shows better lateral continuity compared to the volume where the ground roll was not filtered.

The different geometric attributes display different sensitivity top noise as well as to different kinds of processing errors. Attributes like coherence are efficient in imaging edges of features and show particular sensitivity to coherent noise such as back-scattered ground roll. The difference in azimuth for each bin location also affects the coherence calculation. Coherent energy gradients also exhibit sensitivity to coherent noise as well as preservation of seismic amplitude. Curvature shows sensitivity to imaging false structure due to inaccurate velocities.

The Vacuum Field-Maljamar data set proves to be a good laboratory in testing the imaging of subsurface using geometric attributes. Coherence proves proficient in imaging between the carbonate platform and slump deposits. Coherence also images faults not visible in the conventional seismic section. The coherent energy gradients

prove efficient in imaging the slump deposits of the Brushy Canyon sediments. Curvature volumes are proves powerful in imaging the platform margin.

APPENDIX A

VACUUM-MALJAMAR PROCESSING WORKFLOWS

A.1   Flow One: Migrated brute stack with attributes

```
┌─────────────────────────────┐
│        Original Data        │
└─────────────────────────────┘
              │
              ▼
┌─────────────────────────────┐
│       Datum Correction      │
└─────────────────────────────┘
              │
              ▼
┌─────────────────────────────┐
│            Stack            │
└─────────────────────────────┘
              │
              ▼
┌─────────────────────────────┐
│          Migration          │
└─────────────────────────────┘
              │
              ▼
┌─────────────────────────────┐
│     Geometric Attributes    │
└─────────────────────────────┘
```
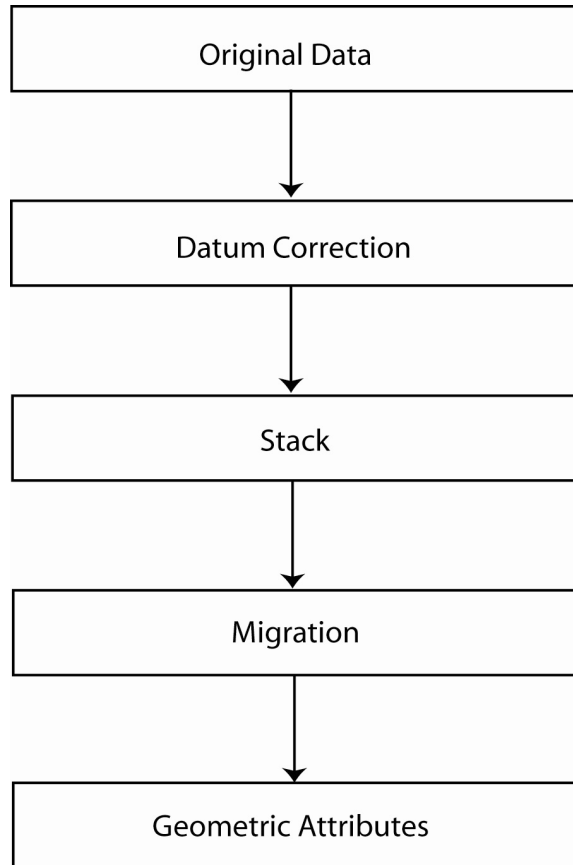
The first flow for the Vacuum-Maljamar data set was the brute migration flow. Datum correction was applied to the data to a datum level of 2000 ft. The data was stacked and then migrated using a single velocity function. Geometric attributes were generated using algorithms from the Allied Geophysical Laboratories at the University of Houston and the Stanford Exploration Project (SEP) codes. List of attributes generated are listed in Appendix B.

A.2   Flow Two: Ground-roll filtered migration with attributes

```
┌─────────────────────────────────┐
│          Original Data          │
└─────────────────────────────────┘
                 │
                 ▼
┌─────────────────────────────────┐
│         Datum Correction        │
└─────────────────────────────────┘
                 │
                 ▼
┌─────────────────────────────────┐
│       Ground-roll Filtering     │
└─────────────────────────────────┘
                 │
                 ▼
┌─────────────────────────────────┐
│              Stack              │
└─────────────────────────────────┘
                 │
                 ▼
┌─────────────────────────────────┐
│            Migration            │
└─────────────────────────────────┘
                 │
                 ▼
┌─────────────────────────────────┐
│       Geometric Attributes      │
└─────────────────────────────────┘
```
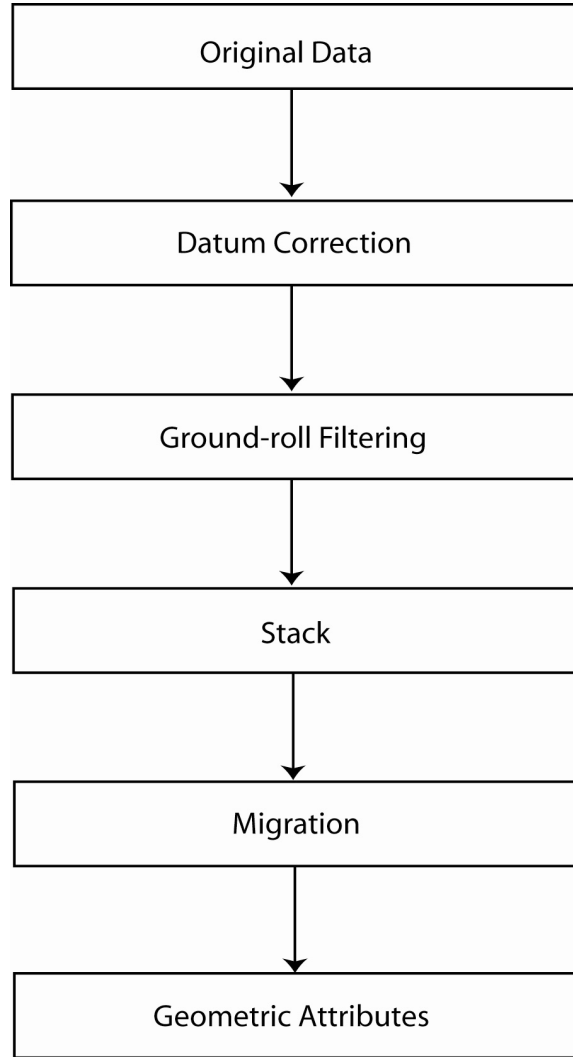
The second processing flow is fairly similar to flow one, with the major difference is the filtering of the ground-roll. Ground-roll was filtered in a cascading manner where a component of ground-roll is filtered out and the resulting data volume is again filtered with another component filtered out, and so forth. The different components filtered out ranges from 1500 fps to 2000 fps (457 m/s to 610 m/s).

A.3   Flow Three: Mid-process stack with outside mute, migration and attributes

```
┌─────────────────────────────┐
│        Original Data        │
└─────────────────────────────┘
               │
               ▼
┌─────────────────────────────┐
│       Datum Correction      │
└─────────────────────────────┘
               │
               ▼
┌─────────────────────────────┐
│     Ground-roll Filtering   │
└─────────────────────────────┘
               │
               ▼
┌─────────────────────────────┐
│         Outside Mute        │
└─────────────────────────────┘
               │
               ▼
┌─────────────────────────────┐
│        Deconvolution        │
└─────────────────────────────┘
               │
               ▼
┌─────────────────────────────┐
│     Velocity Estimation     │
└─────────────────────────────┘
               │
               ▼
┌─────────────────────────────┐
│            Stack            │
└─────────────────────────────┘
               │
               ▼
┌─────────────────────────────┐
│          Migration          │
└─────────────────────────────┘
               │
               ▼
┌─────────────────────────────┐
│     Geometric Attributes    │
└─────────────────────────────┘
```
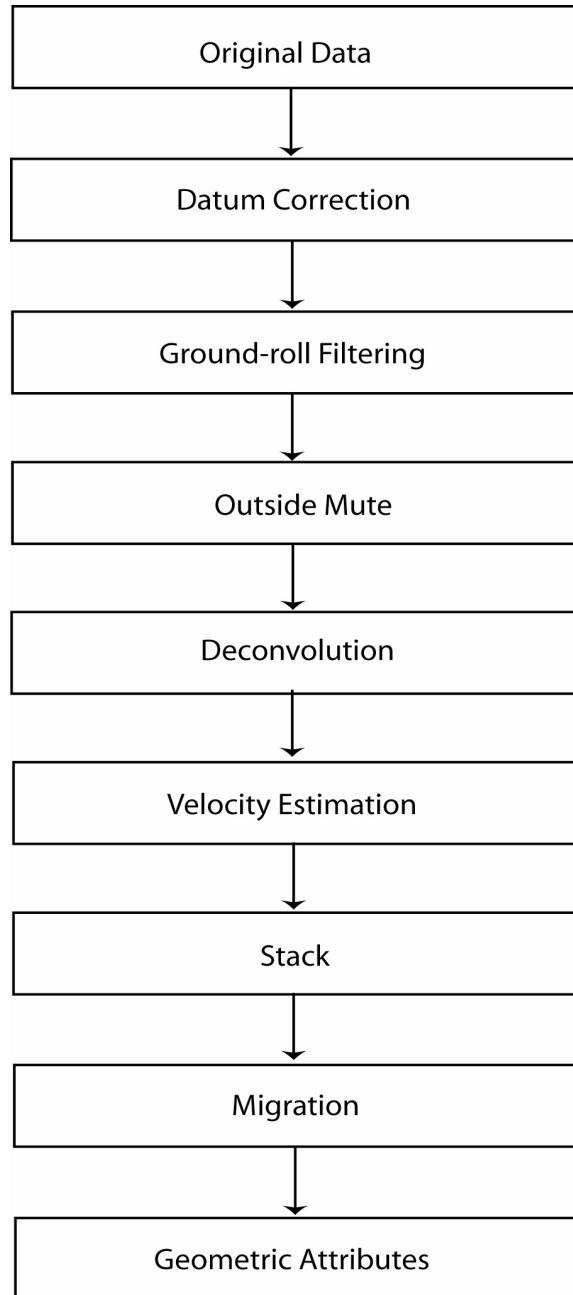
Flow three continues on flow two, using the same ground roll filtered data as input. A chimney mute is implemented to remove first arrivals.

A.4   Flow Four

```
┌─────────────────────────────┐
│        Original Data        │
└─────────────────────────────┘
              │
              ▼
┌─────────────────────────────┐
│       Datum Correction      │
└─────────────────────────────┘
              │
              ▼
┌─────────────────────────────┐
│     Ground-roll Filtering   │
└─────────────────────────────┘
              │
              ▼
┌─────────────────────────────┐
│        Outside Mute         │
└─────────────────────────────┘
              │
              ▼
┌─────────────────────────────┐
│         Inside Mute         │
└─────────────────────────────┘
              │
              ▼
┌─────────────────────────────┐
│        Deconvolution        │
└─────────────────────────────┘
              │
              ▼
┌─────────────────────────────┐
│     Velocity Estimation     │
└─────────────────────────────┘
              │
              ▼
┌─────────────────────────────┐
│            Stack            │
└─────────────────────────────┘
              │
              ▼
┌─────────────────────────────┐
│             FXY             │
└─────────────────────────────┘
              │
              ▼
┌─────────────────────────────┐
│          Migration          │
└─────────────────────────────┘
              │
              ▼
┌─────────────────────────────┐
│     Geometric Attributes    │
└─────────────────────────────┘
```
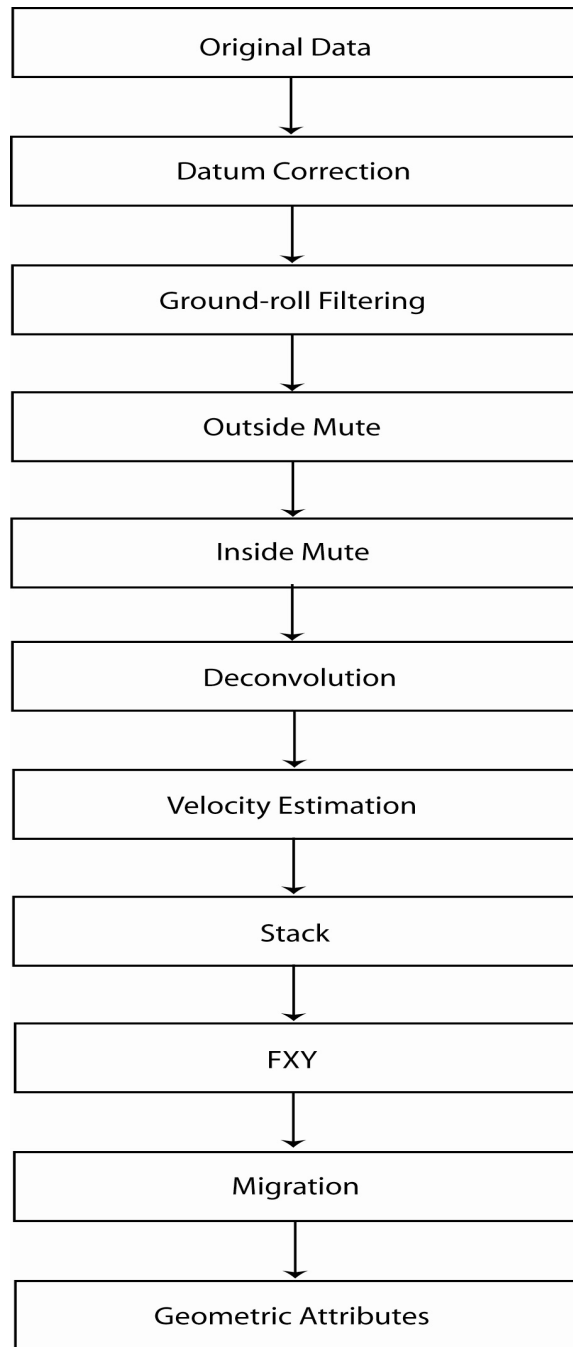
A.5   Flow Five: Mid-process stack, no ground-roll filtering, with attributes

```
┌─────────────────────────────────────┐
│           Original Data             │
└─────────────────────────────────────┘
                  │
                  ▼
┌─────────────────────────────────────┐
│          Datum Correction           │
└─────────────────────────────────────┘
                  │
                  ▼
┌─────────────────────────────────────┐
│           Outside Mute              │
└─────────────────────────────────────┘
                  │
                  ▼
┌─────────────────────────────────────┐
│           Inside Mute               │
└─────────────────────────────────────┘
                  │
                  ▼
┌─────────────────────────────────────┐
│          Deconvolution              │
└─────────────────────────────────────┘
                  │
                  ▼
┌─────────────────────────────────────┐
│         Velocity Estimation         │
└─────────────────────────────────────┘
                  │
                  ▼
┌─────────────────────────────────────┐
│              Stack                  │
└─────────────────────────────────────┘
                  │
                  ▼
┌─────────────────────────────────────┐
│               FXY                   │
└─────────────────────────────────────┘
                  │
                  ▼
┌─────────────────────────────────────┐
│            Migration                │
└─────────────────────────────────────┘
                  │
                  ▼
┌─────────────────────────────────────┐
│        Geometric Attributes         │
└─────────────────────────────────────┘
```
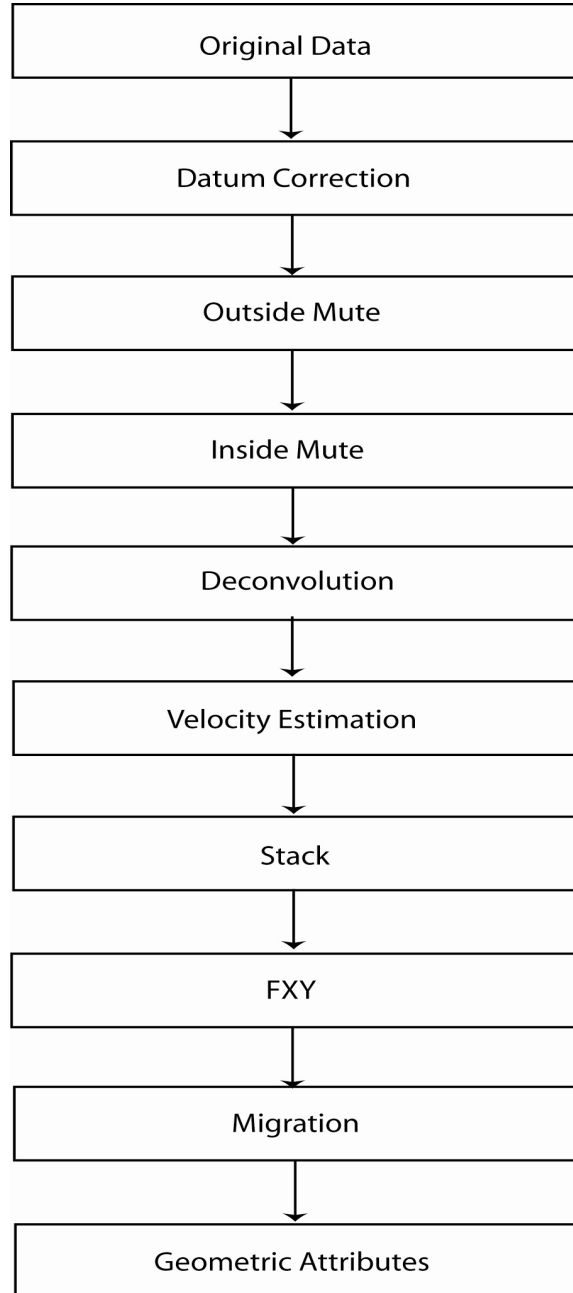
Flow five is a full sequence, conventional processing flow without the ground-roll filtering. I followed this processing sequence in order to compare the effects in attribute imaging of a conventional processing sequence with that of conventional processing with ground-roll removal.

A.5 Flow Six: Final Stack with Attributes

```
┌─────────────────────────────────┐
│         Original Data           │
└─────────────────────────────────┘
                │
                ▼
┌─────────────────────────────────┐
│        Datum Correction         │
└─────────────────────────────────┘
                │
                ▼
┌─────────────────────────────────┐
│       Ground-roll Filtering     │
└─────────────────────────────────┘
                │
                ▼
┌─────────────────────────────────┐
│          Outside Mute           │
└─────────────────────────────────┘
                │
                ▼
┌─────────────────────────────────┐
│          Inside Mute            │
└─────────────────────────────────┘
                │
                ▼
┌─────────────────────────────────┐
│         Deconvolution           │
└─────────────────────────────────┘
                │
                ▼
┌─────────────────────────────────┐
│       Velocity Estimation       │
└─────────────────────────────────┘
                │
                ▼
┌─────────────────────────────────┐
│       Velocity Estimation       │
└─────────────────────────────────┘
                │
                ▼
┌─────────────────────────────────┐
│             Stack               │
└─────────────────────────────────┘
                │
                ▼
┌─────────────────────────────────┐
│              FXY                │
└─────────────────────────────────┘
                │
                ▼
┌─────────────────────────────────┐
│           Migration             │
└─────────────────────────────────┘
                │
                ▼
┌─────────────────────────────────┐
│       Geometric Attributes      │
└─────────────────────────────────┘
```
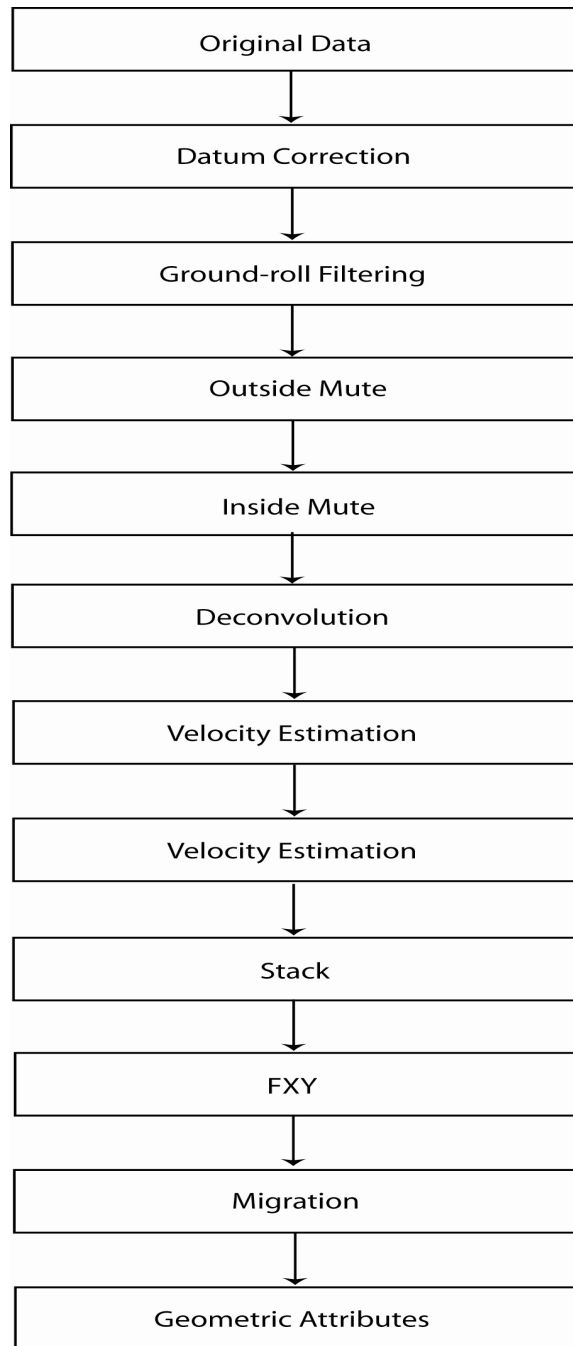
Flow six is a full sequence, conventional processing flow with the ground-roll filtering. This is best compared with flow number five as it follows identical processing flows with flow six having ground roll which was not done in flow five.

A.7 Flow Seven: Final stack with spectral balancing and attributes

```
┌─────────────────────────────┐
│        Original Data        │
└─────────────────────────────┘
              │
              ▼
┌─────────────────────────────┐
│       Datum Correction      │
└─────────────────────────────┘
              │
              ▼
┌─────────────────────────────┐
│     Ground-roll Filtering   │
└─────────────────────────────┘
              │
              ▼
┌─────────────────────────────┐
│        Outside Mute         │
└─────────────────────────────┘
              │
              ▼
┌─────────────────────────────┐
│         Inside Mute         │
└─────────────────────────────┘
              │
              ▼
┌─────────────────────────────┐
│        Deconvolution        │
└─────────────────────────────┘
              │
              ▼
┌─────────────────────────────┐
│      Velocity Estimation    │
└─────────────────────────────┘
              │
              ▼
┌─────────────────────────────┐
│      Velocity Estimation    │
└─────────────────────────────┘
              │
              ▼
┌─────────────────────────────┐
│            Stack            │
└─────────────────────────────┘
              │
              ▼
┌─────────────────────────────┐
│             FXY             │
└─────────────────────────────┘
              │
              ▼
┌─────────────────────────────┐
│          Migration          │
└─────────────────────────────┘
              │
              ▼
┌─────────────────────────────┐
│      Frequency Balancing    │
└─────────────────────────────┘
              │
              ▼
┌─────────────────────────────┐
│      Geometric Attributes   │
└─────────────────────────────┘
```
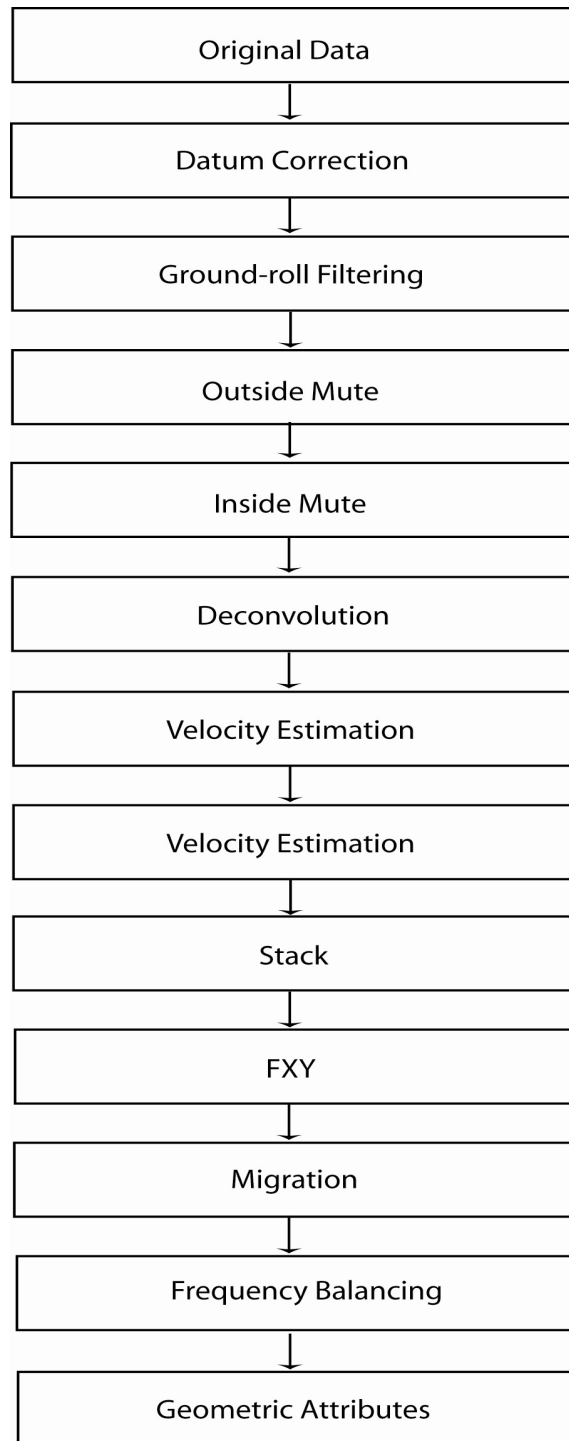
Flow seven is similar to flow six, with the added step of frequency balancing done post-migration in order to increase the frequency content of the data. This is

compared with the output volume from flow number six to determine if the added fidelity

of a higher frequency volumes results in better imaging in attribute space.

REFERENCES

Anstey, N. A., 1986. Whatever Happened to ground roll?: The Leading Edge **5 No. 3**, 40-45.

Bahorich, M. and S. Farmer, 1995, 3-D Seismic discontinuity for faults and stratigraphic features - The Coherence Cube: The Leading Edge **14,** 1053-1058.

Benson, R.D., and T. L. Davis, 2000, Time-lapse Seismic monitoring and dynamic reservoir characterization, Central Vacuum Unit, Lea County, New Mexico: SPE Reservoir Evaluation and Engineering **3**, 88-97.

Brown, A. R., 1999, Interpretation of Three-Dimensional Seismic Data, AAPG Memoir **42**/SEG Investigations in Geophysics **No. 9**.

Famini, J. A. T., K. J. Marfurt, and E. C. Sullivan, 2003, Effects of seismic reprocessing on selected seismic attributes: A case study in the Permian Basin: West Texas Geological Society Annual Fall Symposium **112**, 123-134.

FOCUS 5.2 Users Guide, 2005, Paradigm Geophysical Corporation.

Gulanay, N., 1999. Acquisition geometry footprints removal. SEG Expanded Abstracts, 637-640.

Hill, C., 1996, Geology of the Delaware Basin Guadalupe, Apache, and Glass Mountains, New Mexico and West Texas. Permian Basin Section – SEPM **39**.

Hills, J. M., 1984. Sedimentation, Tectonism, and Hydrocarbon Generation in the Delaware Basin, West Texas and Southeastern New Mexico. AAPG Bulletin **68**, 250-267.

Horak, R. L., 1985. Trans-Pecos Tectonism and its effect on the Permian Basin, In Dickerson, P.W. and Muehlberger, W.R., eds. Structure and Tectonics of Trans-Pecos Texas: West Texas Geological Society, Publication **81**, 81-87.

Jyosyula, S. P., 2003. Azimuthally Dependent Seismic Attribute Analysis: MS Thesis, University of Houston, 156 p.

Kerans, C. and W. M. Fitchen, 1995, Sequence hierarchy and facies architecture of a carbonate ramp system: San Andres Formation of Algerita Escarpment and Western Guadalupe Mountains, West Texas and New Mexico. Report of Investigations **No. 235.** Bureau of Economic Geology.

Marfurt, K. J., 2005, Robust estimates of 3-D reflector dip: Submitted to Geophysics

Marfurt, K, J., and R. L. Kirlin, 2000, 3-D broad-band estimates of reflector dip and amplitude: Geophysics, **65**, 304-320.

Marfurt, K. J., R. M. Scheet, J. A. Sharp, and M. G. Harper, 1998a, Suppression of the acquisition footprint for sequence attribute mapping: Geophysics **63**, 1024-1035.

Marfurt, K. J., R. L. Kirlin, S. L. Farmer, and M. S. Bahorich, 1998b, 3-D seismic attributes using a semblance-based coherency algorithm: Geophysics **63**, 1150-1165.

Roberts, A., 2001. Curvature attributes and their application to 3-D interpreted horizons: First Break, **19**, 85-100.

Sheriff, R. E., 2002. Encyclopedic Dictionary of Applied Geophysics, **4th edition** Geophysical References Series, Society of Exploration Geophysicists.

Smith, J.W. and H. J. McKinley, 1996, Now what's happened to ground-roll? A 3-D perspective on linear-moveout noise rejection: **65th** Annual International Meeting Society of Exploration Geophysicists, Expanded Abstracts, 72-75.

Taner, M. T., F. Koehler, and R. Sheriff, R, 1979, Complex Seismic Trace Analysis: Geophysics **49**, 493-508.

Ward, R. F., C. G. St. C. Kendall, and P. M. Harris, 1986, Upper Permian (Guadalupian) Facies and Their Association with Hydrocarbons – Permian Basin, West Texas, and New Mexico: AAPG Bulletin **70,** 239-262.

Yilmaz, O., 1987. Seismic Data Processing. SEG Investigations in Geophysics, **Vol. 2**.

Yilmaz, O., I. Tanir, and C. Gregory, 2001. A unified 3-D seismic workflow: Geophysics **66**, 1699-1713.

General Reading References

Bates, R.L., and J. A. Jackson, Eds., 1984, Dictionary of Geological Terms, 3rd Ed.

Chen, Q. and S. Sidney, 1997, Seismic attribute technology for reservoir forecasting and monitoring: The Leading Edge **16**, 445-446.

Chopra, S., V. Sudhakar, G. Larsen, and H. Leong, 2000, Azimuth-based coherence for detecting faults and fractures: World Oil **221**.

Duncan, W., P. Constance, and K. J. Marfurt, 2002, Comparison of 3-D edge detection seismic attributes to Vinton Dome Louisiana, **72nd** Annual International Meeting Society of Exploration Geophysicists, Expanded Abstracts, 577-580.

Galikeev, T., 2001. Pre-Stack Depth Migration and Attribute Analysis of 3-D Time-Lapse P-wave Data Vacuum Field, New Mexico: Colorado School of Mines, Masters Thesis.

Guo, N., and S. Fagin, 2002a, Becoming effective velocity-model builders and depth imagers, Part 1 – The basics of prestack depth migration: The Leading Edge **21**, 1205-1209.

Guo, N., and S. Fagin, 2002b, Becoming effective velocity-model builders and depth imagers, Part 2 – The basics of velocity-model building, examples and discussions: The Leading Edge **21**, 1210-1216.

Hardage, B. A., J. L. Simmons, Jr., V. M. Pendleton, B. A. Stubbs, and B. J. Uszynski, 1998, 3-D imaging and interpretation of Brushy Canyon Slope and basin thin-bed reservoirs, northwest Delaware Basin: Geophysics **63**, 1507-1519.

Hesthammer, J., 1999, Improving seismic data for detailed structural interpretation: The Leading Edge **18**, 226-247.

Inanli, B., 2002, Impacts of Acquisition Footprint on Seismic Attribute Analysis: MS Thesis, University of Houston, 128 p.

Liu, Z., 1997, An analytical approach to migration velocity analysis: Geophysics **62**, 1238-1249.

Luo, Y., M. Mahoon, S. Al-Dossary, and M. Alfaraj, 2002, Edge-preserving smoothing: The Leading Edge **21**, 136-141.

Marfurt, K. J., V. Sudhaker, A. Gersztenkorn, K. D. Crawford, and S. E. Nissen, 1999, Coherency calculations in the presence of structural dip: Geophysics **64**, 104-111.

Ota, S., 2001. Integrated 3-D Seismic Analysis of the Atoka Formation sandstone reservoirs, Vacuum Field vicinity, Lea County, New Mexico: New Mexico Institute of Mining and Technology Masters Thesis.

Raiaskaran, S., and G. A. McMechan, 1995, Prestack processing of land data with complex topography: Geophysics **60**, 1875-1886.

Regone, C.J., and G. L. Rethford, 1990, Identifying, quantifying, and suppressing backscattered seismic noise: 60th Annual International Meeting of the Society of Exploration Geophysicists Expanded Abstracts, 748-751.

Roche, S., 1997, Time-lapse, multicomponent, three-dimensional seismic characterization of a San Andres shallow shelf carbonate reservoir, Vacuum Field, Lea County, New Mexico: Ph.D. Dissertation, Colorado School of Mines.

SEG Technical Standards Committee, 1993. Shell Processing Support Format for 3D Land Surveys: SEG Technical Standards Website Homepage (http://www. seg.org/publications/tech-stand/).

SEG Technical Standards Committee, 2002. SEG Y rev 1 Data Exchange Format: SEG Technical Standards Website Homepage (http://www.seg.org/publications/tech-stand/).

Vermeer, G. J. O., 1998, Factors affecting spatial resolution: The Leading Edge **17**, 1025-1029.

Vermeer, G. J. O., 2003, 3-D seismic survey design optimization: The Leading Edge **22**, 934-941.

Wehner, S.C., M. A. Raines, T. L. Davis, and R. D. Benson, 2000. Dynamic reservoir characterization at Central Vacuum Unit: SPE Annual Technical Conference and Exhibition, **SPE 63134.**